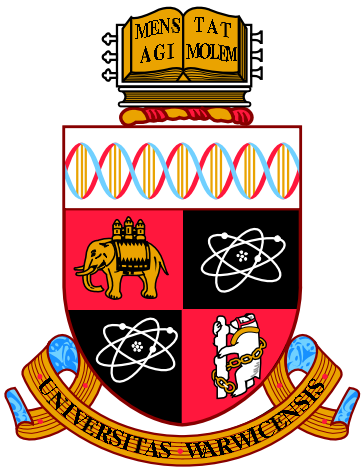

Boundary Layer Transition over Rotating Disks

by

Musa Özkan

Thesis

Submitted to The University of Warwick

for the degree of

Doctor of Philosophy

School of Engineering

October 2016

Contents

Contents i

Acknowledgments v

Declarations vi

Abstract vii

List of Figures viii

List of Tables xvii

Nomenclature xviii

Chapter 1 Introduction 1

Chapter 2 Literature Review 4

2.1 Rotating–Disk Flow 4

2.2 Previous Rotating–Disk Flow Experiments 8

2.3 Rotor–Stator Flow Configuration 11

2.4 BEK Family of Flows 13

2.5 Hot–Wire Anemometry and Calibration 15

2.6 Instabilities and Transition 19

Chapter 3 Numerical Model 26

3.1 Introduction 26

3.2 Computational Fluid Dynamics (CFD) 26
3.3 Governing Equations 27
3.4 Spatial Discretization 30
3.5 Transition–SST Model 32
3.6 Surface Roughness 37

Chapter 4 Numerical Results **43**

4.1 Flow Field 43
4.2 Validation of the Computational Approach 45
4.2.1 Comparison of TSST Results with Numerical and Experimental Literature Data 45
4.2.2 Comparison of TSST Results with Experimental Data of Colley et al. (2006) and von–Kármán Flow 48
4.2.3 Validation: Concluding Remarks 53
4.3 Comparison of TSST Results with the Current Experimental Data 54
4.4 Results from TSST Simulations: Geometry Effects vs. Roughness Effects 56
4.4.1 Geometry Effects 57
4.4.2 Roughness Effects 59
4.4.3 Comparison of Roughness–Induced Effects and Geometry–Induced Effects 62
4.4.4 Conclusions Based on Comparison of Geometry vs. Roughness Effects from TSST Simulations 62
4.5 Comparison of Roughness Effects obtained from TSST Simulations with Cooper et al. (2015), Garrett et al. (2016) and Alveroglu et al. (2016) 64
4.5.1 TSST Results vs. Cooper et al. (2015) 65
4.5.2 TSST Results vs. Garrett et al. (2016) 68
4.5.3 TSST Results vs. Alveroglu et al. (2016) 70

Chapter 5 Experimental Set–up **75**

5.1 Introduction 75

5.2 Experimental Facility 75

5.3 Tank Preparation 78

5.4 Test Disk Manufacture 79

5.5 Calibration 81

5.5.1 Introduction 81

5.5.2 Calibration Against von Kármán Flow 82

5.5.3 Rotating–Arm Calibration Method 84

5.6 Procedure for Velocity Measurements 86

Chapter 6 Experimental Results **89**

6.1 Comparison of Calibration Methods 89

6.2 Yaw Angle Correction 91

6.3 Velocity Profiles 97

6.3.1 Velocity Profiles over Smooth Disk 97

6.3.2 Velocity Profiles over Rough Disks 100

6.4 Velocity Fields 102

6.4.1 Velocity Fields over Smooth Disks 104

6.4.2 Velocity Fields over Single–Grooved Disks 106

6.4.3 Velocity Fields over Concentric–Grooved Disks 107

6.5 RMS Values of Velocity Profiles 109

6.6 Frequency Spectra 110

6.6.1 Frequency Spectra over Smooth Disks 111

6.6.1.1 Contour Plots of Frequency Spectra 113

6.6.2 Frequency Spectra over Concentric–Grooved Disks 114

6.6.2.1 Contour Plots of Frequency Spectra 115

6.6.3 Frequency Spectra over Single–Grooved Disks 115

6.6.3.1 Contour Plots of Frequency Spectra 117

6.6.4 Fourier Power Spectra 119
6.7 Vortex number 120
6.8 Neutral Stability Curves 124
6.8.1 Effect of Roughness on Neutral Stability Curves 128
6.9 PDF Contour Maps 134
6.9.1 Flow Structures Normal to the Disk Surface 137
6.9.2 Roughness Effect on PDF Contour Maps 139

Chapter 7 Summary and Conclusion **141**
7.1 Future Work 148

Bibliography **150**

Appendix **160**

Acknowledgments

Firstly, I would like to express my special appreciation and thanks to my supervisor, Professor Peter Thomas for his constant guidance, help and encouragement throughout my research; he is really an inspiration.

Also, I would like to express my gratitude to my unofficial co–supervisor Professor Stephen Garrett for his priceless help and assistance especially in carrying out the numerical investigation.

I also thank my former colleagues Dr Joseph Harris and Dr Jozef Vlaskamp for their assistance in setting up the experimental facility in the early stages of my research.

Moreover, I wish to acknowledge financial support from the Ministry of National Education of the Republic of Turkey. This thesis would have not been possible without this research funding.

Finally, I am very grateful to all of my family for their support and of course, especially, to my loving wife Hilal for her continuous encouragement, tolerance and unconditional love during the most hectic years of my life. Without her support, I would have gone mad. I am not sure if she has fully succeeded.

Declarations

This thesis is submitted to the University of Warwick in support of my application for the degree of Doctor of Philosophy. I hereby declare that this thesis has not been submitted in any previous application for any degree. The work presented was carried out by the author, except where explicitly stated.

Parts of this thesis have been published by the author:

1. Özkan, M., Harris, J. H., Garrett, S. J., Cooper, A. J. and Thomas, P. J. Effects of anisotropic surface roughness on the boundary–layer transition over rotating disks. *10^{th} European Fluid Mechanics Conference, EFMC–10*, Copenhagen, Denmark, 2014.

2. Özkan, M., Thomas, P. J., Cooper, A. J. and Garrett, S. J. Roughness–based laminar–flow control for boundary layers with a cross–flow component. *11^{th} European Fluid Mechanics Conference, EFMC–11*, Sevilla, Spain, 2016.

3. Özkan, M., Thomas, P. J., Cooper, A. J. and Garrett, S. J. Comparison of the effects of surface roughness and confinement on rotor–stator cavity flow. *to appear in Engineering Applications of Computational Fluid Mechanics. DOI: 10.1080/19942060.2016.1247297.*

Abstract

This thesis summarizes results of a combined numerical and experimental study investigating the effects of surface roughness, and of the geometry of the flow domain (confinement), on the boundary–layer transition over rotating disks.

Numerically, a three–dimensional enclosed cavity flow in a rotor–stator flow configuration is simulated. The effects induced by surface roughness of the rotor disk and the effects induced by the stator geometry enclosing the flow domain are investigated. The steady–state velocity profiles of the boundary–layer flow on the rotating disk are obtained, subjected to a linear stability analysis and compared to relevant data from the literature.

Experimentally, the flow over rotating disks is studied for smooth disk surfaces and for disks with concentric grooves representing distributed roughness. The disks are mounted submerged inside a water–filled tank. Due to the surrounding perimeter wall of the tank and the liquid surface this arrangement resembles the classic rotor–stator flow configuration. Comprehensive measurements of the boundary–layer flow and its laminar–turbulent transition were performed by means of an hot–film anemometer.

The computational results suggest that, for the rotor–stator flow investigated, the roughness–induced effects are very similar to the geometry–induced effects, both in nature and magnitude. This suggests that it may be difficult to distinguish between both effects in experiments where the flow domain is restricted.

Nevertheless, in comparison to previous hot–film measurements employing the same experimental facility, the data of the current study have been significantly improved by means of introducing a new calibration technique. The new experimental data discussed here confirm recent theoretical results of our research group in that they corroborate that an increase in the roughness level can reduce the number of stationary vortices and also stabilize the Type–I (cross–flow) instability mode.

However, the detailed analysis of the experimental data, in comparison to the theoretically predicted magnitude of the roughness–induced and the geometry–induced effects, reveal that future studies would greatly benefit from the availability of a new air–based rotating–disk apparatus.

List of Figures

2.1 Rotating–disk flow. 5

2.2 Mean velocity profiles $F(\zeta)$ (dashed line), $G(\zeta)$ (solid line) and $H(\zeta)$ (chain line) in a stationary reference frame. The numerical data for these profiles are shown in Table 2.1. 7

2.3 Comparison of the azimuthal velocity $G(\zeta)$ profile of the von Kármán flow with the experimentally obtained data by Lingwood (1996) (air–based facility) and Colley et al. (2006) (water–based facility). 9

2.4 Comparison of the radial velocity $F(\zeta)$ profile of the von Kármán flow with the experimentally obtained data by Lingwood (1996) (air–based facility) and Colley et al. (2006) (water–based facility). 10

2.5 Rotor–stator flow configuration. 11

2.6 The four flow regimes of the rotor–stator flow configuration proposed by Daily and Nece (1960). This figure is reproduced from Launder et al. (2010). Merged boundary layers: I (laminar) and III (turbulent). Unmerged boundary layers: II (laminar) and IV (turbulent). 12

2.7 Flow pattern on a disk rotating at $\Omega^* = 30$ rev/s. Photo taken from the study by Kobayashi et al. (1980). 20

2.8 Schematic sketches of the evolution of a wave packet generated by an impulse. (a) Convective instability. (b) Absolute instability. Sketch taken from Davies and Carpenter (2003). 23

2.9 Profiles of v_{rms} at $Re = 430$ ($\circ$), $Re = 470$ ($*$), $Re = 510$ ($\times$), $Re = 550$ ($\square$), $Re = 590$ ($\diamondsuit$), $Re = 630$ (∇). Figure taken from Imayama et al. (2012). 24

2.10 The PDF of the azimuthal fluctuation velocity v at $\zeta = 1.3$ normalized with the wall speed. Filled contours indicate 10%, 20%, 30%, 40%, 50%, 60%, 70%, 80%, and 90% of the local PDF value. Figure taken from Imayama et al. (2012). 24

3.1 The grid on the cross–sectional area of the rotor–stator flow configuration in $r^* - \theta$ plane. 31

3.2 A part of the grid on the cross–sectional area of the rotor–stator flow configuration in $r^* - z^*$ plane. 31

3.3 Demonstration of sand roughness. 38

4.1 Flow field on the cross–sectional area (r^*–z^*–plane) of the rotor–stator flow configuration. $\Omega^* = 1$ rad/s, $Re_\phi = 600$, $h^* = 40\delta$, $D = 0.367$. 44

4.2 The change of intermittency factor γ in the radial direction r^*. Laminar region: $\gamma \cong 0$; Transition region: $0 < \gamma < 1$; Turbulent region: $\gamma = 1$. $\Omega^* = 1$ rad/s, $Re_\phi = 600$, $h^* = 40\delta$, $D = 0.367$. . . 45

4.3 Comparison of the results of the TSST simulation with previous numerical (Vaughan, 1986) and experimental (Sambo, 1983) data ($Re_\phi = 224$ and $D = 0.1$). 46

(a) Radial velocity F, at $Re = 112$. 46

(b) Azimuthal velocity G, at $Re = 134$. 46

4.4 Comparison of the results of the TSST simulations ($D = 0.092$, $h^* = 10\delta$, $Re_\phi = 733$, $Re = 210$ and $Re = 546$) to the experimental data from Figure 2 in Colley et al. (2006) and von Kármán (1921) similarity solution. 49

(a) Radial velocity F 49

(b) Azimuthal velocity G 49

4.5 Comparison of the results of the TSST simulations ($D = 0.918$, $h^* = 100\delta$, $Re_\phi = 733$, $Re = 210$ and $Re = 546$) to the experimental data from Figure 2 in Colley et al. (2006) and von Kármán (1921) similarity solution. 51

(a) Radial velocity F 51

(b) Azimuthal velocity G 51

4.6 The Reynolds number dependence of the velocity profiles obtained from the current TSST simulations ($h^* = 100\delta$, $Re_\phi = 600$) and experiments ($h^* = 76\delta$, $Re_\phi = 560$). 55

(a) Radial velocity F 55

(b) Azimuthal velocity G 55

4.7 The effect of the aspect ratio D on the basic flow profiles ($Re_\phi = 600$, $Re = 500$). 58

(a) Radial velocity F 58

(b) Azimuthal velocity G 58

4.8 The effect of isotropic roughness on the basic flow profiles ($D = 0.092$, $h^* = 10\delta$, $Re_\phi = 600$, $Re = 500$). 60

(a) Radial velocity F 60

(b) Azimuthal velocity G 60

4.9 Comparison between the effects of the aspect ratio D and the geometric roughness heights K ($Re_\phi = 600$, $Re = 500$). 63

(a) Radial velocity F 63

(b) Azimuthal velocity G 63

4.10 Comparison between the roughness effects predicted by the TSST simulations ($Re_\phi = 600$, $Re = 500$) and the roughness effects as predicted by using the code of Cooper et al. (2015) ($\lambda = 0$) based on their *partial slip* approach. Markers identify current TSST data and lines represent data of Cooper et al. (2015). 66

(a) Radial velocity F 66
(b) Azimuthal velocity G 66
4.11 Comparison between the roughness effects predicted by the TSST simulations ($Re_\phi = 600$, $Re = 500$) and the roughness effects predicted in Garrett et al. (2016) based on the approach of modelling roughness by prescribing a surface distribution as a function of the radial position. Markers identify current TSST data and lines represent data of Garrett et al. (2016). 69
(a) Radial velocity F 69
(b) Azimuthal velocity G 69
4.12 Comparison of neutral curves obtained by the TSST simulations for the rotor–stator flow configuration with the ones presented by Alveroglu et al. (2016) for isotropic roughness. Markers identify results of stability calculations based on current TSST data and lines represent data of Alveroglu et al. (2016). 72
(a) von Kármán flow 72
(b) Ekman flow 72

5.1 Rotating disk facility. 76
5.2 The sketch of the experimental facility. 77
5.3 TSI 1218–20W hot–film probe. 77
5.4 Dantec Dynamics MiniCTA 54T42 constant temperature anemometer. 78
5.5 Distributed concentric grooves on the surface of a test disk. 80
5.6 Superimposition of a sine function onto the surface profile of a distributed concentric grooved disk. 80
5.7 A single groove on the surface of a test disk. The diameter of the groove is 180 mm. 81
5.8 A sketch of the rotating–arm calibration method. 84

5.9 Slip–ring MERCOTAC Inc. 85
5.10 Triggering system consists of optical sensors and a metallic reflective mark on the shaft. 87

6.1 Calibration curves of extended King's law equation, $E^2 = A + BU^n + CU^{2n}$. 90
6.2 Radial velocity profiles. 90
6.3 Azimuthal velocity profiles. 91
6.4 The sketch of the along–wire cooling effect on a hot–wire probe. . 92
6.5 Data obtained by rotating–arm calibration method at $\alpha_y = 0°$ and $\alpha_y = 90°$. 93
6.6 Yaw coefficient, ${k_y}^2$. 94
6.7 Effective cooling near the surface of the rotating disk. 95
6.8 Radial velocity profiles with yaw–angle correction at $Re = 300$ and $Re = 510$. Red symbols indicate corrected profiles. 96
6.9 Radial velocity profiles $F(\zeta)$ obtained experimentally at radial locations that correspond to $Re = 200$, $Re = 300$, $Re = 400$, $Re = 510$ and $Re = 530$ at $\Omega = 7.85$ rad/s. 98
6.10 The deformation of the free–surface of water in the vicinity of the rotational axis. 99
6.11 Azimuthal velocity profiles $G(\zeta)$ obtained experimentally at radial locations that correspond to $Re = 200$, $Re = 300$, $Re = 400$, $Re = 510$ and $Re = 530$. 99
6.12 Radial velocity profiles $F(\zeta)$ obtained at $Re = 400$ and $\Omega = 7.85$ rad/s for concentric–grooved disks. 101
6.13 Azimuthal velocity profiles $G(\zeta)$ obtained at $Re = 400$ and $\Omega = 7.85$ rad/s for concentric–grooved disks. 101
6.14 Ensemble averaged azimuthal velocity traces taken over the smooth disk at $\zeta = 1.3$ and $\Omega^* = 7.85$ rad/s. 104

6.15 Ensemble averaged azimuthal velocity traces taken over the smooth disk which was deliberately positioned off–centre. The data were collected at $\zeta = 1.3$ and $\Omega^* = 7.85$ rad/s. 105
6.16 Ensemble averaged azimuthal velocity traces taken over a single–grooved disk with a groove depth of $A = 1$ mm. The data were collected at $\zeta = 1.3$ and $\Omega^* = 7.85$ rad/s. The groove is at $Re = 252$.106
6.17 Ensemble averaged azimuthal velocity traces taken over the disk with distributed concentric grooves, $a = 0.071$. The data were collected at $\zeta = 1.3$ and $\Omega^* = 7.85$ rad/s. 107
6.18 Ensemble averaged azimuthal velocity traces taken over the disk with distributed concentric grooves, $a = 0.167$. The data were collected at $\zeta = 1.3$ and $\Omega^* = 7.85$ rad/s. 108
6.19 Profiles of v_{rms} at $\Omega^* = 12.57$ rad/s. 109
6.20 Three dimensional view of the Fourier energy spectrum. The data were collected over the smooth disk at $\zeta = 1.3$ and $\Omega^* = 7.85$ rad/s.111
6.21 The contour plot of the Fourier energy spectrum. The data were collected over the smooth disk at $\zeta = 1.3$ and $\Omega^* = 7.85$ rad/s. . . 113
6.22 Three dimensional view of the Fourier energy spectrum. The data were collected over the concentric–grooved disk with $A = 0.15$ μm, $B = 1.5$ μm, $a = 0.1$ at $\zeta = 1.3$ and $\Omega^* = 7.85$ rad/s. 115
6.23 The contour plot of Fourier energy spectra. The data were collected over the concentric–grooved disk with $A = 0.15$ μm, $B = 1.5$ μm, $a = 0.1$ at $\zeta = 1.3$ and $\Omega^* = 7.85$ rad/s. 116
6.24 Three dimensional view of the Fourier energy spectrum. The data were collected over the single–grooved disk with $A = 1$ mm at $\zeta = 1.3$ and $\Omega^* = 7.85$ rad/s. 116
6.25 Three dimensional view of the Fourier energy spectrum. The data were collected over the single–grooved disk with $A = 0.5$ mm at $\zeta = 1.3$ and $\Omega^* = 7.85$ rad/s. 117

6.26 The contour plot of the Fourier energy spectrum. The data were collected over the single–grooved disk with $A = 1$ mm at $\zeta = 1.3$ and $\Omega^* = 7.85$ rad/s. 118

6.27 The contour plot of the Fourier energy spectrum. The data were collected over the single–grooved disk with $A = 0.5$ mm at $\zeta = 1.3$ and $\Omega^* = 7.85$ rad/s. 118

6.28 Fourier power spectra for ensemble–averaged time series measured over the smooth disk at $\zeta = 1.3$ and $\Omega^* = 7.85$ rad/s. 119

6.29 The number of vortices acquired from the frequency contour plots which are shown in Section 6.6 against the roughness ratio a. . . . 121

6.30 The number of vortices against the groove width B in mm where the groove depth A is kept constant at $A = 0.05$ mm. 122

6.31 The number of vortices against the non–dimensional roughness height, $A\sqrt{\Omega^*/\nu^*}$. The disks with same non–dimensional roughness height are represented with the same symbols. 123

6.32 Amplification diagram for the frequency of 22.5 Hz for a disk with a single groove which has a depth of $A = 1$ mm. Data was smoothed with a 3–point moving average filter. Vertical line shows the point of minimum energy. Interpolation curve (solid line) is a 5^{th} degree polynomial. 125

6.33 Experimental data relating to the neutral stability curve for the smooth disk rotating at $\Omega^* = 7.85$ rad/s. 126

6.34 Experimentally obtained neutral stability data superimposed on the frequency contour map for the smooth disk rotating at $\Omega^* = 7.85$ rad/s. 127

6.35 Comparison of the experimentally obtained neutral stability data for disks with distributed concentric grooves rotating at $\Omega^* = 7.85$ rad/s. 129

6.36 Neutral stability data for a smooth disk. Comparison of our numerical (CFD) and experimental data with the numerical results by Harris (2013). 129

6.37 Neutral stability data for rough disks. Harris (2013) for $a = 0.08$, Experiments for $a = 0.071$ and CFD simulations for $K = 100$ μm, $K = 300$ μm, $K = 500$ μm. 131

6.38 Neutral stability data for rough disks. Harris (2013) for $a = 0.16$, Experiments for $a = 0.167$ and CFD simulations for $K = 100$ μm, $K = 300$ μm, $K = 500$ μm. 133

6.39 The PDF of the instantaneous azimuthal fluctuation velocity v at $\zeta = 1.3$ normalized by the corresponding wall speed. For the smooth disk rotating at $\Omega^* = 12.57$ rad/s. Filled contours indicate 10%, 20%, 30%, 40%, 50%, 60%, 70%, 80%, 90% of the local PDF value. 136

6.40 The PDF of the instantaneous azimuthal fluctuation velocity normalized by the corresponding wall speed for the smooth disk rotating at $\Omega^* = 12.57$ rad/s. (a) $Re = 200$, (b) $Re = 430$, (c) $Re = 470$, (d) $Re = 510$, (e) $Re = 550$, (f) $Re = 590$, and (g) $Re = 630$. Filled contours indicate same as Figure 6.39. The range of the abscissa is -0.5 to +0.5 for all Re. 138

6.41 The PDF of the instantaneous azimuthal fluctuation velocity v at $\zeta = 1.3$ normalized by the corresponding wall speed. For the rough disk ($A = 0.05$ mm, $B = 0.3$ mm and $a = 0.167$) rotating at $\Omega^* = 12.57$ rad/s. Filled contours indicate same as Figure 6.39. 140

7.1 The contour plot of the Fourier energy spectrum on a logarithmic scale. The data were collected over the smooth disk at $\zeta = 1.3$ and $\Omega^* = 7.85$ rad/s. 162

7.2 The surface function of the amplitude variation with respect to the azimuthal mode number, n, and the Reynolds number, Re. The data were collected over the smooth disk at $\zeta = 1.3$ and $\Omega^* = 7.85$ rad/s. The fitted polynomial surface is of degree 3 in both x and y. The coefficient of determination: $R^2 = 0.5828$. . . . 162

List of Tables

2.1 Numerical data originally produced by Rogers and Lance (1960) and taken from Owen and Rogers (1989, p. 47). 6

5.1 The dimensions of the distributed concentric grooves on the surfaces of the rough disks, all in microns. 80

6.1 Yaw coefficient, k_y, data obtained by rotating–arm calibration method 94

Nomenclature

A groove depth

$A(f)^2$ non-dimensional energy content

A_r roughness amplification

B groove width

D aspect ratio of rotor–stator configuration

D_k destruction term of SST model

E raw voltage read by hot–film probe

E_γ destruction/relaminarization source term

F non-dimensional radial velocity component

F_{length} empirical correlation of the length of transition region

F_{onset} empirical correlation of the transition onset location

$F_{\theta t}$ blending function

G non-dimensional azimuthal velocity component

H non-dimensional axial velocity component

K real geometric roughness height

P non-dimensional pressure

$P(f)$ power spectral amplitude

$P_\gamma, P_{\theta t}$ transition source terms

P_{AR} source term for A_r

P_k production term of SST model

R^* radius of disk (rotor)

Re local (usual) rotational Reynolds number

Re_ϕ global rotational Reynolds number

Re_{θ_t} transition onset momentum–thickness Reynolds number

$\tilde{Re}_{\theta_t}$ local transition onset momentum–thickness Reynolds number

Ro Rossby number

S strain–rate magnitude

S_{ij} strain–rate tensor

Tu turbulence intensity

U^* velocity

U_N velocity component normal to the hot-film

U_T velocity component tangential to the hot-film

V_e effective velocity

a roughness ratio

f physical frequency

f^* angular frequency of the motor

f_D frequency of disk (rotor)

h^*	gap between rotor and stator
k	turbulence kinetic energy
k_s	sand roughness height
${k_s}^+$	non-dimensional surface roughness
k_{seq}	equivalent sand roughness height
k_y	yaw coefficient
l^*	length of rotating arm
n	non-dimensional frequency
p^*	pressure
t_1	time interval
u^*	radial velocity component
${u_\tau}^*$	friction velocity
$\overline{u^*}, \overline{v^*}, \overline{w^*}$	time averages of velocities
$u^{*\prime}, v^{*\prime}, w^{*\prime}$	fluctuation velocities
v^*	azimuthal velocity component
w^*	axial velocity component
x^*, y^*, z^*	Cartesian coordinates
y	distance to nearest wall
$y+$	coordinate in viscous wall layer
Δ	Laplace operator
Ω	vorticity magnitude

Ω^* angular velocity of disk (rotor)

$\Omega_F{}^*$ angular velocity of fluid

$\Omega_S{}^*$ angular velocity of system

α_r wave–number of radial disturbances

α exponential growth rate

α_y yaw angle

δ boundary–layer thickness

δ^* characteristic length scale

δ_2 boundary–layer thickness in TSST model

ϵ turbulent dissipation

η slip coefficient in azimuthal direction

γ intermittency factor

λ slip coefficient in radial direction

λ_θ pressure gradient parameter

μ^* viscosity

$\mu_t{}^*$ eddy viscosity

ν^* kinematic viscosity

ω specific dissipation rate

r^*, θ, z^* cylindrical polar–coordinates

ρ^* density

σ_k turbulent Prandtl number for k

$\sigma_{x,y,z}, \tau_{xy,xz,yz}$ Reynolds stresses

${\tau_w}^*$ wall shear stress

ζ non-dimensional vertical position

CFD computational fluid dynamics

CTA constant temperature anemometer

DAQ data acquisition card

DC direct current

DNS direct numerical simulation

LDA laser Doppler anemometer

LK Lingwood–Karman calibration

NI National Instruments

PC personal computer

PDF probability density function

RANS Reynolds Average Navier–Stokes

RA rotating–arm calibration

SR Strouhal–Reynolds number

rms root mean square

Chapter 1

Introduction

The boundary–layer flow over a rotating disk is the paradigm to study fully three–dimensional boundary–layer flows. Such boundary layers are of particular interest because they are encountered in similar form in, for instance, the flow over highly–swept wings in the aviation industry or the blades of wind turbines (Lingwood and Alfredsson, 2015; Saric et al., 2003; Reed and Saric, 1989). The rotating–disk flow, furthermore, has great experimental importance because of its ease of use and repeatability. For instance, conducting an experiment over a rotating disk is easier than investigating the flow over a scaled swept wing model because a wind tunnel is not necessary and there is no leading–edge contamination in the flow arising from the body holding the wing model (Healey, 2007). The rotating–disk flow has also attracted numerous theoretical researchers over the last 60 years because it represents one of the few examples for which there exists an exact similarity solution of the Navier–Stokes equations. This similarity solution was first derived by von Kármán (1921) to represent an axisymmetric steady laminar flow over an infinite disk rotating in otherwise still fluid. This exact solution of the Navier–Stokes equations can be obtained relatively easy in comparison with the most numerical solutions of the three–dimensional boundary layers. These benefits of the rotating–disk flow were initially identified by Theodorsen and Regier (1944) and Gregory et al. (1955) in their pioneering pa-

pers.

Understanding of the characteristics of the boundary–layer flows over rotating disks, particularly the transition process from laminar to turbulent, has recently become crucial as a result of an increased interest in the flow control techniques to reduce skin–friction drag. The skin–friction drag is higher when the flow is turbulent and thus the flow–control techniques attempt to delay transition and sustain laminar flow. Saric et al. (2011) briefly reviewed these flow–control techniques for three–dimensional boundary layers which appear over rotating disks. One of these control methods is the application of surface roughness. Based on numerous experimental and numerical studies in literature, roughness has been thought to lead to an advanced transition from laminar to turbulent (Dryden, 1953; Merkle et al., 1974). However, it has recently been revealed that the *right sort of roughness* can actually stabilise the flow and thus reduce skin–friction drag (Carpenter, 1997).

Most recently, for instance, Cooper et al. (2015) and Garrett et al. (2016) have numerically shown the stabilizing effect of distributed surface roughness on the inviscid instability which is considered to be the main instability mechanism for the rotating–disk flow. Roughness, in these studies, has been investigated numerically only and thus both of these studies suggested that only detailed experimental investigations can ultimately reveal whether these theoretical roughness models can be employed in practice or different alternative methods have to be pursued.

Accordingly, the main goal of this project is to answer whether it is possible to experimentally measure the effects of distributed surface roughness and quantitatively compare them with these theoretical predictions by Cooper et al. (2015) and Garrett et al. (2016). This experimental set–up and the results are presented in Chapter 5 and 6 of this thesis, respectively.

Despite the fact that the theoretical studies by Cooper et al. (2015) and Garrett et al. (2016) obtained the flow fields from the exact similarity solution

by von Kármán for a disk spinning in an infinite–fluid environment, the previous experimental rotating–disk research at Warwick (Colley et al., 1999, 2006; Harris, 2013), conducted prior to our current study, indicated the existence of substantial wall-induced effects, arises from the finite size of the experimental facility (water tank), which appeared to lead to discrepancies with the von Kármán flow.

Due to the fact that the same water–based facility is used for our experiments, it is believed that a numerical investigation is beneficial to distinguish, if possible, between the effects of the surface roughness and the finite size of the experimental facility. This examination, therefore, comprises another goal of the current research and this numerical study and the results are presented in Chapter 3 and 4, respectively.

Furthermore, during the research carried out by Harris (2013) at Warwick, the linear–motor system of the experimental facility, which had been being used for performing the calibration was irreversibly broken and therefore an alternative calibration technique had to be designed. This newly introduced method of calibration is also presented in Section 5.5.3 of Chapter 5.

Chapter 2

Literature Review

2.1 Rotating–Disk Flow

The flow scenario of an infinite–flat disk spinning in an unbounded fluid which is otherwise at rest sufficiently far above the disk was first studied by von Kármán (1921) who derived an exact similarity solution which reduces the full system of Navier–Stokes equations to a couple of non–linear ordinary differential equations in the axial coordinate (Zandbergen and Dijkstra, 1987). Figure 2.1 illustrates this rotating disk flow. The disk, of radius R^*, rotates with an angular velocity Ω^* about an axis that is perpendicular to the surface of the disk. It is natural to consider this geometry in a cylindrical polar–coordinate system (r^*, θ, z^*) in which the governing Navier–Stokes equations are well known. The radial, azimuthal and axial velocity components of the boundary–layer flow are denoted as, u^*, v^* and w^*, respectively.

The azimuthal velocity component v^* is formed as a result of viscosity and the no–slip boundary condition on the surface of the disk where the fluid is carried along with the rotation of the disk. The magnitude of this tangential component of the velocity varies from $v^* = \Omega^* r^*$ on the surface of the disk to $v^* = 0$ far above the disk. This rotary flow is also orientated radially outwards due to the centrifugal effects and establishes the radial velocity component u^* of

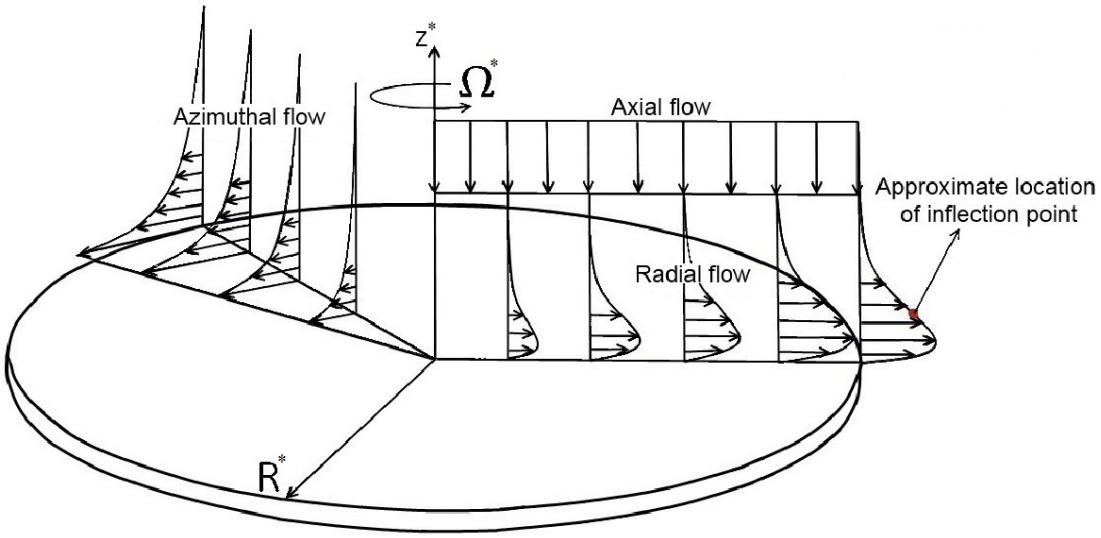

Figure 2.1: Rotating–disk flow.

the boundary layer. The axial velocity component w^* then appears downward towards the disk surface to satisfy mass conservation. For the rotating–disk flow, it is the radial flow component which represents the cross–flow component. The velocity profile of the cross–flow component has an inflection point (Rayleigh, 1879) at some height above the disk surface (*cf.* Figure 2.1) and this characteristic is shared with all other three-dimensional boundary layers where such a cross–flow exists.

All dimensional quantities are scaled on a characteristic length scale given by $\delta^* = \sqrt{\nu^*/\Omega^*}$, where ν^* is the kinematic viscosity of the fluid. The velocity scale is also given by $\Omega^* r^*$. The vertical coordinate z^* is normalized with the length scale as $\zeta = z^*/\delta^*$ and the usual (local) rotational Reynolds number is defined as

$$Re = \sqrt{\frac{\Omega^* r^{*2}}{\nu^*}}. \tag{2.1}$$

The three velocity components and also pressure are non–dimensionalized as

$$F(\zeta) = \frac{u^*}{\Omega^* r^*} \ , \quad G(\zeta) = \frac{v^*}{\Omega^* r^*} \ , \quad H(\zeta) = \frac{w^*}{\sqrt{\nu^* \Omega^*}} \ , \quad P(\zeta) = \frac{p^*}{\rho^* \nu^* \Omega^*}. \tag{2.2}$$

Table 2.1: Numerical data originally produced by Rogers and Lance (1960) and taken from Owen and Rogers (1989, p. 47).

ζ	$F(\zeta)$	$G(\zeta)$	$H(\zeta)$	$F'(\zeta)$	$G'(\zeta)$
0.0	0.0000	1.0000	0.0000	0.5102	-0.6159
0.1	0.0463	0.9386	-0.0046	0.4163	-0.6112
0.2	0.0837	0.8781	-0.0176	0.3338	-0.5987
0.3	0.1135	0.8191	-0.0373	0.2620	-0.5803
0.4	0.1366	0.7621	-0.0624	0.1999	-0.5577
0.5	0.1539	0.7076	-0.0914	0.1467	-0.5321
0.6	0.1663	0.6558	-0.1234	0.1015	-0.5047
0.7	0.1745	0.6067	-0.1575	0.0635	-0.4764
0.8	0.1792	0.5604	-0.1929	0.0317	-0.4476
0.9	0.1810	0.5171	-0.2289	0.0056	-0.4191
1.0	0.1805	0.4766	-0.2651	-0.0157	-0.3911
1.1	0.1780	0.4388	-0.3009	-0.0327	-0.3641
1.2	0.1740	0.4037	-0.3362	-0.0461	-0.3381
1.3	0.1689	0.3711	-0.3705	-0.0564	-0.3133
1.4	0.1628	0.3409	-0.4036	-0.0640	-0.2898
1.5	0.1561	0.3130	-0.4355	-0.0693	-0.2677
1.6	0.1489	0.2873	-0.4660	-0.0728	-0.2470
1.7	0.1415	0.2636	-0.4951	-0.0747	-0.2276
1.8	0.1340	0.2417	-0.5227	-0.0754	-0.2095
1.9	0.1264	0.2216	-0.5487	-0.0751	-0.1927
2.0	0.1190	0.2031	-0.5733	-0.0739	-0.1771
2.1	0.1116	0.1861	-0.5963	-0.0721	-0.1627
2.2	0.1045	0.1705	-0.6180	-0.0698	-0.1494
2.3	0.0976	0.1562	-0.6382	-0.0671	-0.1371
2.4	0.0910	0.1431	-0.6571	-0.0643	-0.1258
2.5	0.0848	0.1310	-0.6746	-0.0612	-0.1153
2.6	0.0788	0.1200	-0.6910	-0.0580	-0.1057
2.7	0.0731	0.1098	-0.7062	-0.0548	-0.0969
2.8	0.0678	0.1006	-0.7203	-0.0517	-0.0888
2.9	0.0628	0.0921	-0.7334	-0.0485	-0.0814
3.0	0.0580	0.0843	-0.7455	-0.0455	-0.0745
3.2	0.0495	0.0706	-0.7670	-0.0397	-0.0625
3.4	0.0421	0.0591	-0.7853	-0.0343	-0.0524
3.6	0.0357	0.0495	-0.8008	-0.0296	-0.0440
3.8	0.0302	0.0415	-0.8140	-0.0253	-0.0369
4.0	0.0255	0.0347	-0.8252	-0.0216	-0.0309
4.5	0.0166	0.0222	-0.8460	-0.0144	-0.0199
5.0	0.0107	0.0142	-0.8595	-0.0094	-0.0128
5.5	0.0069	0.0091	-0.8682	-0.0062	-0.0082
6.0	0.0044	0.0057	-0.8738	-0.0040	-0.0053
7.0	0.0017	0.0022	-0.8796	-0.0017	-0.0022
8.0	0.0006	0.0008	-0.8818	-0.0007	-0.0009
9.0	0.0001	0.0002	-0.8826	-0.0003	-0.0004
10	0.0000	0.0000	-0.8828	-0.0001	-0.0002

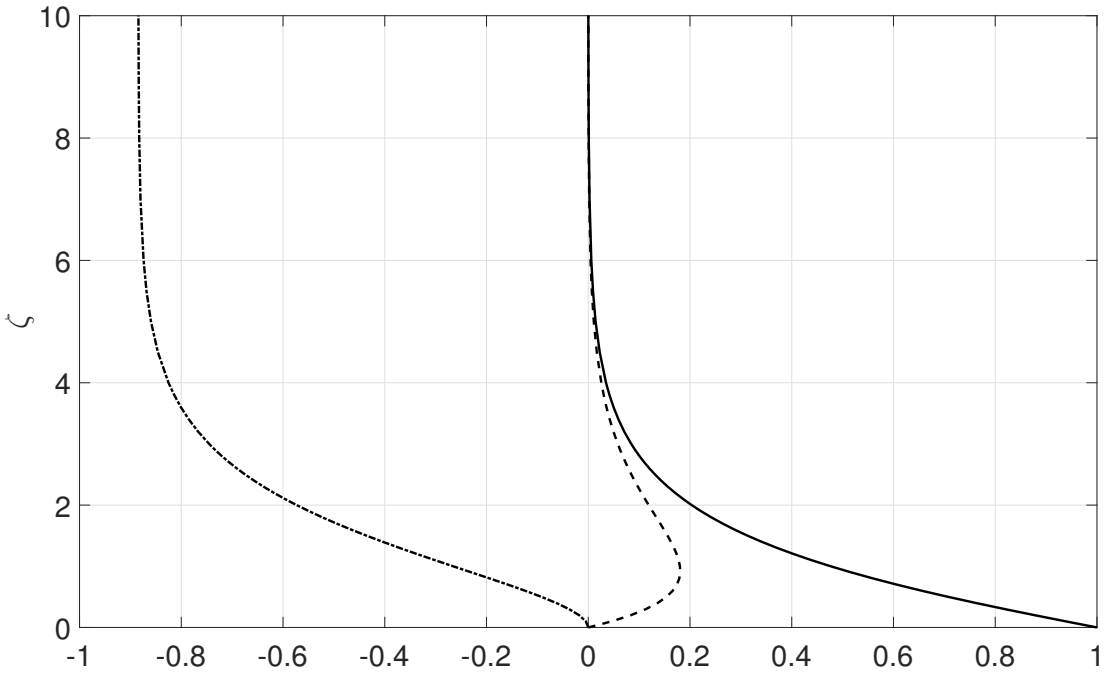

Figure 2.2: Mean velocity profiles $F(\zeta)$ (dashed line), $G(\zeta)$ (solid line) and $H(\zeta)$ (chain line) in a stationary reference frame. The numerical data for these profiles are shown in Table 2.1.

After non-dimensionalization, the following system of ordinary differential equations is obtained:

$$\begin{aligned} 2F + H' &= 0 \\ F^2 + F'H - G^2 - F'' &= 0 \\ 2FG + HG' - G'' &= 0 \\ P' + HH' - H'' &= 0 \end{aligned} \tag{2.3}$$

These are then subjected to boundary conditions:

$$\begin{aligned} \zeta = 0: &\quad F = 0, \quad G = 1, \quad H = 0, \quad P = 0 \\ \zeta \to \infty: &\quad F = 0, \quad G = 0 \end{aligned} \tag{2.4}$$

The solution of this system was first provided approximately by von Kármán (1921) and subsequently more accurate and precise calculation was obtained by Cochran (1934). A comprehensive set of numerical data for $F(\zeta), G(\zeta)$, $H(\zeta)$ and their derivatives $F'(\zeta)$, $G'(\zeta)$ for $0 \leq \zeta \leq 10$, can be found in tabulated form

in Table 2.1 which was reproduced from Owen and Rogers (1989, p. 47) where the data were originally produced by Rogers and Lance (1960). The inspection of the data for $G(\zeta)$ in that table reveals that the boundary–layer thickness, i.e. the height for which the azimuthal velocity component is $v^* = 0.01\Omega^* r^*$ (that is, $G(\zeta) = 0.01$), is given by $\delta = 5.5\ \delta^*$. Mean velocity profiles are plotted in Figure 2.2 in a stationary reference frame by means of the numerical data illustrated in Table 2.1.

2.2 Previous Rotating–Disk Flow Experiments

Several rotating–disk flow experiments were conducted prior to our study at Warwick using the same experimental facility. This facility, which is mainly a submerged disk rotating inside a water tank, was designed and built by Colley (1997). Colley et al. (1999, 2006), then, investigated the laminar–turbulent transition of the boundary layer over rigid and compliant disks by means of this experimental facility. Additionally, Zoueshtiagh et al. (2003) obtained a short set of data for the velocity profiles over disks with different sizes of quartz granules attached on their surfaces to investigate the effects of distributed roughness on the mean flow profiles. Harris (2013), more recently, examined the effects of different types of distributed surface roughness on the transition process from laminar to turbulent by means of the disks with concentric grooves on their surfaces. All of these previous experimental studies indicated that, as a result of the finite size of this water–based facility, there is an alteration to the von Kármán flow where the disk rotates freely in an unbounded fluid. Consideration of this modification is significant when the experimental data need to be compared with the theoretical predictions, such as Cooper et al. (2015) and Garrett et al. (2016), where the flow field is obtained from the von Kármán's similarity solution.

In addition to the above mentioned experiments, Lingwood (1996), Corke et al. (2007) and Imayama et al. (2012), for instance, carried out rotating–disk

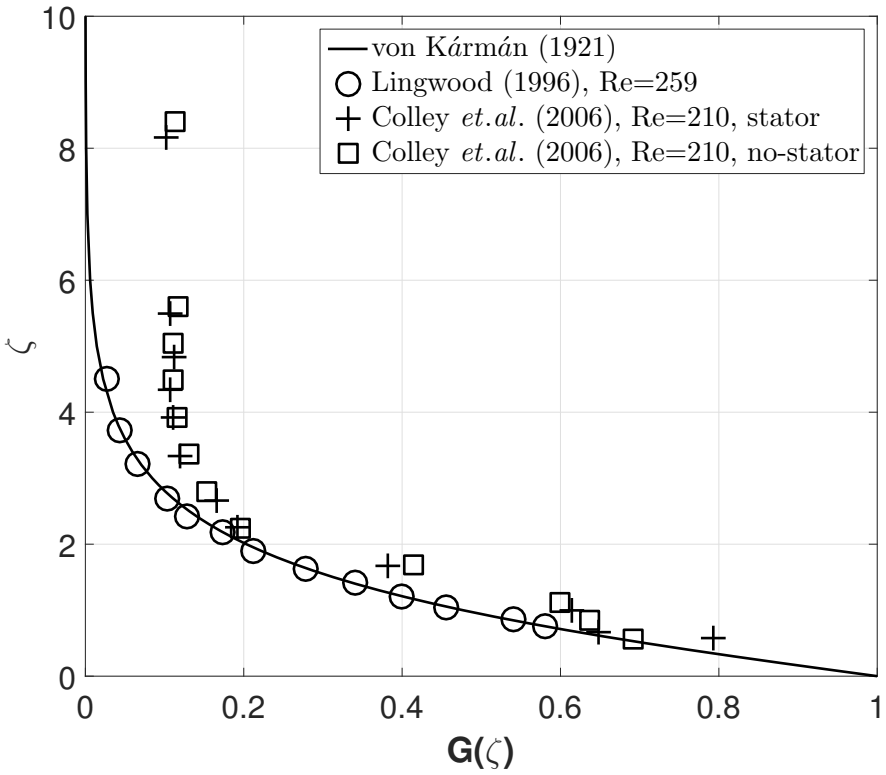

Figure 2.3: Comparison of the azimuthal velocity $G(\zeta)$ profile of the von Kármán flow with the experimentally obtained data by Lingwood (1996) (air–based facility) and Colley et al. (2006) (water–based facility).

experiments by means of air–based experimental facilities. Laminar mean velocity profiles in these studies approximate to the von Kármán's solution better than those obtained using the water–based facilities.

Herein, for clarification, it is useful to illustrate and compare some of the previous data obtained by Lingwood (1996) (air–based) and by Colley et al. (2006) (water–based). This comparison, for the azimuthal velocity profile $G(\zeta)$, is shown in Figure 2.3. The solid line represents the von Kármán flow and its value varies from $G(\zeta) = 1$ on the surface of the disk where $\zeta = 0$ to $G(\zeta) = 0$ far above the disk where $\zeta = 10$. It can be seen that the data provided by Lingwood (1996) fully agree with this similarity solution. However, there are discrepancies between the data provided by Colley et al. (2006) and the similarity solution. The most obvious difference appears after approximately $\zeta > 2$ where the azimuthal velocity by Colley et al. (2006) does not tend to zero far above the disk surface and remains constant at approximately $G(\zeta) \cong 0.11$. This is the indication of the

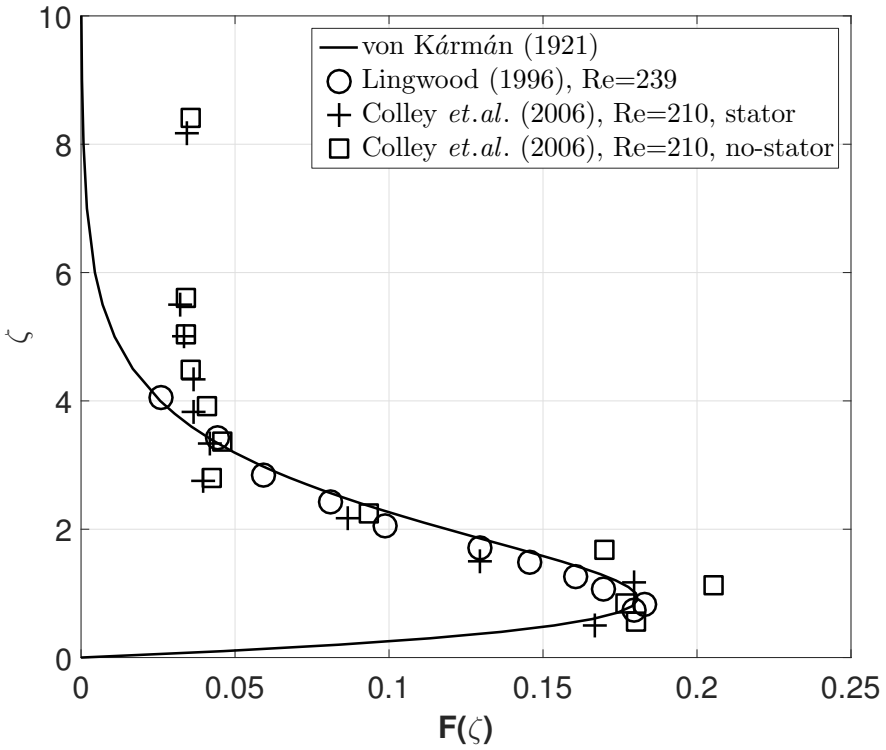

Figure 2.4: Comparison of the radial velocity $F(\zeta)$ profile of the von Kármán flow with the experimentally obtained data by Lingwood (1996) (air–based facility) and Colley et al. (2006) (water–based facility).

residual motion of whole water over the rotating disk. Similar discrepancy also exists for the radial velocity profiles and can be seen in Figure 2.4.

Note here that Colley et al. (2006) have two different experimental configurations, please see Figure 1 of their paper for an illustration. In one of them, in order to minimize undesirable boundary effects such as arising, for instance, from waves on the liquid surface, the flow over the disk was covered with a stationary lid and the other configuration is without this lid. The flow domain with the stationary lid exactly represents a rotor–stator flow configuration which is addressed here in Section 2.3. These two configurations are referred to as *stator* (with the lid) and *no–stator* (without the lid) in Figures 2.3 and 2.4. It is obvious that there is no difference between these two forms of flow configurations in terms of mean velocity profiles. Therefore, the water–based rotating–disk facility with or without a stationary lid can be considered to resemble more like a rotor–stator flow configuration rather than a free disk rotating in an unbounded fluid.

2.3 Rotor–Stator Flow Configuration

In addition to the rotating–disk flow in an infinite fluid, the rotor–stator flow configuration needs to be introduced since it is addressed in the numerical investigation part of the current study. This numerical investigation is essential due to the explanation previously given in Section 2.2 for the modification of the rotating–disk flow in our experiments.

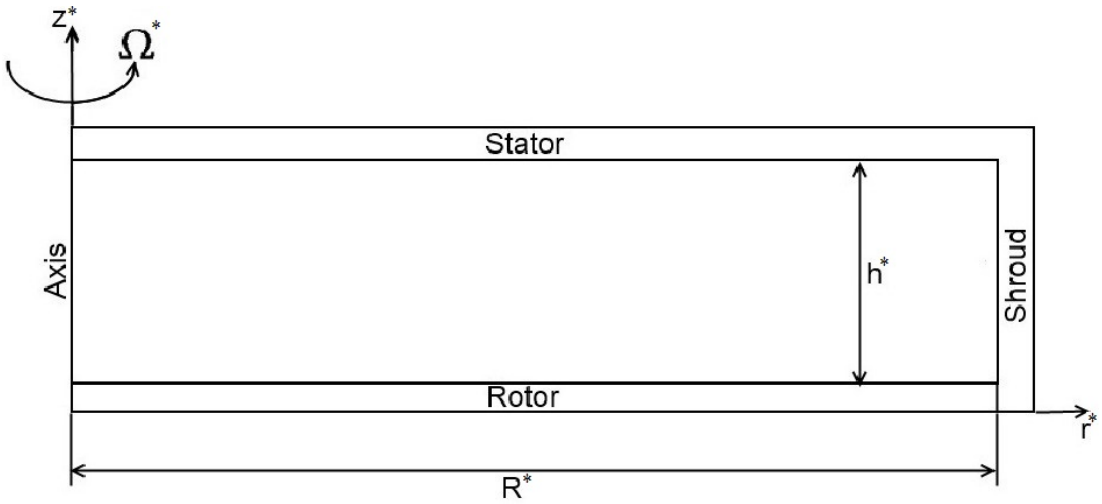

Figure 2.5: Rotor–stator flow configuration.

The rotor–stator flow configuration is shown in Figure 2.5 and the flow is described in the same cylindrical polar coordinates as the free rotating–disk flow. The three velocity components are also defined with the same formulations as in Equation 2.2. The rotor, of radius R^*, in this flow configuration represents the rotating disk with the rotational velocity of Ω^*. The stator and the shroud are stationary walls. In addition to the local rotational Reynolds number Re defined previously for the rotating disk flow in Equation 2.1, the global rotational Reynolds number Re_ϕ is also described to characterize the rotor–stator flow as

$$Re_\phi = \sqrt{\frac{\Omega^* R^{*2}}{\nu^*}}. \tag{2.5}$$

Another flow characteristic of the rotor–stator flow is the aspect ratio D which is defined as

$$D = \frac{h^*}{R^*}, \tag{2.6}$$

where h^* represents the gap between the rotor and the stator disks. In the limit $R^* \to \infty$ and $D \to \infty$, the rotor–stator flow configuration approaches the von Kármán flow where an infinite disk spinning in an unbounded fluid which is at rest sufficiently far above the disk.

Using the flow characteristics, Re_ϕ and D, of the rotor–stator flow, in the limit of $D << 1$, four flow regimes were identified by Daily and Nece (1960) and these are illustrated here in Figure 2.6.

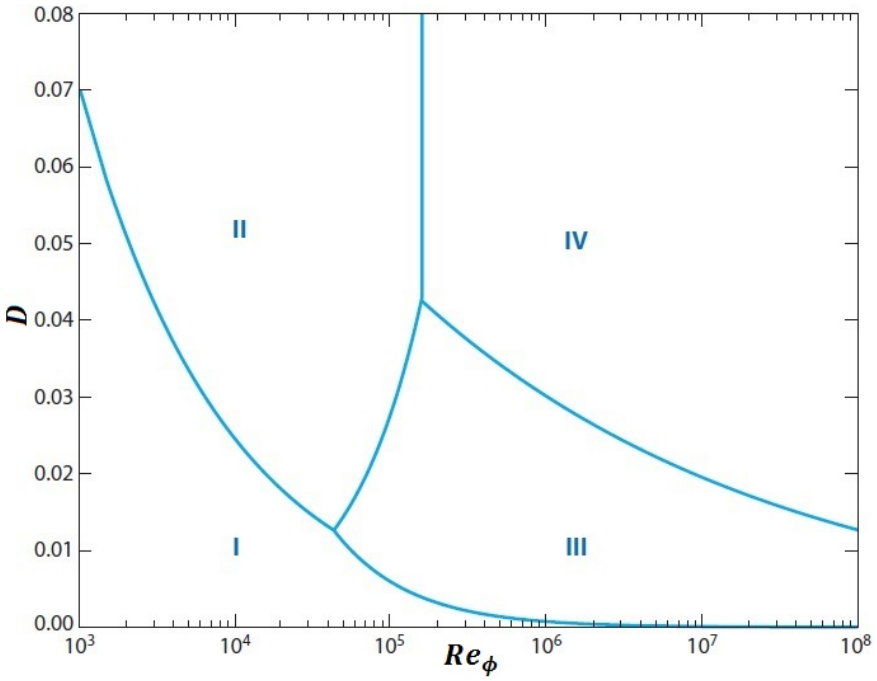

Figure 2.6: The four flow regimes of the rotor–stator flow configuration proposed by Daily and Nece (1960). This figure is reproduced from Launder et al. (2010). Merged boundary layers: I (laminar) and III (turbulent). Unmerged boundary layers: II (laminar) and IV (turbulent).

The aspect ratio in our study is in the range of $0.046 \leq D \leq 0.918$ and the maximum global rotational Reynolds number is $Re_\phi = 600$. Note here that in Figure 2.6, the notation of the global rotational Reynolds number is different (without a root, $Re_\phi = \Omega^* R^{*2}/\nu^*$) from our notation where a root is introduced ($Re_\phi = \sqrt{\Omega^* R^{*2}/\nu^*}$). These two alternative definitions for the Reynolds number

are equally common in the literature on the rotating–disk flow and the rotor–stator flow. However, most seminal studies on the rotating–disk flow in the last two decades, such as Lingwood (1995) and Lingwood and Alfredsson (2015), have been using the definition of the rotational Reynolds number with the root and thus this notation is followed throughout this study. Nevertheless, our global rotational Reynolds number of $Re_\phi = 600$ is equal to $Re_\phi = 3.6 \times 10^5$ in terms of the notation shown in Figure 2.6.

Therefore, according to Figure 2.6, the rotor–stator flow investigated in this research is in Regime IV which indicates that the boundary layers appear over the rotor and the stator are unmerged and thus they are separated with core rotation of the fluid. Additionally, the global rotational Reynolds number in our simulations is high enough for the flow to become turbulent and therefore it represents all types of flow regimes which are laminar, turbulent and transitional. A review of the laminar, transitional and turbulent flows in rotor–stator flow configurations has been published by Launder et al. (2010).

2.4 BEK Family of Flows

The rotor–stator flow configuration, furthermore, represents a broad class of boundary–layer flows, that includes the von Kármán (1921), Ekman (1905) and Bödewadt (1940) flows (Alveroglu et al., 2016). The von Kármán flow has already been described in Section 2.1 but as a reminder there is a stationary fluid above a rotating disk in this flow type. In Bödewadt flow, in contrast with the von Kármán flow, there is a rotating fluid above a stationary disk and in Ekman flow, both the disk and the fluid rotate at approximately equal rates. These three scenarios are commonly referred to as the Bödewadt–Ekman–von Kármán (BEK) family of flows.

In the context of the rotor–stator flow, the boundary layer flow over the rotor is an intermediate state between the von Kármán and Ekman flows. Sim-

ilarly, the boundary layer flow over the stator is an intermediate state between the Bödewadt and Ekman flows. These definitions of intermediate states can be better understood when all of these three flow types are characterized with the Rossby number which is the ratio of inertial forces to Coriolis forces. The definition of the Rossby number is given as, following Lingwood (1997),

$$Ro = \frac{{\Omega_F}^* - \Omega^*}{{\Omega_S}^*}, \tag{2.7}$$

where ${\Omega_F}^*$ and Ω^* are the angular velocities of the fluid and the disk, respectively. The system rotation rate is described with ${\Omega_S}^*$ which is defined as

$$\Omega_S^* = \frac{{\Omega_F}^* + \Omega^*}{4} + \left(\left(\frac{{\Omega_F}^* + \Omega^*}{4} \right)^2 + \frac{\left({\Omega_F}^* - \Omega^*\right)^2}{2} \right)^{1/2}. \tag{2.8}$$

The BEK family of flows, thus, can be represented in terms of the Rossby number:

$$\begin{aligned} \text{von Kármán flow:} \quad & \Omega^* \neq 0, \quad {\Omega_F}^* = 0 \quad \rightarrow \quad Ro = -1 \\ \text{Ekman flow:} \quad & \Omega^* \approx \Omega_F^*, \qquad\qquad\quad \rightarrow \quad Ro = 0 \\ \text{Bödewadt flow:} \quad & \Omega^* = 0, \quad {\Omega_F}^* \neq 0 \quad \rightarrow \quad Ro = 1 \end{aligned} \tag{2.9}$$

Remembering the experimental data produced by Colley et al. (2006) and illustrated in Figure 2.3 of Section 2.2, the angular velocity of the flow over the disk is approximately $G(\zeta) \cong 0.11$ and the angular velocity of the disk is $G(\zeta) = 1$. Thus, by means of Equations 2.7 and 2.8, the Rossby number of the boundary–layer flow over the rotating disk for the experimental facility at Warwick can be found as $Ro \cong -0.92$. This value clearly lies between the values of von Kármán flow ($Ro = -1$) and the Ekman flow ($Ro = 0$) and therefore the meaning of the intermediate state is now explicit. This, furthermore, supports the use of the rotor–stator flow configuration in our numerical investigation to simulate our experiments conducted in water–based experimental facility.

2.5 Hot–Wire Anemometry and Calibration

Hot–wire anemometry is based on convective heat transfer from a heated wire or film component placed in a fluid flow. The basic principles of the hot–wire anemometry and the related heat transfer equations can be found, for instance, in Bruun (1995, p. 19-30). Hot–wire probes are operated mainly in two modes; the constant–current mode, in which the probe temperature varies and the constant–temperature mode, in which the probe temperature is kept virtually constant by varying the current. The constant–temperature type of anemometers are much simpler to use than the constant–current types (Bruun, 1995) and thus most hot–wire measurements are currently conducted with constant–temperature anemometers. Moreover, there are two type of probes (wire and film) used in hot–wire measurements. When the measurements are carried out in air flows, wire probes are usually employed. Whereas, film probes are normally preferred for the liquid flows due to their sturdy construction. Therefore, a constant–temperature anemometer has been used in this study in conjunction with hot–film probes for the measurements carried out in our water–based experimental facility.

The hot–wire anemometer is one of the best measurement techniques for turbulent flows because of its capability to deal with the rapid fluctuations existing in the flow. Despite the fact that such a thin wire/film probe makes it very fragile, it also enables the probe to capture the flow characteristics without disturbing it – mainly in the boundary layers where even a diminutive obstacle can lead to a significant alteration in the flow.

The calibration of hot–wire anemometers is a crucial process in the context of measuring velocities accurately in the boundary layers. This importance becomes even more significant for the measurements of low velocities ($U^* < 3$ m/s) because the conventional calibration techniques, such as wind tunnels, cannot be easily applied. This is due to the small pressure differences occur at these low velocities which are hard to be measured by means of pitot–tubes inside wind tun-

nels and therefore reference velocities for calibration may not be obtained easily (Bruun, 1995). Such low velocities are encountered, for instance, in the boundary layers over rotating disks. Therefore, alternative calibration techniques need to be performed for the measurements in rotating–disk boundary layers.

The calibration apparatus of the rotating disk facility at Warwick was irreversibly broken prior to this research as mentioned in Chapter 1 and thus a new calibration technique has been introduced in this study. It is therefore beneficial to summarize the relevant calibration techniques for low velocities in the literature, including the previous calibration method at Warwick which is currently inoperative.

Essentially, a reference free–stream velocity is needed for the calibration process. However, for the rotating disk flow, there is no free–stream reference velocity outside the boundary layer and thus an in–situ calibration may not be possible and a particular system may be required. Therefore, separate calibration systems may be required in addition to the experimental facility itself.

Pipe flows, for instance, can be used where the hot–film is calibrated against known velocities at the exit of fully–developed laminar pipe flows (Andrews et al., 1972; Lee and Budwig, 1991; Yue and Malmstrom, 1998). Alternatively, Kohan and Schwarz (1973) performed the calibration using the vortex shedding method and this method was most recently improved by Lee and Budwig (1991). In this method, velocities are acquired by measuring the vortex–shedding frequency and then using the Roshko's (Roshko, 1954) Strouhal–Reynolds number (SR) relationship for flow Reynolds numbers ranged between 50 and 150. A laminar plane Couette flow was employed as an alternative method by Aydin and Leutheusser (1980) and Tsanis (1987) for the calibration of the hot–film probe at very low velocities ranged between 0.1 m/s and 0.5 m/s. There are also some commercial calibrators available for low speed calibrations. Christman and Podzimek (1981), for instance, used DISA 55D41/42 calibrator and also Lee and Budwig (1991) compared their calibration results (laminar pipe flow and vortex shedding

method) with TSI 1125 calibrator for the velocity range of $0.02 - 0.9$ m/s.

In all of the preceding calibration methods, the probe is stationary in a known reference flow where the velocity can be controlled. Another approach to calibration is moving the probe in stationary fluid. The most common technique is moving the probe with constant, but variable velocities in a towing tank having stagnant water (Bruun, 1996). As an alternative, Bruun et al. (1989) introduced a swing–arm apparatus for low–speed calibrations. In this method, the anemometer signal is recorded during the motion of the probe at a known path and then these measurements can be evaluated based on an integral procedure between the path and the velocity. Al-Garni (2007) introduced a device with a horizontal arm swinging back and forth around a joint in stagnant air by the rotation of a DC motor at very low velocities ranging from 0 to 0.15 m/s. Özahi et al. (2010) used a rotating–disk method and compared their results with a laminar pipe flow calibration method. In their study, the hot–wire probe was mounted in a hole on the disk which was rotated in stagnant air and anemometer signals were then recorded for the corresponding known velocities.

Nevertheless, the most satisfactory methods are in–situ calibration techniques where the hot–film probes are calibrated directly in the experimental facility itself in which the actual experiments are conducted because otherwise the probes need to be carried each time between the calibration instrument and the experimental rig. This results in the loss of time and the increase in the risk of damaging the probes. However, the preceding calibration methods cannot be performed in–situ for the rotating disk flow investigations. There are few techniques performing the calibration directly in the rotating–disk facility itself.

Colley et al. (1999, 2006), for instance, used the rotating–disk facility at Warwick and traversed the probe across the whole diameter of the water tank with various constant velocities and calibrated their probes in the actual experimental environment. However, this method requires an additional linear motor, traverse and bearing systems apart from the rotational motor, which rotates the disk,

and its bearing. This, obviously, requires an additional cost and maintenance. This linear motor system was irreversibly broken as mentioned previously and is currently inoperative and cannot be employed for the calibration in this research.

Alternatively, Lingwood (1996) and then Imayama et al. (2012) calibrated their hot–wire probe directly in their air–based rotating–disk facilities against the von Kármán flow appears on their rotating disks. Probes, in these studies, were placed inside the rotating disk boundary layer at various locations and aligned correspondingly to face the azimuthal velocity component which was used as a reference velocity for the calibration. Reference velocities (azimuthal component) at the locations of the probes, where the radial and vertical coordinates are known, can be calculated by means of the rotational speed of the disk and the similarity solution by von Kármán. This calibration method seems to be suitable for the air–based rotating–disk facilities because the similarity solution properly represents the actual flow over the disk and thus the theoretically predicted reference velocities used for the calibration correspond to the real values of the velocities existing at these locations of the hot–wire probes. However, remembering Figures 2.3 and 2.4 in Section 2.2, this is not the case for the water–based rotating–disk facilities. The mean flow profiles of the boundary layer, in these facilities, are different from the von Kármán flow and the real values of the azimuthal velocity cannot be predicted theoretically and thus cannot be used as a reference for the calibration. Additionally, the rotating–disk boundary layer is three–dimensional and although the dominant velocity component (azimuthal) is the one used for the calibration, the other two components (radial and axial) may have effects on the probes which are neglected in this calibration technique.

As a result of the above review, a new calibration method had to be introduced in this study which is based on rotating the hot–film probe in still water inside the water tank with various rotational velocities by means of a rotating–arm equipment and recording the corresponding voltage data against the known linear velocities acquired from the rotational speed of the rotating–arm appara-

tus. The details of this calibration technique are proposed in Section 5.5.3 of Chapter 5.

2.6 Instabilities and Transition

Boundary–layer flows over rotating disks with an inflection point on their cross–flow (radial) velocity components (*c.f.* Figure 2.1 in Section 2.1) are prone to instability due to the Rayleigh's inflection–point criterion (Schlichting and Gersten, 2004, p. 432). As a consequence, all boundary–layer flows with a cross–flow component display similar laminar–turbulent transition characteristics associated with the instability arising from the inflection point on the cross–flow velocity profile. This mechanism is called cross–flow instability and considered to be the dominant instability mode for the rotating–disk flow. As a result of the resemblance between the characteristics of the transition process for all boundary layers with a cross–flow component, the rotating–disk flow has become the leading paradigm to study the transition process for these types of boundary layers because it is an easily accessible experimental configuration and because there exists an exact similarity solution.

This cross–flow instability appears as outward–spiralling waves which were first revealed experimentally by Smith (1946) using an hot–wire anemometer. A clear visualization of these spiral waves can be seen in the photo taken from the study by Kobayashi et al. (1980) and illustrated here in Figure 2.7. There are three distinct regions clearly observed in this figure. The laminar regime exists in the centre of the disk, remembering that the Reynolds number is increasing with the radial position (*cf.* Equation 2.1). The turbulent flow occurs near the edge of the disk and these two are separated by the transition region where the spiral waves appear. This flow visualization in Figure 2.7 was obtained by employing titanium tetrachloride on a black painted disk rotating at $\Omega = 30$ rev/s. Titanium tetrachloride in contact with the moist air develops white titanium dioxide

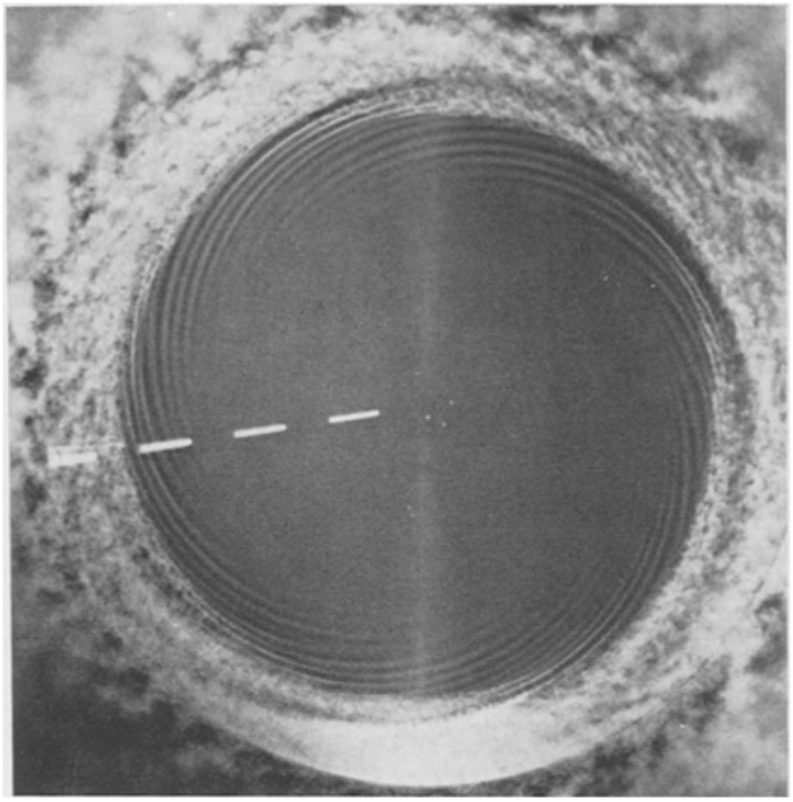

Figure 2.7: Flow pattern on a disk rotating at $\Omega^* = 30$ rev/s. Photo taken from the study by Kobayashi et al. (1980).

powder and thus the flow patterns appears as the motion of white gas which were visualised by means of a stroboscope. When a rotating object is illuminated by means of a stroboscope flashing at a rate equal to the rotation frequency then the object appears stationary. Therefore, the spiral waves observed in this figure are stationary with respect to the rotating disk and thus they are also called stationary modes. The number of these stationary spiral vortices was found to be in the range of between 28 and 31 which is in agreement with the value previously obtained by Gregory et al. (1955). This number of vortices was confirmed later by Kohama (1984) and Wilkinson and Malik (1985) and is considered as standard for the smooth rotating disk, irrespective of the size and the rotational speed of the disk.

Gregory et al. (1955), in their classic paper, provided theoretical analysis with supplementary experimental results and surmised several key features about the cross–flow instability such as the role small surface roughness could have in

fixing the locations of stationary modes. Their surmise was later supported by Wilkinson and Malik (1985) who experimentally observed that stationary modes originated from dust particles on the surface of a 'clean' disk. Subsequently, Fedorov (1988) carried out a linear stability analysis and supported these previous studies by the conclusion that even minute surface roughness can excite the cross–flow instability and therefore this instability is unavoidable and exists at any rotating–disk flow.

In addition to the stationary modes, Gregory et al. (1955) also mentioned the expected existence of travelling modes based on their theoretical analysis but these modes could not be detected in their experiments. Despite the fact that linear theory predicts the travelling modes to be more amplified (Corke and Knasiak, 1998), many experimental studies have concentrated on stationary modes of cross–flow instability. This is due to the susceptibility of this instability to surface roughness as mentioned above. Roughness can increase the amplitude of stationary modes which then cover and fill the entire circumference of the rotating disk. This feature was experimentally observed, for instance, by Wilkinson and Malik (1985) and Jarre et al. (1996b). Therefore, our study has only focused on the stationary modes, however, further information about travelling modes can be found in Reed and Saric (1989) and Corke and Knasiak (1998).

A linear stability analysis of the basic flow, obtained from the similarity solution (Kármán, 1921), was developed by Malik et al. (1981). This stability analysis is used to predict the location of the transition from laminar to turbulent. Other prominent numerical investigations of the linear stability of the von Kármán's flow were performed by Mack (1985), Malik (1986) and Faller (1991). Additionally, the stability of rotating–disk boundary layers was reviewed by Reed and Saric (1989). In the numerical part of our study, the basic flow profiles, obtained from the solution of Navier–Stokes equations by means of the commercial CFD software, ANSYS Fluent, have been subjected to a linear stability analysis using the same numerical code developed by Cooper et al. (2015) and

Garrett et al. (2016). Note here that the velocity profiles in the current study are dependent on the Reynolds number and thus the velocity profiles were averaged first over a range of Reynolds number from $Re = 200$ to $Re = 600$ and then subjected to the linear stability analysis.

Moreover, Lingwood (1995) revealed numerically and subsequently experimentally (Lingwood, 1996) that the rotating–disk flow is absolutely unstable. Thereafter, the rotating–disk boundary–layer flow is known to be liable to two types of instabilities which are convective and absolute. When the disturbance grows spatially from the source and affects the boundary–layer flow in the downstream direction, as in Figure 2.8(a), it is called convective instability. On the other hand, when the disturbance grows in time at fixed radial locations and can affect the flow in both downstream and upstream directions, as in Figure 2.8(b), it is called absolute instability. Formally, the flow is unstable at all Reynolds numbers above a critical value for the onset of convective instability. According to Lingwood (1995, 1997), the critical value of the Reynolds numbers for convective instability is about 290 and that for the absolute instability is 507.3 which was corrected in Lingwood (1997) from the value of 510.6 given in Lingwood (1995). Despite the fact that Lingwood's absolute instability theory indicates that the laminar flow cannot exist above the critical Reynolds number, Davies et al. (2007) revealed numerically that globally stable flow can be obtained even in the presence of absolute instability. Therefore, the role of the absolute instability in the transition process from laminar to turbulent is still unresolved.

In addition to the cross–flow instability, there is another primary mode which is known as streamline–curvature instability. These two modes are also referred as Type–I and Type–II instabilities, respectively. Type–II instability disappears when the Coriolis and streamline–curvature terms are excluded in the stability analyses (Lingwood, 1995) and for the analyses at high Reynolds numbers where the viscous terms are usually neglected (Lilly, 1966). As a result, these two findings support the idea of the Type–II instability being caused by the bal-

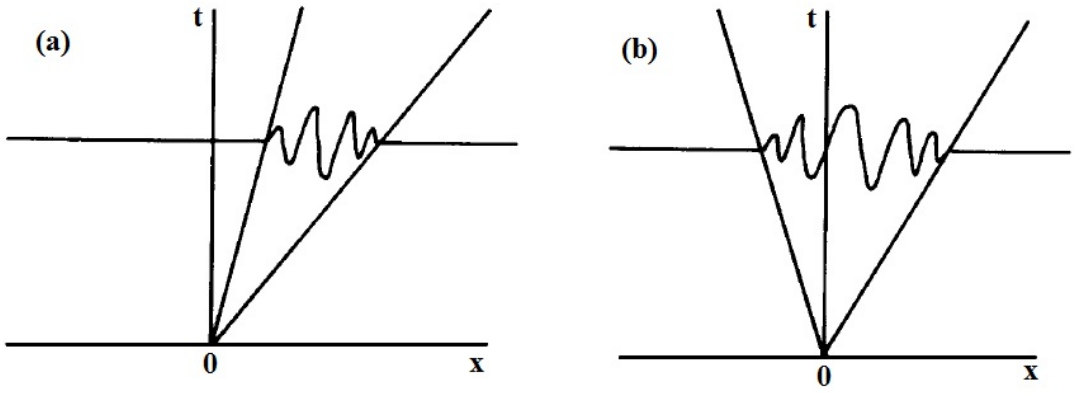

Figure 2.8: Schematic sketches of the evolution of a wave packet generated by an impulse. (a) Convective instability. (b) Absolute instability. Sketch taken from Davies and Carpenter (2003).

ance between viscous and Coriolis effects (Hall, 1986). Nevertheless, the Type–II instability is hardly identified in experiments since the stationary disturbances for this mode have relatively small growth rates and furthermore a comprehensive physical explanation for this instability mode has not yet been provided. The behaviour of the Type–II instability mode, in addition to the Type–I mode, has been investigated in the numerical part of our study in Chapter 4. This investigation may provide better understanding of the physical meaning of Type–II instability because the basic flow profiles, which have been used in the stability analysis, were obtained in the rotor–stator flow configuration which represents a more realistic flow environment than any numerical models which can only be provided by means of many theoretical assumptions.

For the investigation of the transition in the rotating–disk boundary–layer flow, most recently, Imayama et al. (2012) introduced a new way of describing the transition characteristics using an air–based experimental facility. They graphically depicted the phases of transition from laminar to turbulent by means of the probability density function (PDF) contour map of the fluctuating azimuthal disturbance velocity. They first produced the root mean square (rms) profiles of the azimuthal velocity fluctuation for various Reynolds numbers in their study. Figure 2.9, taken from Imayama et al. (2012), illustrates these profiles.

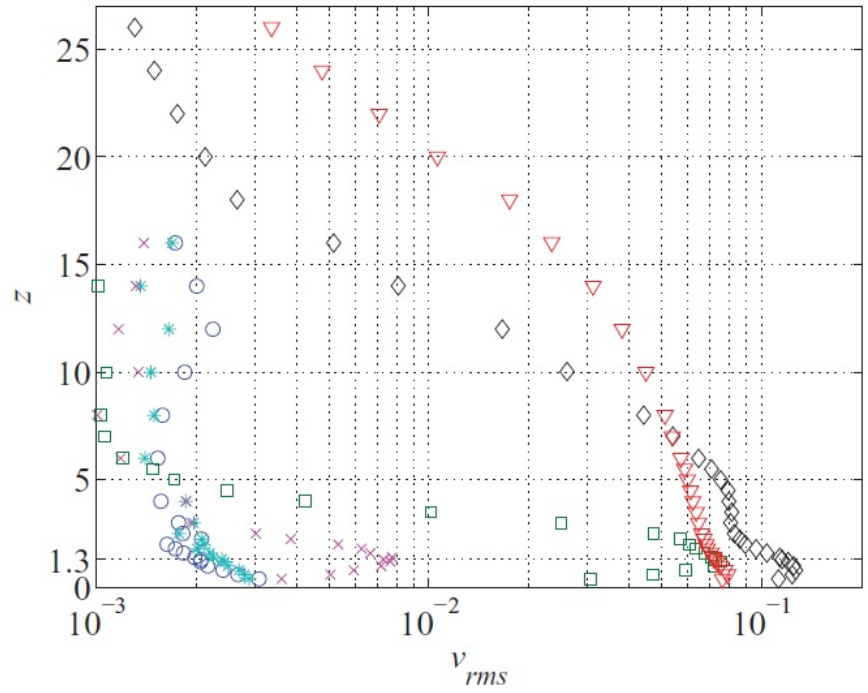

Figure 2.9: Profiles of v_{rms} at $Re = 430$ ($\circ$), $Re = 470$ ($*$), $Re = 510$ ($\times$), $Re = 550$ ($\square$), $Re = 590$ ($\Diamond$), $Re = 630$ (∇). Figure taken from Imayama et al. (2012).

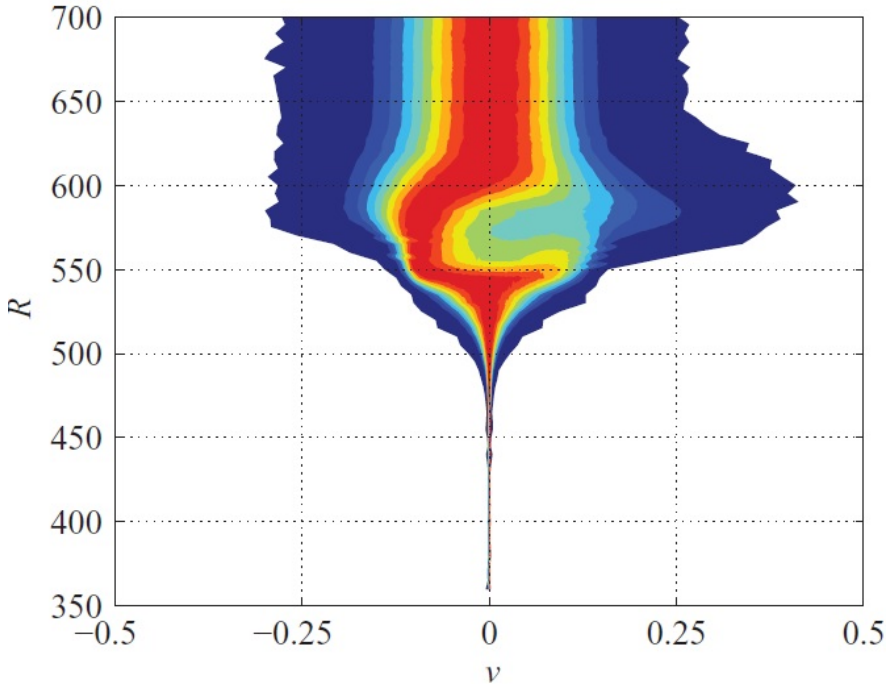

Figure 2.10: The PDF of the azimuthal fluctuation velocity v at $\zeta = 1.3$ normalized with the wall speed. Filled contours indicate 10%, 20%, 30%, 40%, 50%, 60%, 70%, 80%, and 90% of the local PDF value. Figure taken from Imayama et al. (2012).

The y–axis of Figure 2.9, z, is the non–dimensional height ζ in terms of our notation. The x–axis of the same figure represents the rms values of instantaneous azimuthal fluctuation velocity normalized with the wall speed $v_{rms} = v^*_{rms}/(\Omega^* r^*)$. Imayama et al. (2012) reported that, from Figure 2.9, the maximum values of v_{rms} at each Reynolds number seem to appear at approximately $\zeta = 1.3$ and, therefore, they decided to produce the pdf contour map of the azimuthal fluctuation velocity at this non–dimensional height. They produced the pdf contour map shown here in Figure 2.10 which was taken from Imayama et al. (2012). They suggested that this figure reveals the characteristics of the transition process from laminar to turbulent. The highly skewed structures, for instance, at approximately $550 \lesssim Re \lesssim 600$ may give insights into this process. Further information about this new approach can be found in Imayama et al. (2012).

This approach of Imayama et al. (2012) has also been employed in the current study (see Sections 6.5 and 6.9) for the investigation of the boundary–layer transition carried out in the water–based rotating–disk facility which is somewhat different than their air–based facility due to the previously mentioned discrepancies (see Section 2.2).

Chapter 3

Numerical Model

3.1 Introduction

The rotating–disk flow inside the rotor–stator flow configuration was solved using computational fluid dynamics (CFD). In this chapter, the overview of CFD is described and particularly the transition/turbulence model that was used to simulate the flow is presented.

There are various types of CFD software packages such as OpenFOAM, COMSOL, STAR–CCM+, ANSYS Fluent and ANSYS CFX which are widely used both in industry and academia. ANSYS Fluent was used to perform the simulations in this thesis because there exists a powerful transition model called Transition Shear–Stress–Transport (TSST) model (ANSYS Fluent User's Guide, Release 15.0, 2013, p. 717). The details of this model are presented in Section 3.5.

3.2 Computational Fluid Dynamics (CFD)

Computational fluid dynamics (CFD) first appeared approximately in the early 1970s. This method was started to be widely employed by means of the developments in computer science. Due to the rapid increase in the speed of computational process via supercomputers, it is now feasible to simulate extremely

complicated flow characteristics, such as multi–phase flows and turbulent flows. The procedure for the CFD simulations consists of creating the geometry of the problem, dividing the volume occupied by the fluid into discrete cells (the mesh), defining the physical modelling and the boundary conditions and finally solving the equations iteratively. Once the convergence of the iterative solutions of each equation acquired, post–processing of the simulations can be performed.

In the following sections of this chapter, the governing equations (in Section 3.3), the spatial discretization of the fluid volume (in Section 3.4) and particularly the TSST model (in Section 3.5) are described in detail.

3.3 Governing Equations

The governing equations, continuity and momentum (Navier–Stokes) equations, for turbulent flows are provided in Cartesian coordinates (x^*, y^*, z^*) in this section. Nevertheless, these equations are transformed and treated in cylindrical polar coordinates (r^*, θ, z^*) by the CFD software, ANSYS Fluent.

The TSST model used in this study is based on the Reynolds–averaged Navier–Stokes (RANS) equations approach which was first presented by Reynolds (1895). This approach is based on the decomposition of the flow variables into *mean* and *fluctuating* parts, followed by the time averaging. When the time averages of the velocity components u^*, v^* and w^* are denoted as $\overline{u^*}$, $\overline{v^*}$ and $\overline{w^*}$ and the fluctuation velocities are denoted as $u^{*\prime}$, $v^{*\prime}$ and $w^{*\prime}$, the velocity components and the pressure can be written as, following (Schlichting and Gersten, 2004, p. 497–502),

$$u^* = \overline{u^*} + u^{*\prime}, \quad v^* = \overline{v^*} + v^{*\prime}, \quad w^* = \overline{w^*} + w^{*\prime}, \quad p^* = \overline{p^*} + p^{*\prime}. \tag{3.1}$$

where the average is the time average at a fixed point in space and given as, for

instance,

$$\overline{u^*} = \frac{1}{t_1}\int_{t_0}^{t_0+t_1} u^* dt. \tag{3.2}$$

When this integral is taken over an adequately large time interval t_1, the average is independent of the time. Therefore, the averages of the fluctuating variables become zero by definition

$$\overline{u^{*\prime}} = 0, \quad \overline{v^{*\prime}} = 0, \quad \overline{w^{*\prime}} = 0, \quad \overline{p^{*\prime}} = 0. \tag{3.3}$$

In the current study, the turbulent flow is considered to be steady. Additionally, due to the fact that the experiments in water–based facility have been simulated, the fluid domain in simulations is water and thus the flow is incompressible.

As a consequence of these flow conditions and definitions, the continuity equation for turbulent flows is given by

$$\frac{\partial \overline{u^*}}{\partial x^*} + \frac{\partial \overline{v^*}}{\partial y^*} + \frac{\partial \overline{w^*}}{\partial z^*} = 0. \tag{3.4}$$

Momentum equations for turbulent flows are also given by

$$\rho^* \left(\overline{u^*}\frac{\partial \overline{u^*}}{\partial x^*} + \overline{v^*}\frac{\partial \overline{u^*}}{\partial y^*} + \overline{w^*}\frac{\partial \overline{u^*}}{\partial z^*} \right) = -\frac{\partial \overline{p^*}}{\partial x^*} + \mu^* \Delta \overline{u^*} + \left(\frac{\partial {\sigma^*}'_x}{\partial x^*} + \frac{\partial {\tau^*}'_{xy}}{\partial y^*} + \frac{\partial {\tau^*}'_{xz}}{\partial z^*} \right), \tag{3.5}$$

$$\rho^* \left(\overline{u^*}\frac{\partial \overline{v^*}}{\partial x^*} + \overline{v^*}\frac{\partial \overline{v^*}}{\partial y^*} + \overline{w^*}\frac{\partial \overline{v^*}}{\partial z^*} \right) = -\frac{\partial \overline{p^*}}{\partial y^*} + \mu^* \Delta \overline{v^*} + \left(\frac{\partial {\tau^*}'_{xy}}{\partial x^*} + \frac{\partial {\sigma^*}'_y}{\partial y^*} + \frac{\partial {\tau^*}'_{yz}}{\partial z^*} \right), \tag{3.6}$$

$$\rho^* \left(\overline{u^*} \frac{\partial \overline{w^*}}{\partial x^*} + \overline{v^*} \frac{\partial \overline{w^*}}{\partial y^*} + \overline{w^*} \frac{\partial \overline{w^*}}{\partial z^*} \right) = -\frac{\partial \overline{p^*}}{\partial z^*} + \mu^* \Delta \overline{w^*} + \left(\frac{\partial \tau^{*\prime}{}_{xz}}{\partial x^*} + \frac{\partial \tau^{*\prime}{}_{yz}}{\partial y^*} + \frac{\partial \sigma^{*\prime}{}_{z}}{\partial z^*} \right), \tag{3.7}$$

where Δ is the Laplace operator. The stress tensor due to the turbulent velocity components is given by

$$\begin{pmatrix} \sigma^{*\prime}{}_{x} & \tau^{*\prime}{}_{xy} & \tau^{*\prime}{}_{xz} \\ \tau^{*\prime}{}_{xy} & \sigma^{*\prime}{}_{y} & \tau^{*\prime}{}_{yz} \\ \tau^{*\prime}{}_{xz} & \tau^{*\prime}{}_{yz} & \sigma^{*\prime}{}_{z} \end{pmatrix} = - \begin{pmatrix} \rho^* \overline{u^{*\prime 2}} & \rho^* \overline{u^{*\prime} v^{*\prime}} & \rho^* \overline{u^{*\prime} w^{*\prime}} \\ \rho^* \overline{u^{*\prime} v^{*\prime}} & \rho^* \overline{v^{*\prime 2}} & \rho^* \overline{v^{*\prime} w^{*\prime}} \\ \rho^* \overline{u^{*\prime} w^{*\prime}} & \rho^* \overline{v^{*\prime} w^{*\prime}} & \rho^* \overline{w^{*\prime 2}} \end{pmatrix}. \tag{3.8}$$

These stresses are called Reynolds stresses and these momentum equations, correspondingly, are also called Reynolds equations.

There are fundamental difficulties when solving these equations for turbulent flows because the number of unknowns in the equation system is more than the number of equations. Therefore, additional equations are required in order to be able to calculate turbulent flows. There are several turbulence models which provide these additional equations with different approaches. Each of these models can be stronger than the others according to the flow conditions in the simulations. In the context of this study, it is only necessary to know that the TSST model can blend different turbulence models depending on the local flow conditions. Accordingly, it is useful to point out that this model can efficiently simulate the laminar, transitional, and turbulent flow regions in our flow configuration due to this ability of blending different turbulence models as well as switching between the laminar and turbulent solvers.

3.4 Spatial Discretization

The governing equations introduced in Section 3.3 can only be solved numerically by means of dividing the volume, where these equations are applied, into small geometrical elements. These elements are called grid cells and this process is named as grid/mesh generation. This numerical approach is necessary when the analytical methods cannot be employed due to the complexity of the flow geometry and/or conditions, such as transition and turbulence. The spatial discretization schemes can be divided into three major categories: *finite–difference, finite–volume* and *finite–element* schemes. In this study, the fluid domain inside the rotor–stator configuration was divided into hexagonal grid cells and the finite–volume scheme (McDonald, 1971) was employed in order to discretize the governing equations.

The grid on the cross–sectional area of the rotor–stator system in $r^* - \theta$ plane is illustrated in Figure 3.1 as an example. It can be seen from the figure that the central domain of the rotor–stator system was split to form an hexahedron. This enables the grid to be produced as structured hexagonal cells rather than unstructured tetrahedral cells. Otherwise, in the central domain of the system, hexagonal cells cannot be produced smoothly. This split creates a computational advantage since the structured grids are stored in the computer memory with corresponding indexes that represent a linear computational space. This feature facilitates more easy and quick access to the data of the neighbouring cells. Thus, the calculation of the gradients, fluxes and also the application of the boundary conditions are immensely simplified (Blazek, 2015, p. 33).

Figure 3.2 shows the grid also on the cross–sectional area of the rotor–stator system in $r^* - z^*$ plane. In order to obtain better resolution inside the boundary layers on the rotor (this is the lower limit of the z^*–coordinate where $z^* = 0$ in Figure 3.2) and on the stator (this is the upper limit of the z^*–coordinate in Figure 3.2), the grid is stretched accordingly. There are 20 grid cells inside

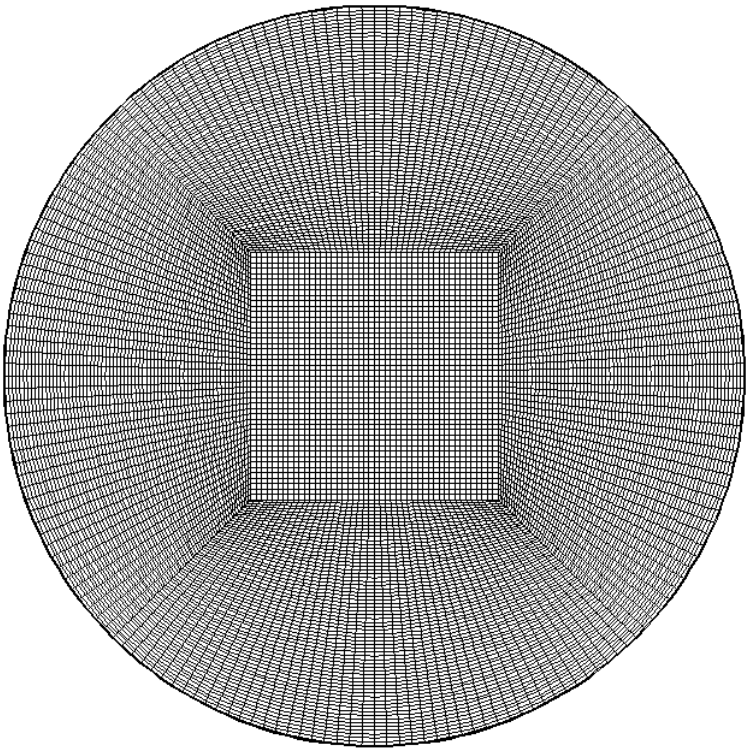

Figure 3.1: The grid on the cross–sectional area of the rotor–stator flow configuration in $r^* - \theta$ plane.

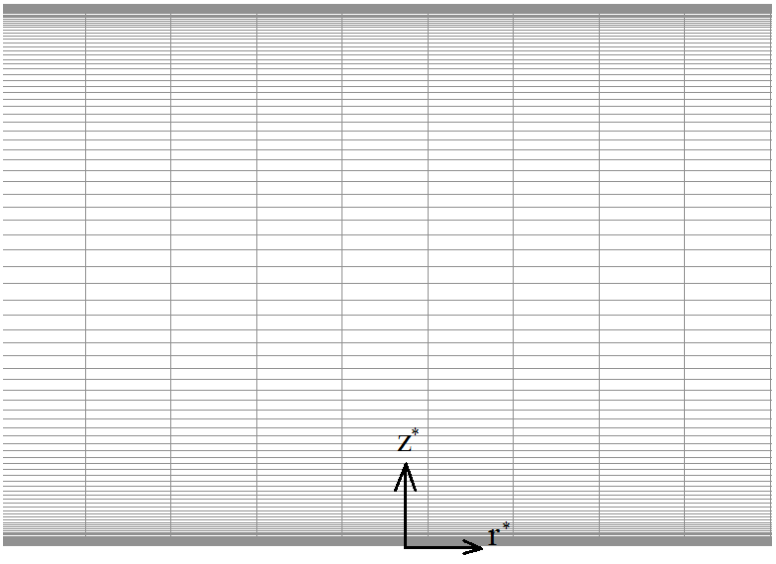

Figure 3.2: A part of the grid on the cross–sectional area of the rotor–stator flow configuration in $r^* - z^*$ plane.

each of the boundary layers on both the rotor and the stator. The volume of the cells are larger in the central domain of the flow configuration where the accuracy and the resolution of the solution are relatively less significant than inside the boundary layers and therefore the total number of required cells for the whole domain can be reduced.

In order to achieve grid–independent results, about 1,800,000 hexagonal grid cells were generated in total. This total number of grid cells was obtained after iterative simulations where the mesh was adapted at each iteration. This iterative approach was carried out until the difference between the iterative results, for instance the velocity profiles, can be neglected. The quality of the grid was measured by the value of *orthogonality*. The mesh orthogonality indicates how close the angles between adjacent faces of a grid cell to an optimum angle which is 90° for quadrilateral faced elements. As a result, this quantity shows the degree of deviation from an orthogonal intersection which ranges from zero (represents a poor quality), to one (indicates the ideal case). The detailed explanation and formulation of orthogonality can be found, for instance, in Alter (2004). The minimum value of the orthogonality in the current study is 0.7172 which is considered to be adequate due to the fact that typical grids range from 0.6 to 0.8 (Alter, 2004).

Moreover, the gradients were evaluated by the least–squares cell–based approach which was initially presented by Barth (1991) and the discretization of the governing equations were employed by means of a coupled *pressure–based* scheme (Chen and Przekwas, 2010).

3.5 Transition–SST Model

The Transition–Shear–Stress–Transport (TSST) model used in this study is based on empirical correlations and it was developed by Langtry and Menter (2009). These empirical correlations are defined based on the T3B, T3A, T3A-

, and the Schubauer and Klebanoff (1955) flat–plate test cases, however, the model can also be extended to flows with rough walls and to flows with crossflow instability (Langtry and Menter, 2009). The TSST model is a coupling model of the Shear–Stress–Transport (SST) $k-\omega$ model which was introduced by Menter (1994) with the two additional transport equations using only the local variables, i.e. the intermittency factor γ and the transition onset criteria, in terms of momentum thickness Reynolds number $\tilde{Re}_{\theta_t}$.

The SST $k-\omega$ model by Menter (1994) can successfully combine the standard $k-\omega$ model (Wilcox, 1998), which is strong and precise in the near wall region, and the standard $k-\epsilon$ model (Launder and Spalding, 1974) with its freestream independence in the far field. Transport equations for the turbulence kinetic energy k, the dissipation rate ϵ, and the specific dissipation rate ω of these two turbulence models are not included here for simplicity but they can be found, for instance, in Wilcox (1998, p. 119–125).

The intermittency factor γ is one of the local variables and defined as the quality of being intermittent, i.e. it gives the fraction of time for which there is turbulent flow at a particular position (Schlichting and Gersten, 2004, p. 418). Therefore, $\gamma = 1$ indicates a turbulent flow and $\gamma = 0$ shows a laminar flow. A transitional flow exists between these two values. The transport equation for the intermittency is used to locally trigger transition. It is now widely agreed that any turbulence model, excluding the intermittency equation, seems to be an unreliable method of predicting transition (Langtry and Menter, 2005). The transport equation for the intermittency γ is given as

$$\frac{\partial\left(\rho^{*}\gamma\right)}{\partial t}+\frac{\partial\left(\rho^{*}U_{j}^{*}\gamma\right)}{\partial x_{j}^{*}}=P_{\gamma}-E_{\gamma}+\frac{\partial}{\partial x_{j}^{*}}\left[\left(\mu^{*}+\mu_{t}^{*}\right)\frac{\partial\gamma}{\partial x_{j}^{*}}\right], \tag{3.9}$$

where μ^{*} and μ_{t}^{*} are molecular and eddy viscosities, respectively and P_{γ} is the transition source and described as

$$P_\gamma = 2F_{length}\rho^* S\left[\gamma F_{onset}\right]^{0.5}(1-\gamma)\,, \tag{3.10}$$

where S is the strain–rate magnitude and defined as

$$S = \sqrt{2S_{ij}S_{ij}}, \tag{3.11}$$

where S_{ij} is the strain–rate tensor and given by,

$$S_{ij} = 0.5\left(\frac{\partial u_i^*}{\partial x_j^*} + \frac{\partial u_j^*}{\partial x_i^*}\right). \tag{3.12}$$

Additionally, F_{length} and F_{onset}, in Equation 3.10, are empirical correlations which manage the length of the transition region and the transition onset location, respectively. These are non–dimensional terms and employed to control the intermittency equation in the boundary layer. These terms are defined in Equations A.1–A.6 and A.7 in the Appendix. The destruction/relaminarization source term E_γ, in Equation 3.9, is given by

$$E_\gamma = 0.06\rho^*\Omega\gamma F_{turb}\left(50\gamma - 1\right), \tag{3.13}$$

$$F_{turb} = e^{-\left(\frac{R_T}{4}\right)^4}. \tag{3.14}$$

where Ω is the vorticity magnitude and R_T is defined in Equation A.4 in the Appendix.

The critical Reynolds number where the intermittency first begins to grow in the boundary layer is illustrated with Re_{θ_c}. This occurs upstream of the local transition onset momentum–thickness Reynolds number $\tilde{Re}_{\theta_t}$ that is obtained from the transport equation displayed in Equation 3.15. Both the F_{length} and the Re_{θ_c} are functions of $\tilde{Re}_{\theta_t}$ which are based on the experimental test cases by Schubauer and Klebanoff (1955) and these empirical correlations are described

with the conditional functions given in Equations A.7 and A.8 in the Appendix.

The second transport equation of the TSST model for the local transition onset momentum–thickness Reynolds number, $\tilde{Re}_{\theta_t}$, is defined as

$$\frac{\partial\left(\rho^{*}\tilde{Re}_{\theta_t}\right)}{\partial t}+\frac{\partial\left(\rho^{*}U_{j}^{*}\tilde{Re}_{\theta_t}\right)}{\partial x_{j}^{*}}=P_{\theta_t}+\frac{\partial}{\partial x_{j}^{*}}\left[2\left(\mu^{*}+\mu_{t}^{*}\right)\frac{\partial\tilde{Re}_{\theta_t}}{\partial x_{j}^{*}}\right]. \tag{3.15}$$

The source term, P_{θ_t}, in Equation 3.15 is expressed as

$$P_{\theta_t}=0.03\frac{\rho^{*}}{t}\left(Re_{\theta_t}-\tilde{Re}_{\theta_t}\right)\left(1.0-F_{\theta_t}\right), \tag{3.16}$$

where the time scale t exists due to dimensional reasons and is given by

$$t=\frac{500\mu^{*}}{\rho^{*}U^{*2}}, \tag{3.17}$$

where U^{*} is the local velocity. Furthermore, Re_{θ_t}, in Equation 3.16, is the transition onset momentum thickness Reynolds number based on free–stream conditions. F_{θ_t}, in the same equation, is called the blending function which is equal to zero in the free–stream and one in the boundary layer to propagate the transported scalar $\tilde{Re}_{\theta_t}$. This blending function is given by

$$F_{\theta_t}=min\left(max\left(F_{wake}\cdot e^{-\left(\frac{y}{\delta_2}\right)^{4}},1.0-\left(\frac{\gamma-1/50}{1.0-1/50}\right)^{2}\right),1.0\right). \tag{3.18}$$

The boundary layer thickness δ_2, in Equation 3.18, is different from the usual boundary layer thickness previously defined for the rotating–disk flow and this new variable is given by

$$\delta_2=\frac{50\Omega y}{U^{*}}\frac{15}{2}\frac{\tilde{Re}_{\theta_t}\mu^{*}}{\rho^{*}U^{*}}. \tag{3.19}$$

F_{wake}, in Equation 3.18, deactivates the blending function in the wake regions

downstream of, for instance, an aerofoil:

$$F_{wake} = e^{-\left(\frac{Re_\omega}{1E+5}\right)^2}, \qquad Re_\omega = \frac{\rho^* \omega y^2}{\mu^*}. \tag{3.20}$$

In addition to the previously defined empirical correlations, F_{lenght} and Re_{θ_c}, the third correlation Re_{θ_t}, which is used in Equation 3.16, is described as a function of turbulence intensity Tu and the pressure gradient parameter λ_θ:

$$Tu = 100\frac{\sqrt{2k/3}}{U^*}, \tag{3.21}$$

$$\lambda_\theta = \frac{\rho^* \theta^2}{\mu^*}\frac{dU^*}{ds}, \tag{3.22}$$

where dU^*/ds is the acceleration in stream–wise direction and θ is the momentum thickness. The empirical correlation of the Re_{θ_t} is given in Equation A.9 in the Appendix.

Moreover, for the cases of the separation induced transition, the following modification to the intermittency, γ, is necessary:

$$\gamma_{sep} = min\left(2 \cdot max\left[0, \left(\frac{Re_V}{3.235 Re_{\theta_c}}\right) - 1\right] F_{reattach}, 2\right) F_{\theta_t}, \tag{3.23}$$

$$F_{reattach} = e^{-\left(\frac{R_T}{20}\right)^4}, \tag{3.24}$$

$$\gamma_{eff} = max\left(\gamma, \gamma_{sep}\right). \tag{3.25}$$

Eventually, the presented TSST model is combined with the SST turbulence model (Menter, 1994) by modifying the transport equation of the turbulence kinetic energy k in the SST $k-\omega$ model. The modification is represented below in Equation 3.26 but the detailed rationale can be found in Menter et al. (2006).

$$\frac{\partial}{\partial t}\left(\rho^* k\right) + \frac{\partial}{\partial x_j^*}\left(\rho^* u_j^* k\right) = \tilde{P}_k - \tilde{D}_k + \frac{\partial}{\partial x_j^*}\left(\left(\mu^* + \sigma_k \mu_t^*\right)\frac{\partial k}{\partial x_j^*}\right), \tag{3.26}$$

$$\tilde{P}_k = \gamma_{eff} P_k, \qquad \tilde{D}_k = min\left(max\left(\gamma_{eff}, 0.1\right), 1.0\right) D_k, \tag{3.27}$$

P_k and D_k are the original production and destruction terms for the SST model and σ_k is the turbulent Prandtl number for k. The detailed expressions of these terms can be found in ANSYS Fluent Theory Guide, Release 15.0 (2013, p. 60-64).

3.6 Surface Roughness

Due to the fact that the surface roughness in reality can be formed from infinite number of possible shapes, a standard roughness needs to be defined in the computational approaches to describe the effect of roughness on a flow. Therefore, a standard form of roughness was introduced in literature, as illustrated in Figure 3.3 (Schlichting and Gersten, 2004, p. 527). The surface is assumed to be covered with a layer of spheres packed which resembles more like the surface of sandpaper. Therefore, this standard form of roughness is called *sand roughness* and the diameter of the spheres is called the *sand roughness height* and/or *sand–grain roughness height*, denoted by k_s. Any technical surface roughness can be transformed into this standard roughness with a so–called *equivalent sand–grain roughness height* denoted as k_{seq}. The relevant formulations and the tables to perform this transformation can be found, for instance, in Schlichting and Gersten (2004, p. 529-532).

In our simulations, instead of the equivalent sand–grain roughness height, the real geometric roughness height, denoted by K, was used directly and thus the transformation was not necessary. The rationale behind this is that, as mentioned

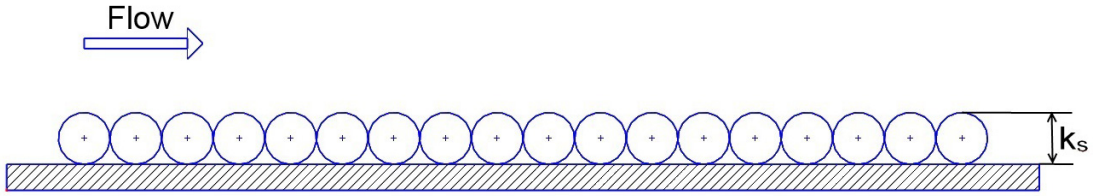

Figure 3.3: Demonstration of sand roughness.

previously in Section 3.5, the TSST model is based on empirical correlations which were obtained from experiments using the real forms and thus heights of surface roughness.

Wilcox (1998) reported that a main benefit of the $k-\omega$ turbulence model over the $k-\epsilon$ formulation is that the ω–oriented equations have solutions in which the value of ω can be randomly defined at the wall. Due to this advantage, the influence of surface roughness can be incorporated naturally (Saffman, 1970). The surface boundary condition on ω is defined as

$$\omega_w = \frac{u^{*2}_{\tau}}{\nu^*} S_R, \tag{3.28}$$

where u^*_τ is the friction velocity and given as

$$u^*_\tau = \sqrt{\frac{\tau^*_w}{\rho^*}}, \tag{3.29}$$

where τ^*_w is the shear stress on the wall and described with the Newton's law of viscosity as follows:

$$\tau^*_w = \mu^* \left.\frac{\partial u^*}{\partial y^*}\right|_{y^*=0}. \tag{3.30}$$

The implementation of a specific dissipation at the surface, as shown in Equation 3.28, results in an increased turbulence compared to a smooth surface and therefore higher momentum transfer towards the wall (Aupoix, 2014). S_R, in Equation 3.28, is a function of non–dimensional surface roughness and defined as

$$S_R = \begin{cases} \left(50/k_S^+\right)^2, & k_S^+ < 25 \\ 100/k_S^+, & k_S^+ \geq 25 \end{cases}, \tag{3.31}$$

where k_S^+ is the non–dimensional sand–grain roughness height and given by

$$k_S^+ = \frac{u_\tau^* k_s}{\nu^*}. \tag{3.32}$$

Based on the non–dimensional sand–grain roughness height k_S^+, there are three conditions which correspond to three regimes; hydraulically smooth regime: $0 \leq k_s^+ \leq 5$, transition regime: $5 < k_s^+ < 70$ and fully–rough regime: $70 \leq k_s^+$ (Schlichting and Gersten, 2004, p. 529). In the hydraulically smooth regime, the case is similar to the ideal smooth surface, whereas roughness effects arise in the transition region. Then the flow becomes independent of the Reynolds number in the fully–rough regime since the viscosity effects disappear.

Wilcox (1998) stated that this approach has been validated for a maximum k_s^+ value of 400 and both attached and separated flows can be properly simulated with this model. Thus, it can be employed even for smooth surfaces where $k_s^+ \leq 5$. In ANSYS Fluent, Wilcox's model is implemented in two different techniques. First one is the modification of the model to employ the wall functions for big values of $y+$, however, this technique was not necessary in our simulations since the $y+$ value is less than one. Secondly, the lower limiting value for k_s^+ is modified to be limited to 1 by the below arrangement:

$$k_s^+ = max\left(1.0; \frac{u_{\tau k_s}^*}{\nu^*}\right). \tag{3.33}$$

However, this was not a restriction in the context of our study because the lower geometric roughness height used in the simulations was $K = 100\mu m$ which corresponds to $k_s^+ \cong 2.5$. This value is larger than the above mentioned lower limitation.

Hellsten and Laine (1997) reported that the SST model is not appropriate to simulate the rough surfaces because the SST limitation based on Bradshaw's assumption, which is that the turbulent shear stress is proportional to the turbulent kinetic energy (Bradshaw et al., 1967), causes under–prediction of roughness effects, for instance, skin friction. The modification of roughness modelling by Hellsten and Laine (1997) was implemented by means of a user–defined–function in ANSYS Fluent by Ferrer and Munduate (2009). They compared their results with the default roughness modelling of ANSYS Fluent, which is based on the approach by Wilcox (1998), and revealed that this correction is not essential. Therefore, the modification by Hellsten and Laine (1997) was not considered in this study.

The above mentioned roughness modelling based on Wilcox (1998) is satisfactory once the boundary–layer flow becomes fully turbulent. The roughness effect on the transition process, furthermore, can be captured by means of the modification to the correlation for the transition onset momentum thickness Reynolds number Re_{θ_t}. This modification is possible with an additional transport equation for the variable called *Roughness Amplification* and denoted by A_r. This additional equation was initially proposed by Dassler et al. (2010) and is given by

$$\frac{\partial\left(\rho^* A_r\right)}{\partial t} + \frac{\partial\left(\rho^* U_j^* A_r\right)}{\partial x_j^*} = P_{AR} + \frac{\partial}{\partial x_j^*}\left[20\left(\mu^* + \mu_t^*\right)\frac{\partial A_r}{\partial x_j^*}\right], \tag{3.34}$$

where P_{AR} is the source term and generates a transition amplifying variable A_r in the vicinity of rough walls. This variable is then transported through the flow by means of the convective and diffusive terms of the equation. The source term P_{AR} is only applied to the wall–adjacent cells and is a function of y^+ and k_s^+ that is given by

$$P_{AR} = \frac{2.0}{1.0 + e^{(-y^{+} \cdot 7.0 + 7.0)}} \cdot \frac{11000.0}{1.0 + e^{\left(-k_s^{+} \cdot 1.0 + 11.1\right)}}. \tag{3.35}$$

To implement this new variable A_r into the transport equation of $\tilde{Re}_{\theta_t}$ (Equation 3.15), a new variable is defined as

$$Arg_r = max\left(\frac{A_r - 2.0}{2.0}, 0.0\right). \tag{3.36}$$

This new variable ensures that only A_r values bigger than two and only positive values are considered. With increasing the roughness height and thus increasing the A_r values, the source term P_{θ_t} in Equation 3.15 becomes negative by means of Equation 3.37 below and the transported scalar $\tilde{Re}_{\theta_t}$ is, thus, reduced. As a result, the transition onset is triggered.

$$P_{\theta_t} = -10.0 \cdot Arg_r, \qquad F_{\theta_t} > 0.99. \tag{3.37}$$

The constants in empirical correlations, i.e. the modelling parameters of the TSST model, are fixed in the numerical simulation code, and hence non–adjustable. However, the robustness of the TSST model to perform simulations that include the effect of surface roughness has recently been confirmed by Aldaş and Yapıcı (2014). They numerically investigated the effects of surface roughness on efficiency of water jet pumps by means of various turbulence model options of ANSYS Fluent and compared these numerical results with the experimental data from the literature. They have found that the TSST model provided results closer to the experiments than the other turbulence models. The TSST model was also used by Ferrer and Munduate (2009) for the predictions of transition under the effect of distributed roughness covering the surface of a wind turbine blade. Although the flow over wind turbine blades is a paradigm of a three–dimensional rotating–disk flow, Ferrer and Munduate (2009) performed two–dimensional simulations which does not represent this paradigm. Therefore, apart from our own

study (Özkan et al., in press), we are not aware of any research that investigates the effect of surface roughness on a three–dimensional rotating–disk flow by means of the TSST model.

Chapter 4

Numerical Results

In the current study, although the whole system of equations were numerically solved for the three–dimensional flow domain, only the azimuthal and the radial velocity components are displayed in the results since for the rotating–disk flow these are the dominant flow components and one can usually only measure these two components experimentally in rotating–disk boundary–layer experiments.

4.1 Flow Field

The contour plot of the velocity on the cross–sectional area (r^*–z^*–plane) of the rotor–stator flow configuration is shown in Figure 4.1 for the gap width of $h^* = 40\delta$ and the rotational speed of $\Omega^* = 1$ rad/s which corresponds to the global rotational Reynolds number of $Re_\phi = 600$ where the radius of the system is equal to $R^* = 0.6$ m.

In this figure, the x–axis shows the radial location r^* and the y–axis indicates the vertical position z^* in the flow field. Here, $r^* = 0$ m indicates the centre of the disk, i.e. rotation axis and the stationary annular shroud is displayed with $r^* = \pm 0.6$ m. The rotor and the stator disks are located at $z^* = 0$ m and $z^* = 0.22$ m, respectively. Boundary layers, especially the one on the rotor,

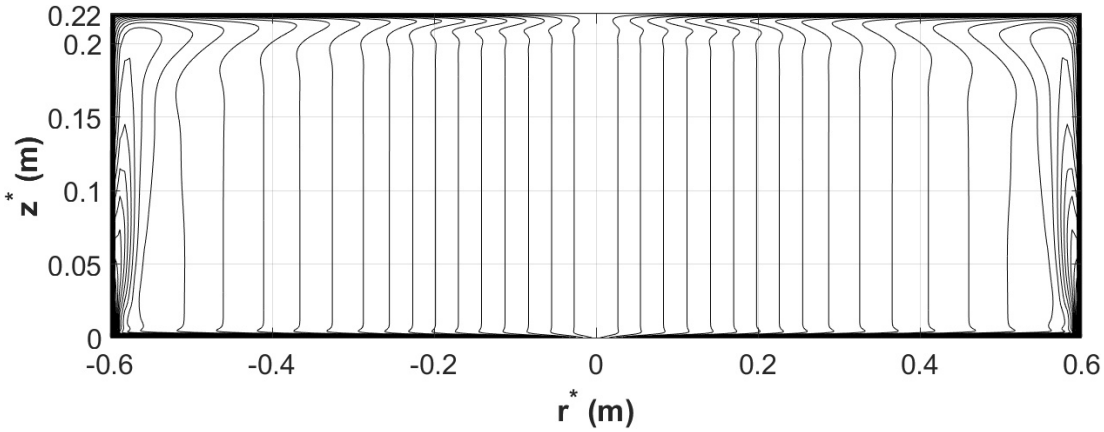

Figure 4.1: Flow field on the cross–sectional area (r^*–z^*–plane) of the rotor–stator flow configuration. $\Omega^* = 1$ rad/s, $Re_\phi = 600$, $h^* = 40\delta$, $D = 0.367$.

are very thin and thus may be hard to be observed from the figure. However, the orientation of the boundary layer flow on the rotor can still be recognized from the centre to the edge of the disk, whereas the flow in the boundary layer on the stator has the opposite orientation whereby the fluid flows towards the centre of the stator disk. As a result of the finite size of the flow geometry, small cavities occur near the stationary annular shroud but they do not have effect on the large portion of the main flow. The distortion of the main flow due to the stationary annular shroud, for instance, seems to start at the radial location of approximately $r^* \approx 0.58$ which corresponds to the local Reynolds number of $Re \approx 580$. This is a reasonable value in the context of the current study since the numerical results were produced up to the maximum Reynolds number of 546 which is adequately away from the affected field.

In addition to the velocity field, it is beneficial to illustrate the laminar, transitional and turbulent flow regimes over the rotating disk in the rotor–stator flow configuration. Figure 4.2 shows the change of the intermittency factor γ in the radial direction r^* inside the boundary layer of the rotor. Laminar and turbulent regions can clearly be seen in the figure where $\gamma \cong 0$ and $\gamma = 1$, respectively, and these two flow regimes are separated by the transitional flow where $0 < \gamma < 1$. As a reminder, the definition of the intermittency factor γ was provided in Section 3.5.

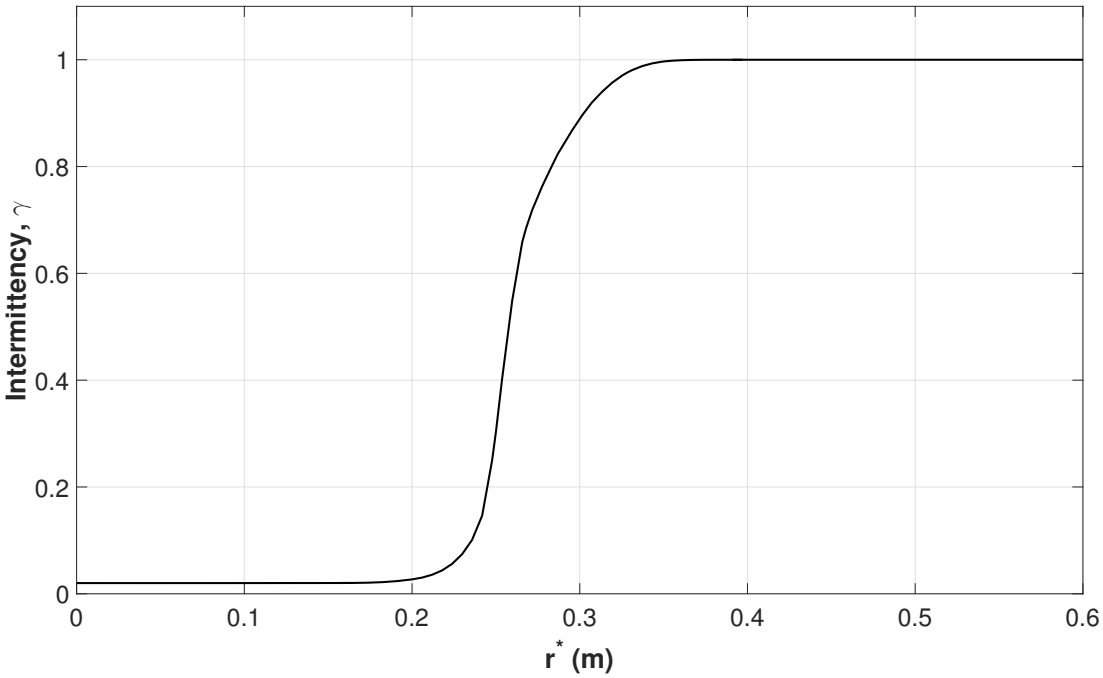

Figure 4.2: The change of intermittency factor γ in the radial direction r^*. Laminar region: $\gamma \cong 0$; Transition region: $0 < \gamma < 1$; Turbulent region: $\gamma = 1$. $\Omega^* = 1$ rad/s, $Re_\phi = 600$, $h^* = 40\delta$, $D = 0.367$.

4.2 Validation of the Computational Approach

4.2.1 Comparison of TSST Results with Numerical and Experimental Literature Data

The results of the current study have been compared with the available data in literature for validation. Figures 4.3(a) and 4.3(b) compare our TSST simulations with the numerical results of Vaughan (1986) and the experimental data of Sambo (1983). These figures show the radial velocity component F in Figure 4.3(a) and the azimuthal component G in Figure 4.3(b) for the entire extend of the gap in the rotor–stator flow as a function of the normalized height z^*/h^*. The two opposing boundary layers, which were indicated and shown previously in Section 4.1 and in Figure 4.1, on the rotor ($z^*/h^* = 0$) and the stator ($z^*/h^* = 1$) can be observed in both Figures 4.3(a) and 4.3(b). In Figure 4.3(b), for instance, two boundary layers are separated with core rotation of the fluid where its rotational speed is of the order of approximately $G(z^*/h^*) \approx 0.35 - 0.4$.

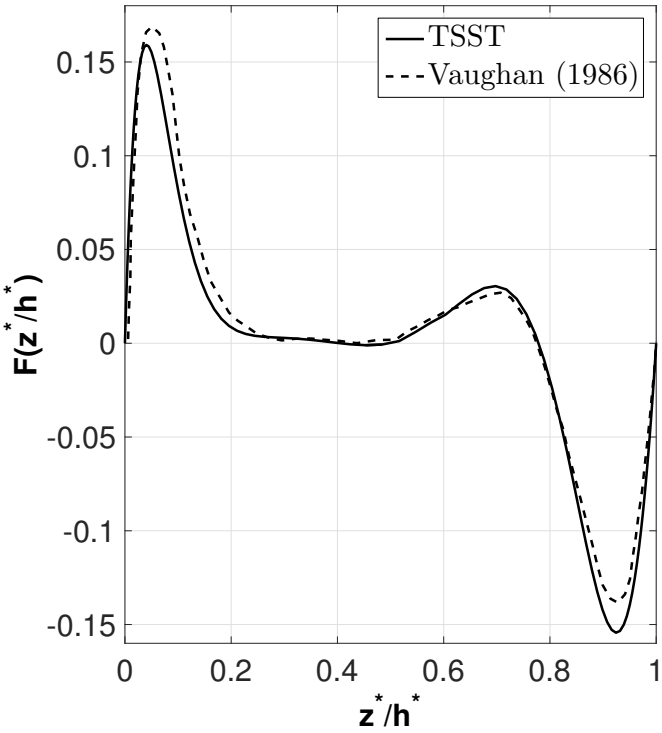

(a) Radial velocity F, at $Re = 112$.

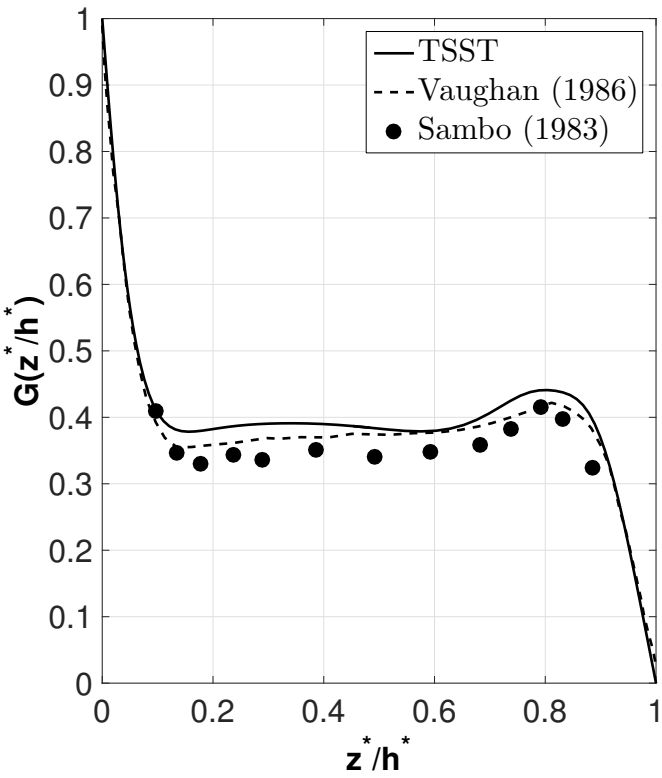

(b) Azimuthal velocity G, at $Re = 134$.

Figure 4.3: Comparison of the results of the TSST simulation with previous numerical (Vaughan, 1986) and experimental (Sambo, 1983) data ($Re_\phi = 224$ and $D = 0.1$).

The data of Vaughan (1986) and Sambo (1983) were obtained and reproduced from Owen and Rogers (1989, p. 138).

Sambo (1983) produced the experimental data by means of an air–based rotor–stator system. The flow velocity within this air-filled flow configuration was measured by means of a Laser-Doppler Anemometry (LDA) system. The radius of the rotor–stator system was $R^* = 190.5$ mm and the gap width was $h^* = 19$ mm; giving an aspect ratio of $D = 0.1$. The radial flow component was obtained at the radial location $r^* = 0.5R^*$ and the azimuthal component was acquired at $r^* = 0.6R^*$. The global rotational Reynolds number had a value of $Re_\phi = 224$. Assuming that the experiments were conducted approximately at a room temperature of 20°C, where the kinematic viscosity of air is 1.51^{-5} $\mathrm{m^2 s^{-1}}$, this value of Re_ϕ indicates a rotational velocity of $\Omega^* = 20.8$ rad/s equivalent to, approximately, 200 rev/min. The measurement locations of the radial and the azimuthal velocity components are, therefore, equal to the local Reynolds numbers of $Re = 112$ and $Re = 134$, respectively. Vaughan (1986) subsequently developed a finite-difference solver for the Navier–Stokes equations to model the flow within Sambo's system.

Figures 4.3(a) and 4.3(b) display a very good qualitative and quantitative agreement between the current TSST simulations and the numerical data of Vaughan (1986) for both the radial and the azimuthal velocity components. The maximum discrepancies between the results of both models occur near the maxima of the radial flow component, that is near $z^*/h^* \approx 0.05$ and $z^*/h^* \approx 0.95$, and in the vicinity of $z^*/h^* \approx 0.18$ for the azimuthal flow component. Here the differences are of the order of approximately 1%, or less, for the radial component and about 4% for the azimuthal component. Owen and Rogers (1989, p. 138) only display experimental data for the azimuthal velocity component from Sambo (1983) and Figure 4.3(b) reveals that, similar to the results of Vaughan (1986), the present simulations compare well to his experiments.

4.2.2 Comparison of TSST Results with Experimental Data of Colley et al. (2006) and von–Kármán Flow

The flow configurations of Colley et al. (2006) were previously mentioned in Sections 2.2 and 2.4. As a reminder, they obtained their results with two moderately different experimental configurations. One of these configurations is that the disk was rotating freely under water. In the other case, the flow over the rotating disk was enclosed with a stationary lid to minimize the disturbances which arise from the free surface of water and affect the boundary layer on the rotating disk. This second experimental facility, therefore, resembles the rotor–stator flow configuration which was previously shown in Figure 2.5. These two experimental facilities of Colley et al. (2006) with and without the stationary lid are referred to as *stator* and *no–stator*, respectively, in the current study. However, note here that the flow system of Colley et al. (2006) with the stationary lid had a small annular opening of approximately $10-20$ mm between the rotating disk and the stationary lid. Therefore, there may have been some exchange of water through this circumferential gap. When this gap is neglected, the aspect ratio of their system was $D = 0.1$ since the gap between the stationary lid and the rotating disk was $h^* = 0.02$ m which corresponded to 10δ in terms of the boundary-layer thickness.

The data from Figure 2 in Colley et al. (2006), for both their experimental systems, are included here in Figures 4.4 and 4.5 in comparison with the computational results obtained from our TSST simulations and the theoretical data of von Kármán flow. Moreover, Figure 4.4 shows the TSST simulations for $D = 0.092$, $h^* = 10\delta$, while Figure 4.5 includes corresponding simulations for $D = 0.918$, $h^* = 100\delta$. Both figures, furthermore, emphasize the Reynolds number dependence by including TSST simulations for $Re = 210$ and for $Re = 546$. Here the lower Reynolds number corresponds to a radial location within the laminar region of the boundary layer while the higher Reynolds number is associated

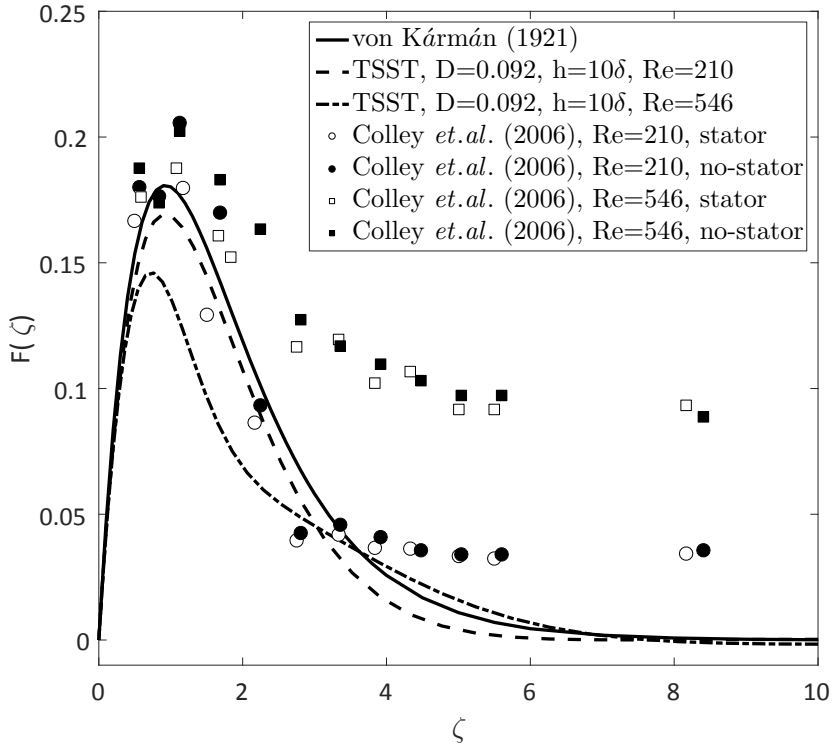

(a) Radial velocity F

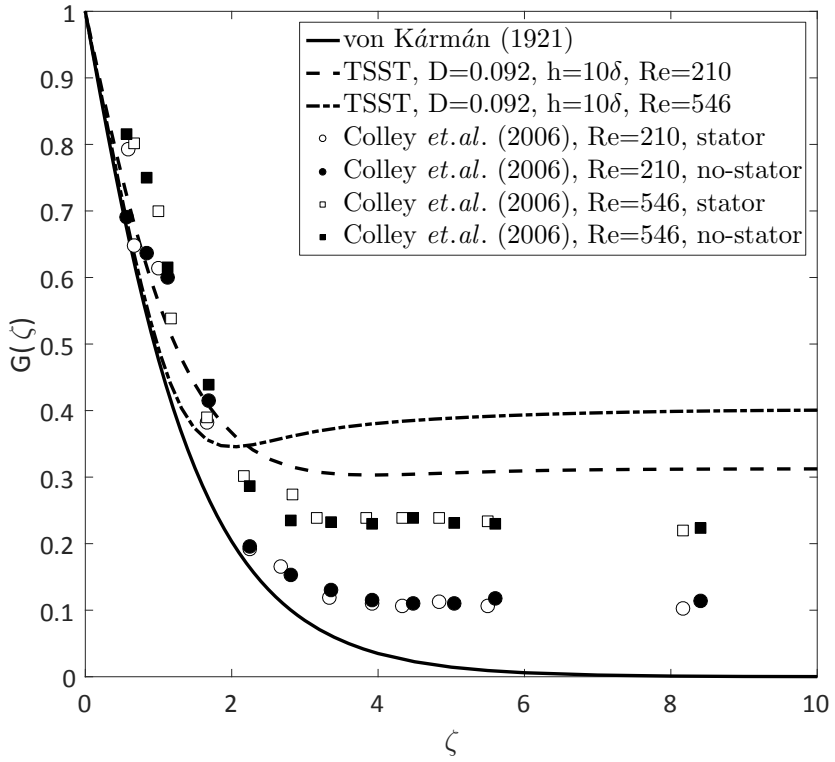

(b) Azimuthal velocity G

Figure 4.4: Comparison of the results of the TSST simulations ($D = 0.092$, $h^* = 10\delta$, $Re_\phi = 733$, $Re = 210$ and $Re = 546$) to the experimental data from Figure 2 in Colley et al. (2006) and von Kármán (1921) similarity solution.

with a radial location in the turbulent region - i.e. above the critical value near $Re = 507$ (Lingwood, 1997). Note here that the von Kármán flow is independent of Reynolds number because it describes the similarity solution denoted in non–dimensional form which is globally valid throughout the laminar flow region of the rotating–disk boundary layer.

As regards the validation of the TSST simulations, apart from the radial flow components of Colley et al. (2006) at $Re = 546$ in Figures 4.4(a) and 4.5(b), in general there is a good qualitative agreement between the TSST results, the von Kármán flow and the experimental data of Colley et al. (2006). It is not appropriate to make a final quantitative comparison between the data of Colley et al. (2006) and the TSST simulations and the von Kármán flow. One of the reasons for this is, for instance, there exists an annular gap between the rotating disk and the stationary lid in the experiments of Colley et al. (2006) which may alter the flow field in comparison to that in TSST simulations. Additionally, in the experiments, the hot–film probe is liable to an effect known as the yaw–angle bias (Bruun, 1995, p. 71). This results from along–wire cooling in the flow field with its three velocity components and leads to overestimates of the measured velocity values. Although the data of Colley et al. (1999, 2006) were not corrected for the yaw–angle bias, as is discussed in Colley et al. (1999, p. 334), since this was not necessary in the particular context of their studies, this issue will be addressed in our experimental study in Section 6.2. Finally, the experiments in the tank of the facility of Colley et al. (1999, 2006) represents a spatially restricted and, therefore, fairly high–noise environment in which one has to resolve small quantities. To appreciate this note that a distance of $\Delta\zeta = 1$ on the abscissa in Figures 4.4 and 4.5 corresponds to a vertical height difference of only $\Delta z^* = 0.36$ mm for their experimental data. Similarly, velocity changes of $\Delta F = \Delta G = 0.1$, at $Re = 210$, correspond to $\Delta u^* = \Delta v^* \approx 0.06$ m s^{-1} occurring over an interval of only $\Delta\zeta \approx 2$, that is 0.72 mm.

The most positive agreement is expected between the TSST simulations

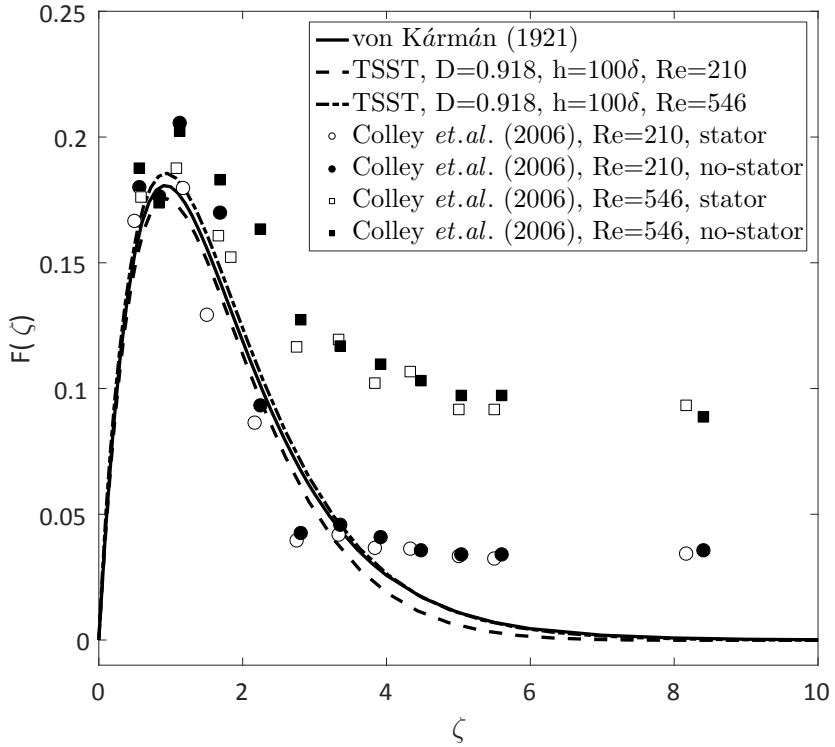

(a) Radial velocity F

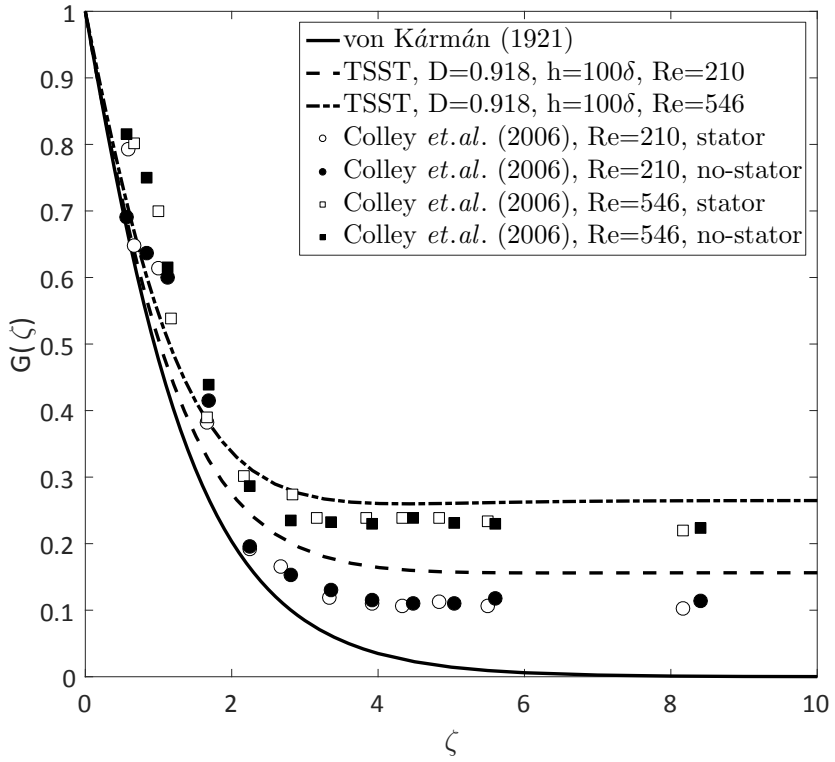

(b) Azimuthal velocity G

Figure 4.5: Comparison of the results of the TSST simulations ($D = 0.918$, $h^* = 100\delta$, $Re_\phi = 733$, $Re = 210$ and $Re = 546$) to the experimental data from Figure 2 in Colley et al. (2006) and von Kármán (1921) similarity solution.

and the von Kármán flow for lowest Reynolds numbers Re and largest aspect ratios D. Figures 4.5(a) and 4.5(b) show that this expectation is actually correct where the aspect ratio is $h^* = 100\delta$, $D = 0.918$. This is the largest aspect ratio in our simulations. One can see in Figure 4.5(a) that there is a good quantitative agreement between the TSST simulations and Kármán (1921) for the radial velocity component for all heights ζ and for the azimuthal flow component in Figure 4.5(b) up to about $\zeta = 2$. Despite the fact that for $\zeta > 2$ the azimuthal flow of TSST simulations deviates more strongly from von Kármán (1921), it is in very good quantitative agreement with the corresponding experimental data by Colley et al. (2006) which display the same type of divergence with respect to von Kármán (1921). This type of discrepancy is naturally expected since our simulations and the data of Colley et al. (2006) are for rotor–stator flow whereas the theory by von Kármán (1921) is for a freely spinning disk. Moreover note that in Figure 4.5(b) the TSST simulations almost exactly quantitatively reflect the dependence on the Reynolds number that was experimentally observed by Colley et al. (2006).

In addition to the validation of the TSST simulations, the data in Figures 4.4(a) and 4.4(b), and in Figures 4.5(a) and 4.5(b), provide a first assessment of the influences of the aspect ratio D on our TSST simulations but this will be addressed in more detail in Section 4.4.1.

In addition to the validation of the TSST simulations, the above comparison of the current results to the experimental data of Colley et al. (2006) produces the first direct, quantitative support to the speculation expressed in their paper that their data do not approach the similarity solution by von Kármán (1921) for $\zeta \to \infty$ due to residual fluid motion exterior to the boundary layer (see Section 2.2). In this context, two additional brief remarks relating to the comparison of the TSST approach and the experimental data of Colley et al. (2006) are provided.

Firstly, in their experiments, even without the stationary lid (*no–stator*

configuration), the height of the water above their rotating disk was only approximately 0.15 m which corresponds to about $h^* = 76\delta$ or $D = 0.75$. Therefore, it is possible that the effects induced due to the existence of the free surface of the water resembled, to some extent, those induced due to the stationary lid (*stator* configuration). This may have possibly contributed to the similarity of the experimental data for their *stator* and *no-stator* case which was also mentioned previously in Section 2.2. Together with the limited size of the water tank (diameter approx. 1 m) housing the disk (diameter approx. 0.5 m) it may also explain why there exists a residual radial flow motion in Figures 4.4(a) and 4.5(a). This is supported by the residual radial flow in Figures 4.4(a) and 4.5(a) being more pronounced for the higher local Reynolds number, $Re = 546$, which corresponds to a position of the hot-film probe closer to the lateral boundary of the water tank and where one would expect stronger effects of any side–wall induced recirculation flow regions that can result in radial flow.

Secondly, the small quantitative discrepancies between experiment and TSST simulation at $\zeta > 4$ in Figure 4.5(a), for the parameter configurations that most closely resembles the case of Colley et al. (2006), i.e. $h^* = 100\delta$ or $D = 0.918$ and at $Re = 210$, are possibly partly associated with the, previously addressed, yaw–angle bias.

4.2.3 Validation: Concluding Remarks

In conclusion, the preceding examination of the current numerical results obtained by the TSST approach has demonstrated that this numerical modelling is suitable to investigate the flow inside the rotor–stator configuration, particularly, the boundary layer flow over the rotor disk. Therefore, this provides enough reliability of the TSST method to investigate qualitative effects, together with their quantitative magnitude, induced by changes in the boundary conditions associated with the rotor–stator configuration. Therewith one can be confident

that it is possible to evaluate these effects in comparison to the boundary–layer flow over a freely spinning disk on the basis of the theoretical similarity solution by von Kármán (1921).

The main issues of the current numerical study are now addressed in the following sections. Further additional validation of the TSST approach will appear in Section 4.3 where the velocity profiles acquired from the TSST simulations are compared with our current experimental data and in Section 4.5 where the roughness effects predicted on the basis of these computations are compared with the corresponding theoretical results of Cooper et al. (2015), Garrett et al. (2016) and Alveroglu et al. (2016).

4.3 Comparison of TSST Results with the Current Experimental Data

Figure 4.6 shows the Reynolds number dependence of the radial and azimuthal flow profiles obtained from the current TSST simulations together with the ones acquired from our experiments. Our experimental data appears here the first time without any introductory information, however, the details of our experimental set–up and the data acquisition process will be addressed in Chapters 5 and 6.

The aspect ratio of the numerical results shown here is $D = 0.918$ which corresponds to $h^* = 100\delta$. This case was chosen to compare the numerical profiles directly with our experiments which were conducted without any stator above the rotating disk where the depth of water is about $h^* = 76\delta$, i.e. this is exactly the same as the *no–stator* case of Colley et al. (2006). There is a very good qualitative and quantitative agreement between the numerical results and the experimental data in Figure 4.6(b). Both our simulations and experiments clearly show the core rotation of water with their order of approximately same magnitudes and

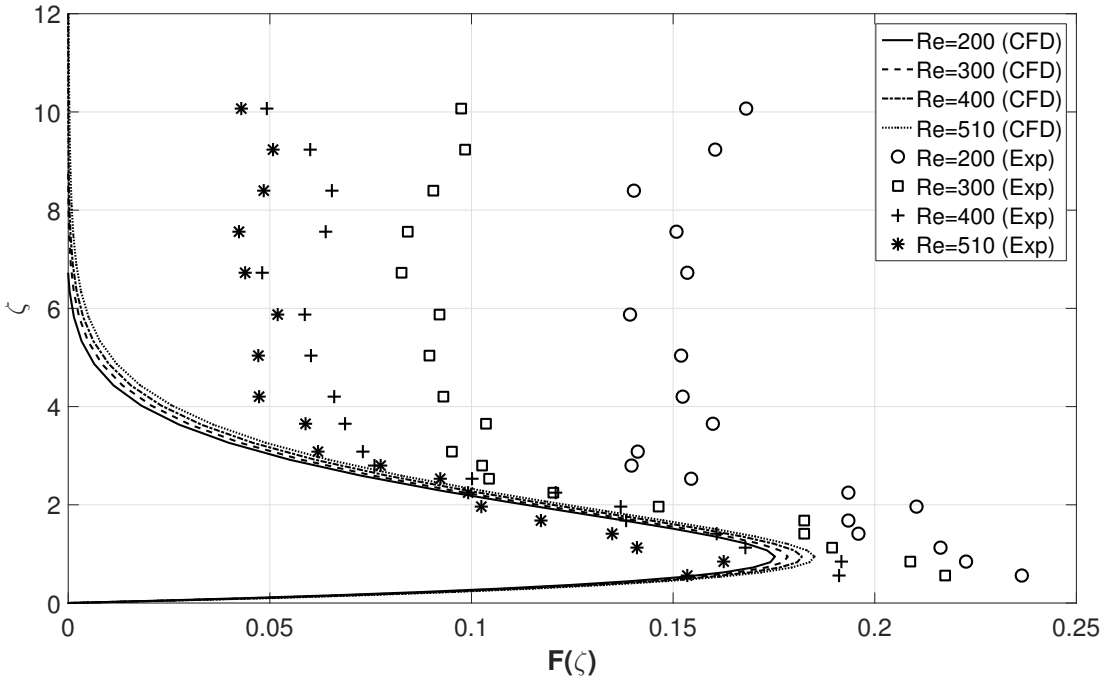

(a) Radial velocity F

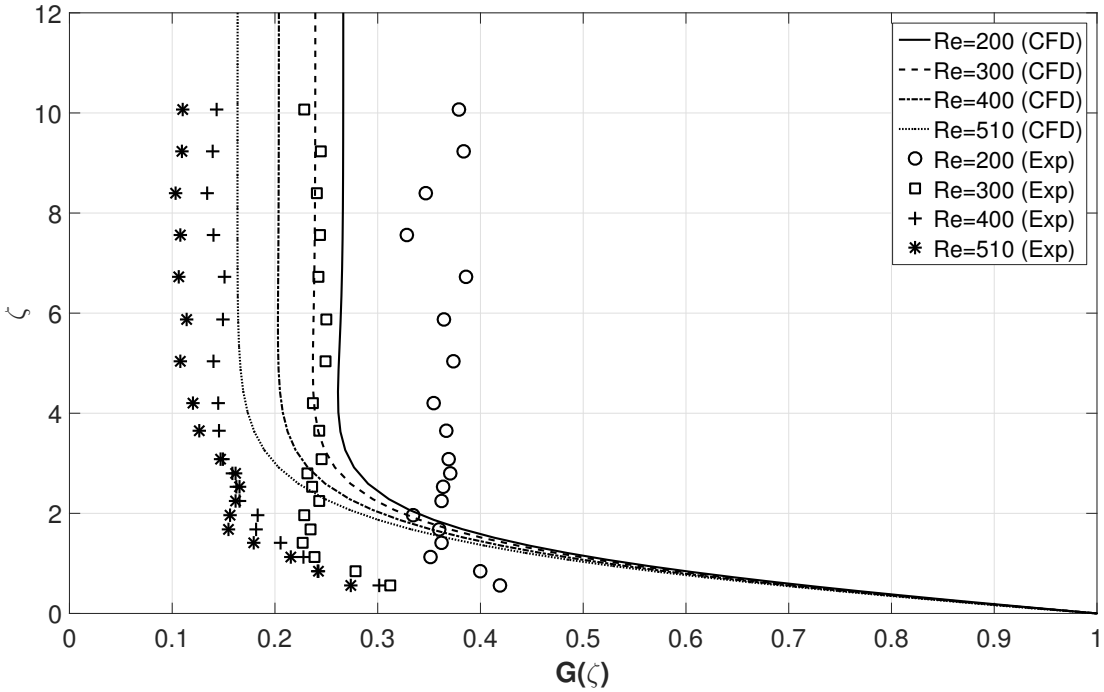

(b) Azimuthal velocity G

Figure 4.6: The Reynolds number dependence of the velocity profiles obtained from the current TSST simulations ($h^* = 100\delta$, $Re_\phi = 600$) and experiments ($h^* = 76\delta$, $Re_\phi = 560$).

also it seems that the Reynolds number affects the azimuthal flow profiles in the same way in both simulations and experiments, i.e. when the Reynolds number is increased the magnitude of the core rotation of water is decreased. This is probably due to the strong vortex appear in the vicinity of the rotation axis of the rotating disk in experiments (*c.f.* Figure 6.10) and the rotor–stator system in simulations.

The Reynolds number dependence of the radial flow component is shown in Figure 4.6(a) where this dependence in simulations is not as strong as the one observed in experiments. It should be noticed that the experimental measurements of the radial flow component are not simple because the velocity magnitudes are very small and thus any effects induced from the small changes in the flow characteristics, such as the Reynolds number, may be hard to be distinguished. Nevertheless, it can still be appreciated that the maximum values of the radial jet flow, at the height of approximately $\zeta = 0.1$, are almost same for both of our simulations and experiments.

4.4 Results from TSST Simulations: Geometry Effects vs. Roughness Effects

In this section of the thesis, the effects of both the finite–size of the flow configuration, i.e. the aspect ratio of the rotor–stator system, and the surface roughness on the boundary–layer flow over a rotating disk are investigated. The underlying rationale is to establish whether the effects in both cases are of similar nature and, if so, whether they must be expected to be of comparable magnitude in the type of system considered here.

4.4.1 Geometry Effects

Figures 4.7(a) and 4.7(b) display results from TSST simulations demonstrating how the aspect ratio D of the rotor–stator configuration influences the radial and azimuthal components of the flow velocity inside the boundary layer on the rotor for a global rotational Reynolds number of $Re_\phi = 600$ and at a radial position corresponding to a local rotational Reynolds number of $Re = 500$ (laminar flow regime), where $R^* = 0.6$ m and $\Omega^* = 1$ rad/s. Figures 4.7(a) and 4.7(b) illustrate the computational data obtained from the TSST simulations in comparison with the corresponding theoretical laminar velocity profiles of von Kármán (1921) for an unbounded rotating disk. The TSST simulations were conducted for the aspect ratios D of $0.046, 0.092, 0.367, 0.918$. These values for D correspond to gap widths h^* of $5\delta, 10\delta, 40\delta, 100\delta$ when expressed in terms of the boundary layer thickness for the flow over a rotating disk satisfying the theory of von Kármán (1921).

Figures 4.7(a) and 4.7(b) reveals that, as one would expect, the velocity profiles obtained from the TSST simulations approximate the von Kármán's flow when the aspect ratio D is increased. However, the azimuthal profile, for instance, is still significantly changed from the similarity solution of Kármán (1921) even for the largest aspect ratio ($D = 0.918$, $h^* = 100\delta$) in our simulations. This is the case at least for all heights above approximately $\zeta = 1$ – and remembering that the boundary layer extends to $\zeta = 5.5$ according to von Kármán (1921). At heights above approximately $\zeta = 2$ the difference for the azimuthal flow component is still of the order of $\Delta G \approx 0.15 - 0.25$, reflecting the core rotation in rotor–stator flow.

Figure 4.7(a) shows that a decrease in the aspect ratio results in a reduction in the radial jet flow, particularly in the region of approximately $0 \leq \zeta \leq 2$. This reduction is of the order of about $\Delta F \approx 0.02$ which corresponds to approximately 10% in comparison to the maximum value of the radial jet flow $F \approx 0.18$.

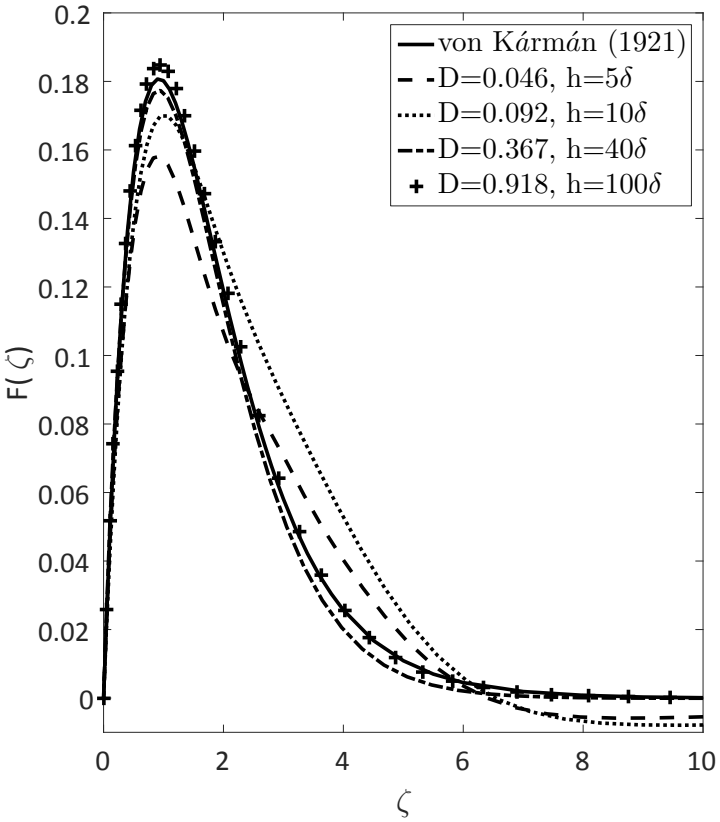

(a) Radial velocity F

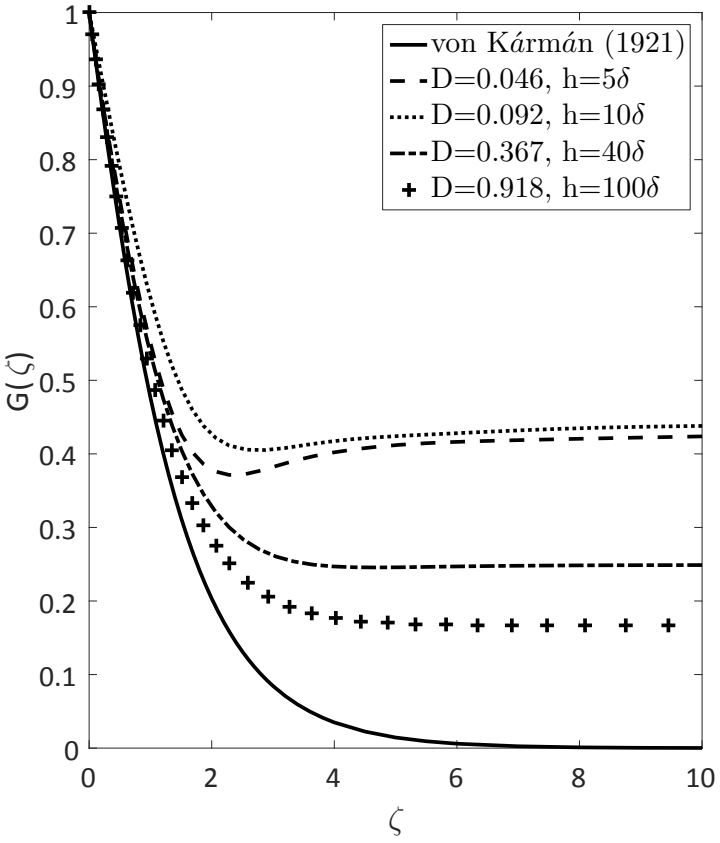

(b) Azimuthal velocity G

Figure 4.7: The effect of the aspect ratio D on the basic flow profiles ($Re_\phi = 600$, $Re = 500$).

A similar reduction effect is also observed as a result of an increase in the surface roughness height which will be considered in the subsequent section. The discrepancies between the rotor–stator flow configuration, when the gap width is 100δ, and the von Kármán flow are less significant for the radial velocity component than the azimuthal flow component but, nevertheless, within the region of approximately $3 \leq \zeta \leq 6$, one can still recognize differences of up to the order of around $\Delta F \approx 0.003$ which corresponds to about 2% in comparison to the maximum value of $F \approx 0.18$.

4.4.2 Roughness Effects

The effects of the distributed surface roughness, predicted by the TSST simulations, on the flow profiles of the boundary layer on the rotor in a rotor–stator flow configuration are shown in Figure 4.8(a) for the radial and in Figure 4.8(b) for the azimuthal components. The rotor–stator configuration investigated in the simulations has the aspect ratio of $D = 0.092$ which corresponds to $h^* = 10\delta$. The global rotational Reynolds number is $Re_\phi = 600$ and the data were collected at a radial location which corresponds to a local rotational Reynolds number of $Re = 500$. The TSST simulations were conducted for the geometric roughness heights of $K = 100, 300$ and 500μm. These specific values for the roughness were selected because they describe approximately the range of typical real roughness heights one would expect to find associated with applications involving drag–reduction techniques in practice. The velocity profiles acquired for these roughness parameters are compared with the smooth surface case which was obtained again by the TSST simulations.

The investigation of the roughness–induced effects shown in Figure 4.8 reveals that they are qualitatively akin to the geometry–induced effects in Figure 4.7 – but a direct comparison to evaluate quantitative difference will be shown in Figure 4.9 in Section 4.4.3. The data in Figure 4.8(a) show that roughness de-

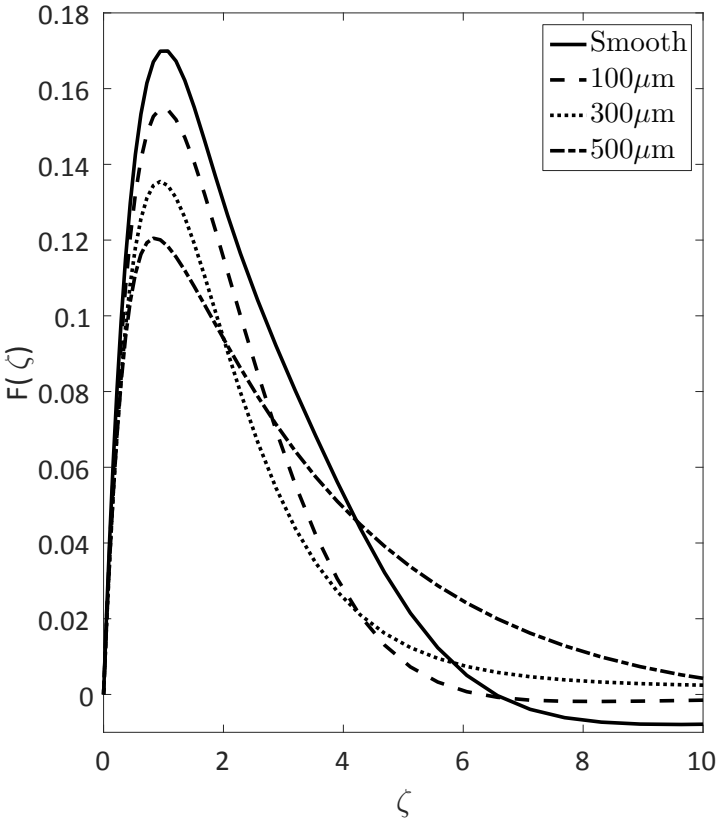

(a) Radial velocity F

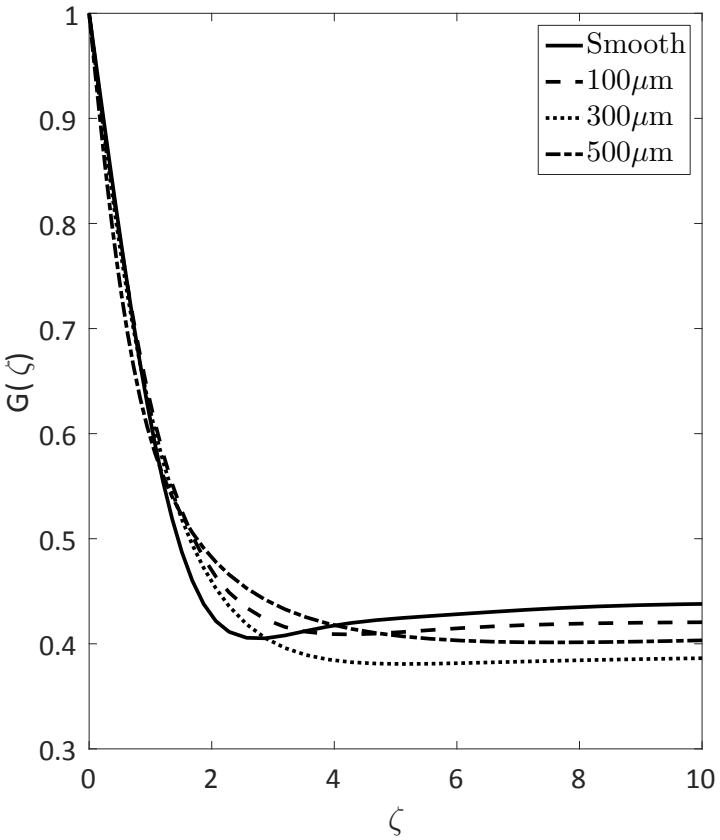

(b) Azimuthal velocity G

Figure 4.8: The effect of isotropic roughness on the basic flow profiles ($D = 0.092$, $h^* = 10\delta$, $Re_\phi = 600$, $Re = 500$).

creases the radial jet flow, in comparison to the curve for the smooth disk, within, approximately, $0 \leq \zeta \leq 5$, whereas this trend is reversed for heights above this region.

The magnitude of typical variation of the predictions for different roughness heights are of the order of around $0.02 \leq \Delta F \leq 0.04$ and this of comparable magnitude to the values $\Delta F \approx 0.02$ obtained for the geometry–induced effects in Figure 4.7(a).

Similar roughness–induced modifications are observed for the azimuthal flow component in Figure 4.8(b) where typical values are of the order of around $\Delta G \approx 0.1$ for heights $\zeta > 0.15$; which compares to $0.15 \leq \Delta G \leq 0.25$ for the geometry–induced effects at $\zeta > 2$ in Figure 4.7(b). Figure 4.8(b), additionally, reveals that roughness seems to reduce the magnitude of the rotational velocity of the core rotation of water. Despite the fact that this effect is not directly in line with an increase in roughness height, it is of comparable magnitude to the geometry–induced effects.

Therefore, the comparison of Figures 4.8 and 4.7 suggests that it can be difficult to distinguish between roughness–induced and geometry–induced effects in experiments. Specifically, and in a general experimental context, the comparison of Figures 4.8 and 4.7 describes the necessary measurement sensitivity for methods attempting to recognize the difference between geometry-induced and roughness–induced effects in a geometrically restricted flow environment. Any measurement technology to be adopted must be sufficiently sensitive to resolve velocity changes significantly smaller then the magnitude of the alterations anticipated due to the roughness effects and the geometry effects individually.

4.4.3 Comparison of Roughness–Induced Effects and Geometry–Induced Effects

The roughness–induced and the geometry–induced effects, obtained by the TSST approach, are compared here in Figure 4.9. The plot shows results for two aspect ratios $D = 0.046$ and $D = 0.092$ which correspond to $h^* = 5\delta$ and $h^* = 10\delta$ respectively, in comparison to the results for the roughness–induced effects for the largest aspect ratio investigated, $D = 0.092$, $h^* = 10\delta$, with the geometric roughness heights of 100 μm and 300 μm on the rotor disk. The figure highlights qualitatively that the predicted roughness–induced effects and the geometry–induced effects on the radial and the azimuthal component of the flow velocity within the boundary layer are very similar in both nature and magnitude.

4.4.4 Conclusions Based on Comparison of Geometry vs. Roughness Effects from TSST Simulations

The comparison of geometry–induced effects and roughness–induced effects in Figures 4.7, 4.8 and 4.9 reveals that it can be difficult to distinguish between both in a water–based rotor–stator–like rotating–disk configuration with typical, practical dimensions similar to those of the facility used in Colley et al. (1999), Colley et al. (2006) and Harris (2013). As a result, the computational data based on the TSST simulations indicate that it might be difficult to use the data from the rotor of such a rotor–stator–like rotating–disk facility to confirm many of the computational predictions for roughness effects induced into the boundary–layer flow for an unrestricted disk spinning in an infinite liquid medium. For this purpose, it ideally requires a rotating disk housed within a substantially larger water tank where it can spin freely without the requirement for the stator shroud shown in Figure 2.5 to eliminate free–surface, wave– and wall–induced disturbances affecting the boundary–layer flow on the surface of the rotating disk. Alternatively, an air–based experimental facility can be used since it was shown

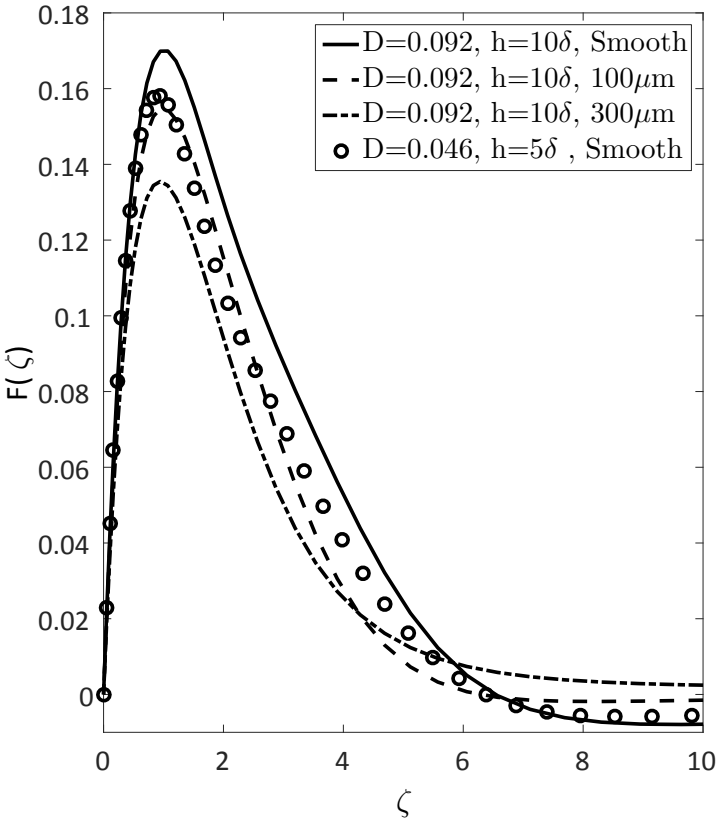

(a) Radial velocity F

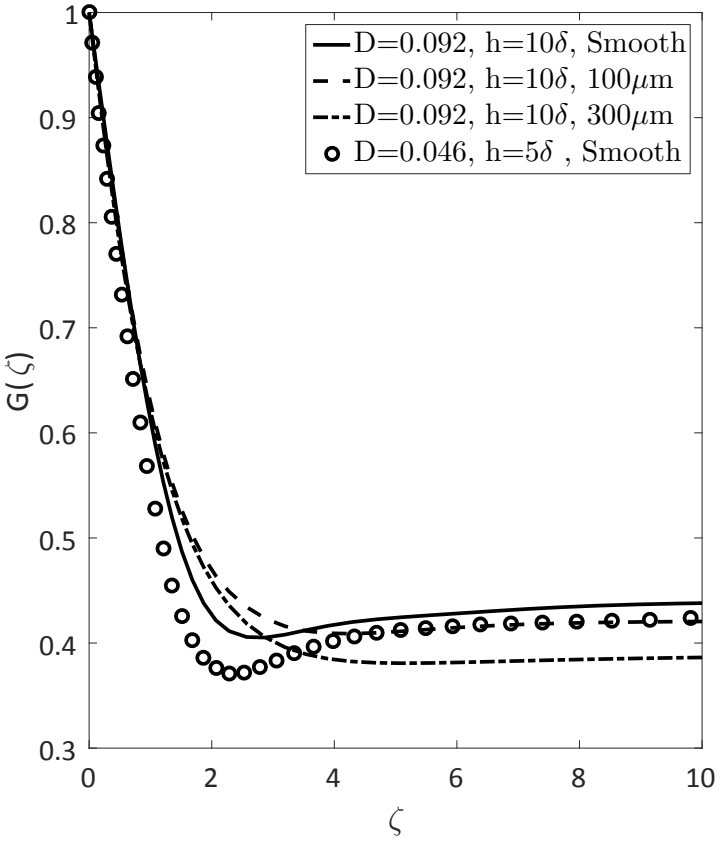

(b) Azimuthal velocity G

Figure 4.9: Comparison between the effects of the aspect ratio D and the geometric roughness heights K ($Re_\phi = 600$, $Re = 500$).

previously in Section 2.2 that the core rotation of the fluid outside the boundary layer does not exist in those types of facilities, whereas this core rotation seems to be unavoidable even for significantly large domains in water–based configurations.

4.5 Comparison of Roughness Effects obtained from TSST Simulations with Cooper et al. (2015), Garrett et al. (2016) and Alveroglu et al. (2016)

The roughness–induced effects calculated by the TSST approach are now compared to the corresponding predictions obtained on the basis of the methods described in detail in Cooper et al. (2015) and in Garrett et al. (2016). The aim of this comparison is twofold. Firstly, it will produce a further means of validation for our TSST simulations. Secondly, a favourable comparison between all three fundamentally different numerical approaches will, in turn, provide further contribution to some of the main conclusions drawn in Cooper et al. (2015) and Garrett et al. (2016). Note here that the TSST simulations in Sections 4.5.1, 4.5.2 and 4.5.3 were acquired for a rotor–stator configuration of constant gap width $D = 0.092$, which corresponds to $h^* = 10\delta$, such that changes of the computational data truly reflect roughness–induced effects only.

The global rotational Reynolds number for the TSST simulations is $Re_\phi = 600$ and the results are for a radial position corresponding to a local Reynolds number $Re = 500$. However, the results of Cooper et al. (2015), Garrett et al. (2016) and Alveroglu et al. (2016) are independent of the Reynolds number because in these studies the steady–state flow profiles represent modified versions of the similarity solution of von Kármán (1921) for the Navier–Stokes equations which describes the flow at all values of the Reynolds number Re.

4.5.1 TSST Results vs. Cooper et al. (2015)

Figure 4.10 compares the TSST simulations for roughness–induced effects to corresponding data we obtained on the basis of the method, and the code, of Cooper et al. (2015). The definition of the surface roughness in that paper is based on the method of Miklavčič and Wang (2004). The distributed surface roughness on a rotating disk is modelled by means of substituting the usual no–slip boundary condition with a *partial slip* condition on the surface of the rotating disk. This *partial slip* condition is obtained by means of introducing two slip coefficients relating the radial and azimuthal velocity components with the radial and azimuthal shear stresses, respectively. The slip coefficient for the radial component is referred to as λ and that for the azimuthal component is η in Cooper et al. (2015). The partial slip reduces to the usual no–slip boundary condition for $\lambda \to 0$ and $\eta \to 0$, whereas the hypothetical condition of complete slip is approached for $\lambda \to \infty$ and $\eta \to \infty$. Therefore, an increase in λ and/or η corresponds to an increase in the roughness height in the radial and/or azimuthal direction, respectively. Note here that $\lambda \neq \eta$ can be chosen which means that any type of surface roughness, such as isotropic roughness, can be modelled with this approach, refer to Cooper et al. (2015) for further details. Based on the *partial slip* condition, they then establish the modified steady–flow velocity field according to the similarity solution of the Navier–Stokes equations due to von Kármán (1921).

Here, the values of $\eta = 0, 0.14, 0.57$ and 1.18 were chosen where the radial shear stress is kept constant at $\lambda = 0$. This choice of λ enables a direct inter–comparison between our TSST results and the numerical data of *both* previous publications, Cooper et al. (2015) and Garrett et al. (2016). As discussed in Garrett et al. (2016), the choice for $\lambda = 0$ was enforced in that study to enable a comparison with Cooper et al. (2015) due to certain limitations of the alternative approach of modelling roughness to be addressed in Section 4.5.2.

A comparison of the results in Figure 4.10(a) obtained by means of the

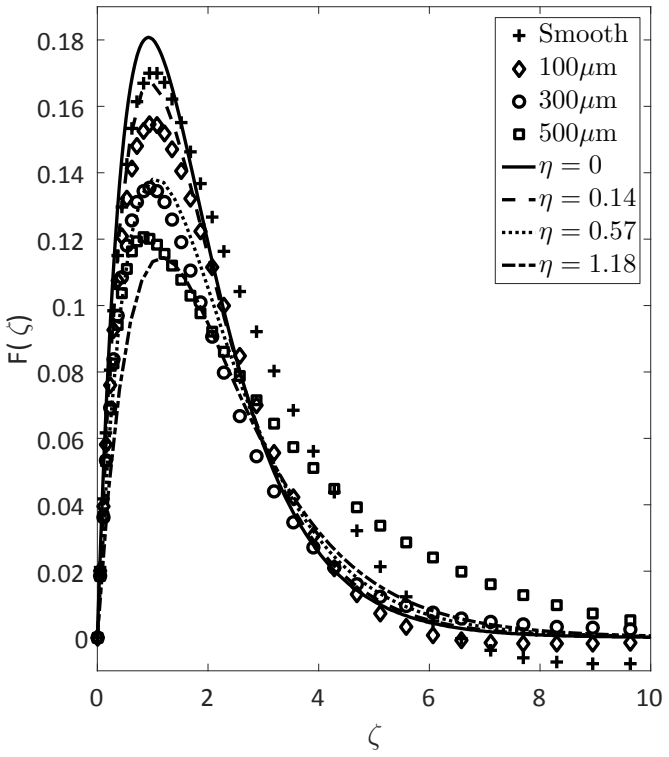

(a) Radial velocity F

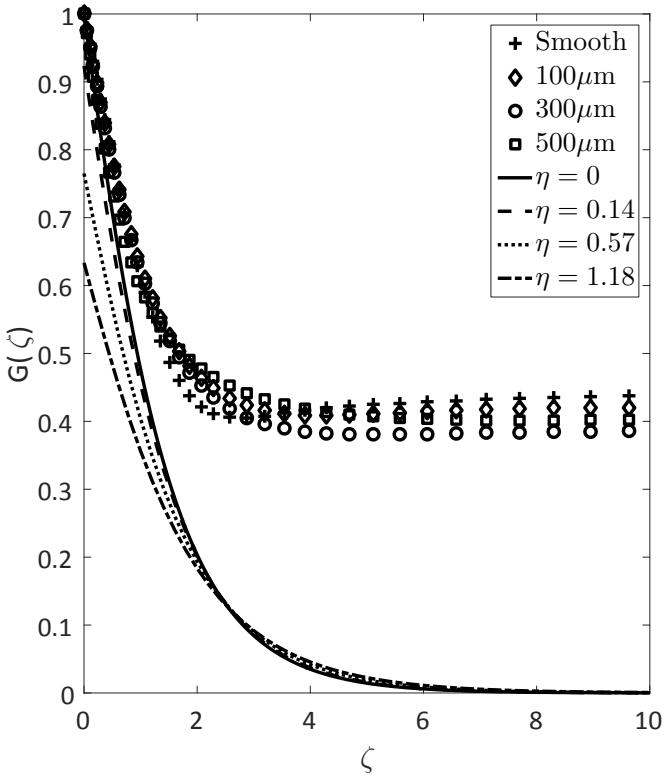

(b) Azimuthal velocity G

Figure 4.10: Comparison between the roughness effects predicted by the TSST simulations ($Re_\phi = 600$, $Re = 500$) and the roughness effects as predicted by using the code of Cooper et al. (2015) ($\lambda = 0$) based on their *partial slip* approach. Markers identify current TSST data and lines represent data of Cooper et al. (2015).

TSST simulations for the geometric roughness heights K of $0, 100, 300$ and 500μm and with the *partial slip* approach for the different values of η, reveals a very high level of qualitative agreement for the radial velocity component. In this context, it is worth highlighting again that it is the instability mode arising from the inflection point (Schlichting and Gersten, 2004, p. 432) on the radial velocity component (*cf.* Figure 2.1) that is mainly responsible for the laminar–turbulent transition of boundary layers with a cross–flow component. Hence, this high level of agreement between the results of the current TSST approach and Cooper et al. (2015) represents substantial supportive evidence regarding validity of the boundary–layer transition issues discussed in that paper.

A comparison of our TSST simulations with the data of Cooper et al. (2015), however, is not that simple for the azimuthal flow component that is shown in Figure 4.10(b). Due to the fact that flow profiles affected by the roughness in Cooper et al. (2015) are the modified versions of von Kármán flow, there is no core rotation of the fluid outside the boundary layer of the rotating disk. However, in our TSST simulations, this rotary flow motion exists as a result of the finite size of the rotor–stator configuration. Therefore, the numerical data from our TSST approach differ quite significantly from those in Cooper et al. (2015). Nevertheless, what the data in Figure 4.10(b) do show is that for the TSST simulations and also for the simulations following Cooper et al. (2015), roughness effects are of comparable magnitude.

Although the *partial–slip* condition is a standard approach in modelling flow over rough surfaces, the slip coefficients λ and η do not, a priori, bear any direct relevance to real geometric roughness. They only become useful if, for any particular application, empirical data are available that suggest how their values should be selected. As a result of the high level of agreement that the TSST simulations displayed in comparison to experimental and computational data in all preceding sections, and due to the qualitative agreement in the present, and in the following sections, it appears that it may be possible to employ TSST

simulations to determine theory–based calibration charts relating λ and η to different values of geometric roughness. However, only future experiments will be able to reveal if this is indeed possible in practice.

4.5.2 TSST Results vs. Garrett et al. (2016)

The TSST results from the preceding section for the roughness–induced effects and the theoretical data acquired on the basis of the method described in detail in Garrett et al. (2016) are compared in Figure 4.11. Garrett et al. (2016) used an alternative method of modelling roughness which is based on the theoretical technique of Yoon et al. (2007). Their model defines the roughness by introducing a specific surface distribution as a function of the radial position and assumes a rotational symmetry. The numerical data of Garrett et al. (2016) are displayed in terms of the parameter a which is the ratio of the amplitude A to the wavelength B of the sinusoidal surface function. The method of Yoon et al. (2007) is, therefore, limited because it models the roughness in the radial direction only, whereas the more flexible technique based on Miklavčič and Wang (2004) in Cooper et al. (2015) enables the roughness to be modelled in the radial and the azimuthal directions by means of selecting the slip coefficients λ and η differently. This restriction of the method by Yoon et al. (2007) is the cause why the value $\lambda = 0$ had to be chosen in Section 4.5.1. The data in Figures 4.11(a) and 4.11(b) do not need an additional detailed explanation because they exactly mirror the observations discussed in connection with Figures 4.10(a) and 4.10(b) in the previous section. It is, nonetheless, highlighted again that it is not acceptable to perform quantitative comparisons between the results obtained from the different simulation approaches as a result of the discussed specific differences, and limitations, associated with the techniques in Cooper et al. (2015) and Garrett et al. (2016). The significant outcome is that all methods result in consistent qualitative changes of the relevant quantities which are of similar magnitude.

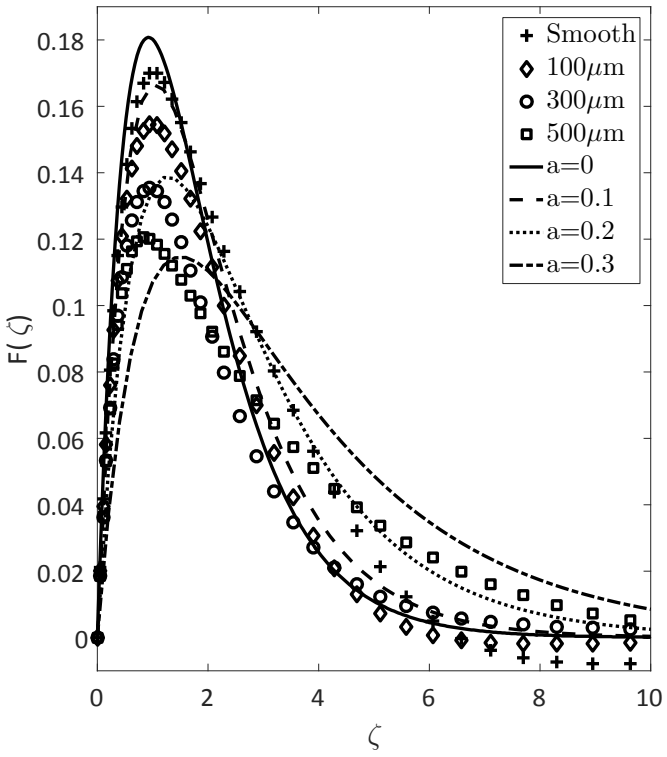

(a) Radial velocity F

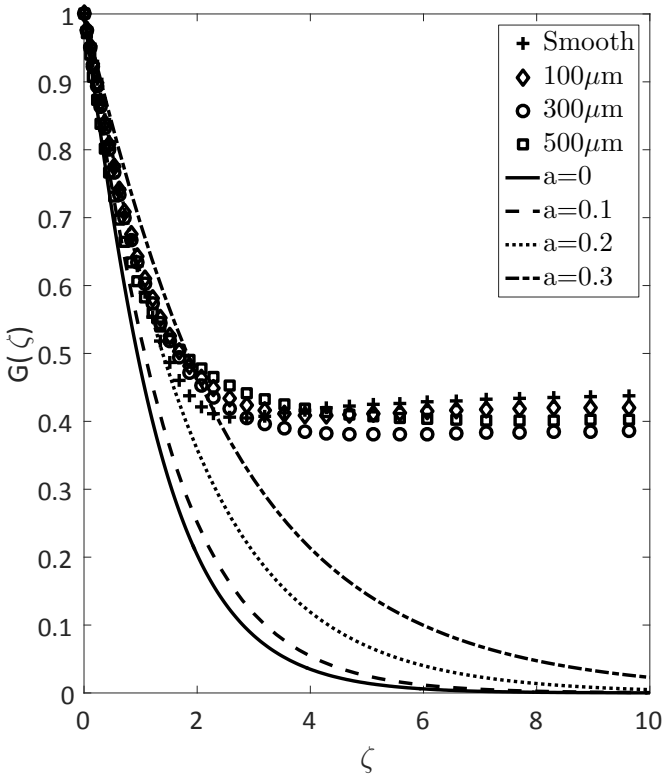

(b) Azimuthal velocity G

Figure 4.11: Comparison between the roughness effects predicted by the TSST simulations ($Re_\phi = 600$, $Re = 500$) and the roughness effects predicted in Garrett et al. (2016) based on the approach of modelling roughness by prescribing a surface distribution as a function of the radial position. Markers identify current TSST data and lines represent data of Garrett et al. (2016).

4.5.3 TSST Results vs. Alveroglu et al. (2016)

The steady–state mean flow profiles modified due to the roughness–induced effects and obtained from our TSST simulations, which were illustrated previously in Sections 4.5.1 and 4.5.2, have been subjected to linear stability analyses by means of the same numerical code used in Cooper et al. (2015) and in Garrett et al. (2016). These analyses are beneficial since the effect of the surface roughness on the stability of the boundary–layer flow is one of the main goals of this current research.

The two previous theoretical studies by Cooper et al. (2015) and Garrett et al. (2016) addressed the stability analyses and provided the neutral stability curves associated with the mean flow profiles modified due to the effects of the surface roughness. As mentioned previously, their flow profiles are the modified versions of the von Kármán flow, however, our simulations are for the rotor–stator flow configuration which substantially differs from this flow type and thus a direct comparison of our neutral stability curves with these two studies may not be appropriate. Nevertheless, there is a recent study by Alveroglu et al. (2016) which considers the effect of surface roughness on the boundary layer stability for the BEK family flows. Note here that the rotor–stator configuration and correspondingly the water–based rotating disk facility represent the intermediate states of BEK family flows, see Section 2.4 as a reminder. In addition to Alveroglu et al. (2016), Jasmine and Gaijar (2005) also investigated the BEK family of flows using linear stability theory. However, only the effect of the gap between the rotating disk and the stationary lid on the stability of the system was examined in that study and the effect of surface roughness was not addressed. They found that with a decrease in distance between the disk and the lid, the BEK family of flows become increasingly stable. In the current study, however, it is only beneficial to compare our neutral stability curves produced based on the mean flow profiles reflecting the roughness–induced effects with those provided in Alveroglu et al.

(2016).

Alveroglu et al. (2016) modelled the surface roughness based on the approach of Miklavčič and Wang (2004) and by applying the same methods as in Cooper et al. (2015). Figure 4.12 compares the neutral stability curves obtained by our TSST simulations with those of Alveroglu et al. (2016). The figure illustrates the usual type of results where the wave–number of the radial disturbance α_r is displayed as a function of the local Reynolds number Re. For any value of Re, any particular disturbance α_r is unstable if it lies within the area enclosed by the curves shown and it is stable if it lies outside the area enclosed. The figure displays the TSST results in comparison with the data of Alveroglu et al. (2016) for von Kármán and Ekman flows over isotropically rough disks. These two flow cases were selected from Alveroglu et al. (2016) for the comparison because the qualitative nature of the flow over the rotor disk in the rotor–stator cavity flow lies somewhat between these two types of flow scenarios as discussed previously in Section 2.4.

The two previously mentioned, see Section 2.6, instability modes are addressed here. The Type–I mode is an inviscid instability mode arising due to the Rayleigh's inflection point criterion and reveals itself in experiments in the form of a series of co–rotating vortices within the laminar–turbulent transition region of the boundary layer over the disk. Additionally, the Type–II mode, which is associated with the streamline curvature and Coriolis effects, is concerned. However, the exact physical nature of the Type–II mode remains, as yet, unknown.

In both Figures 4.12(a) and 4.12(b), there is a qualitative agreement between the results showing a stabilizing effect of roughness on both the inviscid Type–I (cross-flow) and the viscous Type–II instability mode. Stabilization is recognized by a shift of the stability curves towards the positive x–axis, i.e. higher Reynolds number; that is the shift to the right in these figures. It is not feasible to quantitatively compare the TSST results and the data of Alveroglu et al. (2016) as a result of the approach of Miklavčič and Wang (2004) used by Alveroglu et al.

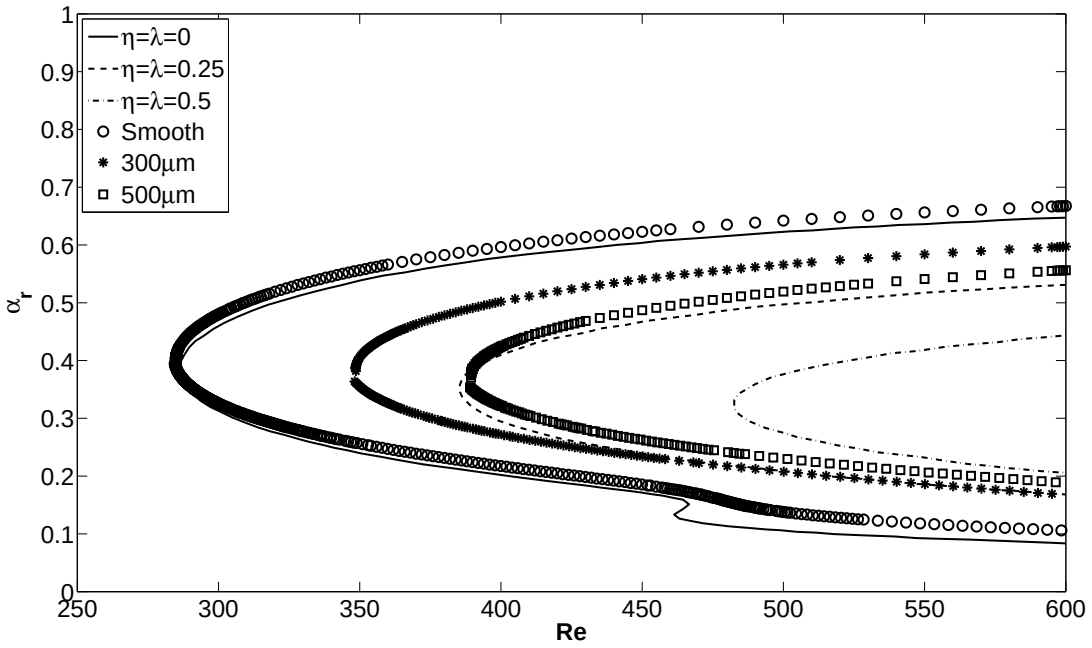

(a) von Kármán flow

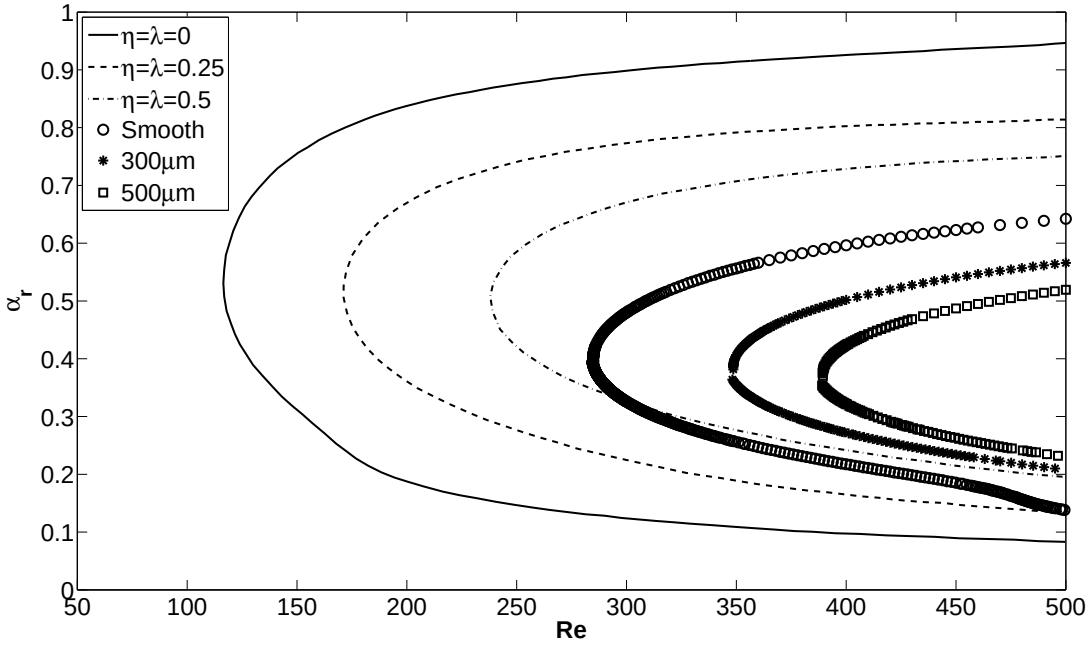

(b) Ekman flow

Figure 4.12: Comparison of neutral curves obtained by the TSST simulations for the rotor–stator flow configuration with the ones presented by Alveroglu et al. (2016) for isotropic roughness. Markers identify results of stability calculations based on current TSST data and lines represent data of Alveroglu et al. (2016).

(2016). The reason for this restriction was previously addressed in Section 4.5.1 while comparing our results with those provided by Cooper et al. (2015).

Note, nevertheless, that for the von Kármán flow over smooth surfaces in Figure 4.12(a), there is a very good quantitative agreement between our neutral stability curve obtained from the TSST simulations and the corresponding curve of Alveroglu et al. (2016). Both of the neutral stability curves are almost in perfect agreement with each other, apart from the absence of the Type–II instability in the current TSST simulation for a single temporal frequency within the narrow region around $460 \leq Re \leq 480$ where $0.13 \leq \alpha_r \leq 0.15$. The Type–II mode is represented by the little kink on the curve for $\eta = \lambda = 0$ in that parameter region. The very good quantitative agreement between these curves found here further reinforces the confidence in the TSST simulations. In fact, the close agreement indicates that it may even become possible to apply TSST simulations to calibrate the slip coefficients, when used in the context of the type of calculations described in Cooper et al. (2015) and Alveroglu et al. (2016), for a subsequent comparisons to experimental data. Main results of this section relate, however, to the stabilizing effect of the surface roughness on the Type–I instability mode.

The absence of Type–II mode, in Figure 4.12(a), for the boundary–layer flow over a smooth rotating disk in a rotor–stator configuration was revealed by means of the current TSST simulations for a single temporal frequency. In addition to this outcome, the data in Figure 4.12(b) shows that this instability mode vanishes also for the results of Alveroglu et al. (2016) for Ekman flow displayed there. This correspondence suggests that the absence of the Type–II mode from the TSST simulations in Figure 4.12(a) reflects the fact that the flow over the rotor disk of the rotor–stator configuration represents an intermediate state between the limits of von Kármán and Ekman flows, refer to Section 2.4 as a reminder. Therefore, it indicates that the absence of the Type–II mode for the TSST simulations may be brought about by the non–vanishing fluid motion in the core of the flow field between the two boundary layers on the rotor and the

stator. However, more detailed further analysis should be carried out to support this argument.

Chapter 5

Experimental Set–up

5.1 Introduction

The effects of distributed surface roughness on the flow profiles and the boundary–layer transition over rotating disks were experimentally investigated. The water–based rotating–disk facility and its preparation are described in Sections 5.2 and 5.3, respectively. The test disks with smooth surface and also the disks with the concentric grooves representing distributed roughness are described in Section 5.4. The calibration techniques and the data acquisition process are explained in Sections 5.5 and 5.6.

5.2 Experimental Facility

The rotating disk facility used in our study was designed and built by Colley (1997) and it is displayed here in Figure 5.1 and also sketched in Figure 5.2. The cylindrical tank with a diameter of 1 m and a height of 650 mm is filled with 500 litres of water and it is the main component of the facility with a rotating support disk placed on top of a drive shaft inside the tank under the water. The rotation axis of the support disk is same with the central vertical axis of the water tank and it holds the actual test disks which are examined in experiments.

There is a 2–axis traverse system that allows the probe holder to be moved horizontally and vertically over the disk surface. The hot–film probe is mounted on the probe support and can be lowered or raised by means of a vertical vernier scale with accuracies of 1 μm. The radial movement of the probe is performed manually by means of a fixed ruler and thus the accuracy in the radial direction is approximately ± 0.5 mm.

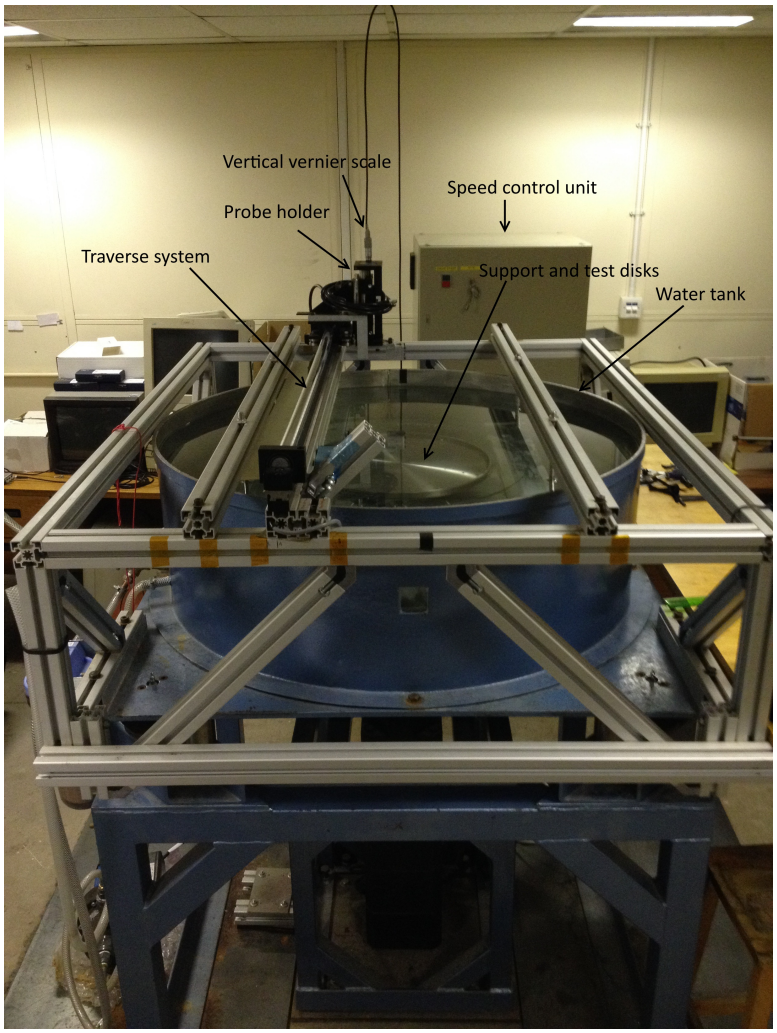

Figure 5.1: Rotating disk facility.

The drive shaft is rotated by a Bosch DC servo motor which is controlled by a speed control unit operated via a separate PC running the Trio Motion software. The water tank is lifted over four air filled dampers to isolate the tank from outside noise. Furthermore, a stationary annular shroud, positioned flush with the rotating disk surface, prevents the flow recirculation disturbing the

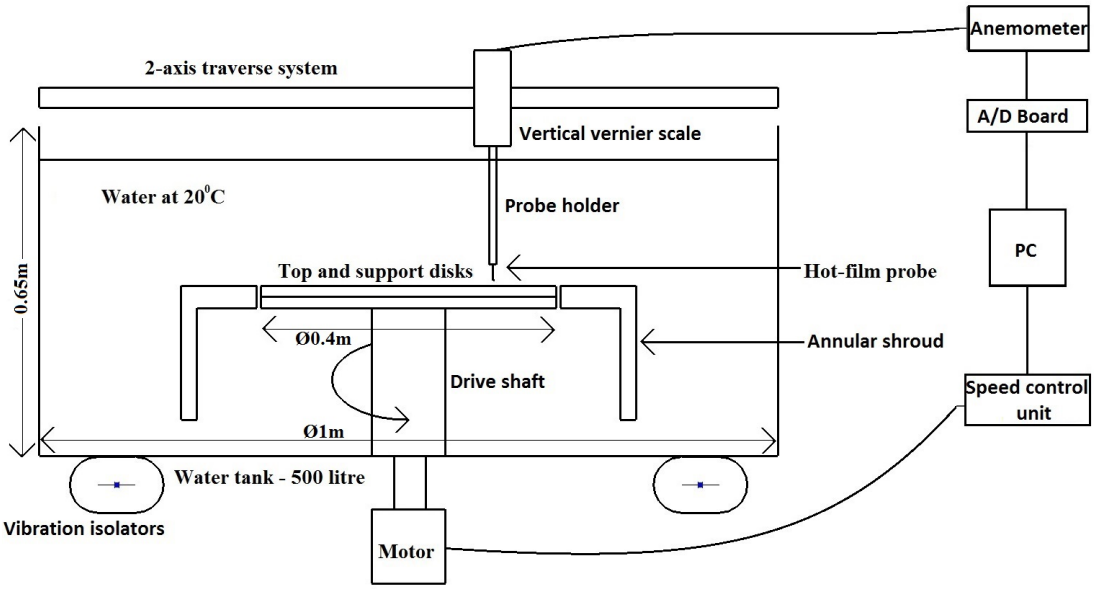

Figure 5.2: The sketch of the experimental facility.

Figure 5.3: TSI 1218–20W hot–film probe.

boundary layer over the disk surface.

A TSI 1218–20W hot–film probe, illustrated in Figure 5.3, is connected to a Dantec MiniCTA 54T42 constant temperature anemometer (CTA), represented in Figure 5.4, which is then linked to a NI 9215 data acquisition card (DAQ). The DAQ card is then connected via a Hi–Speed USB Carrier, NI USB–9162, to a PC running NI LabView software for data analyses. The overheat setting is performed via white dip switches inside the anemometer (*c.f.* Figure 5.4) using the related probe, support, and cable resistances. This anemometry system is a new addition to the previously used experimental rig since the previous anemometer system was very old and caused various serious problems as reported by Harris (2013).

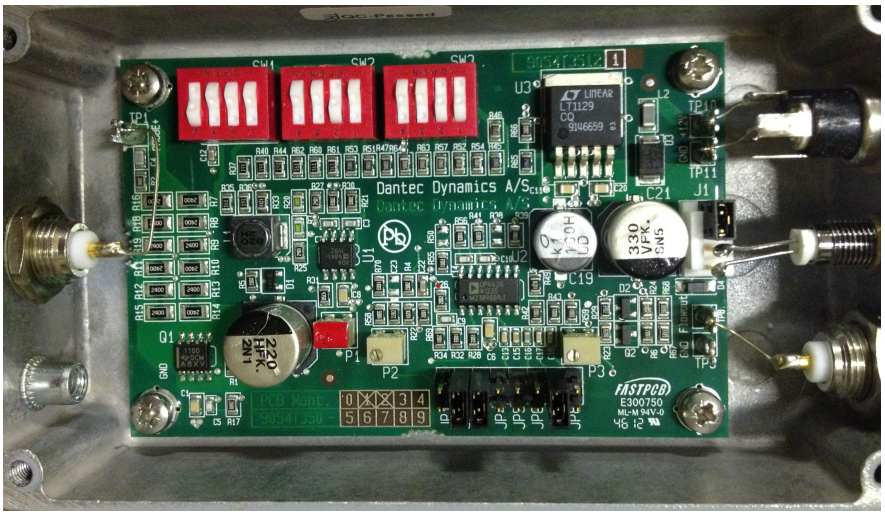

Figure 5.4: Dantec Dynamics MiniCTA 54T42 constant temperature anemometer.

More detailed information about the facility which is not reported here, such as the technical drawings, can be found in Colley (1997). Furthermore, one of the main goals of the current research is to improve the data of Harris (2013), who previously used the same experimental facility, since although his data show a qualitative agreement, it was hard to draw a final conclusion from his experimental measurements. Therefore, improvements, such as the new calibration method and the anemometry system, have been added, in the context of the current study, to that facility used previously by Colley et al. (1999, 2006); Harris (2013); refer to Section 2.2 for the details of these preceding studies.

5.3 Tank Preparation

The tank is filled with mains tap water which is filtered to remove undesirable particles of smaller than 0.1 μm. This resolves the probe contamination problem. The water remains in the tank for two days before performing any experiments to allow any air bubbles to leave the water. This is done because the bubble formation on the probe is one of the main difficulties that makes the hot–film measurements in liquids complicated (Bruun, 1996). This problem was also addressed by Rasmussen (1967) as a common issue observed on a heated

probe immersed in air–saturated water. Moreover, the temperature of the room, where the tank is placed, is kept constant at $20°C$ and the temperature of the water is checked every 30 minutes during the experiments. The tank is lifted by means of four air–filled dampers and hence becomes vibration free and finally ready for the experimental purposes.

5.4 Test Disk Manufacture

There are three types of test disks used in the experiments which are glass disks, disks with concentric grooves distributed over the whole surface, and disks with a single groove on the test surface of disks (hereinafter single–grooved disks). Glass disks having 388 mm diameter and 10 mm thickness were manufactured by an external supplier and the average roughness of their surfaces was measured as 9 μm using a Taylor Hobson's surface profilometer. Test disks having distributed concentric grooves illustrated in Figure 5.5 were previously manufactured in the School of Engineering, University of Warwick for a study by Harris (2013). These disks have 390 mm diameter and 12 mm thickness and were made of aluminium. The top surfaces of these disks were first polished to obtain a smooth surface and then the grooves were cut accordingly as they were designed and are listed in Table 5.1. The surface profiles of these disks are traced using the Taylor Hobson's surface profiler and a sine function is superimposed on this trace for comparison in Figure 5.6. Effective groove depth A and pitch B represent the dimensions of the concentric grooves in terms of the amplitude and wavelength of a sine function, respectively.

Lastly, single–grooved disks are designed and manufactured as a part of this study to find out the difference between the spot–excitation with a single roughness element and an excitation with the distributed disturbance. These disks have the same diameter and thickness with the distributed concentric–grooved disks and their top surface was polished to obtain a smooth surface.

Figure 5.5: Distributed concentric grooves on the surface of a test disk.

Table 5.1: The dimensions of the distributed concentric grooves on the surfaces of the rough disks, all in microns.

Groove depth	Groove pitch	Effective depth A	Effective pitch B	$a = A/B$
100	300	50	300	0.167
100	400	50	400	0.125
100	500	50	500	0.1
100	700	50	700	0.071
200	1000	100	1000	0.1
300	500	150	500	0.3
300	1500	150	1500	0.1
500	2500	250	2500	0.1

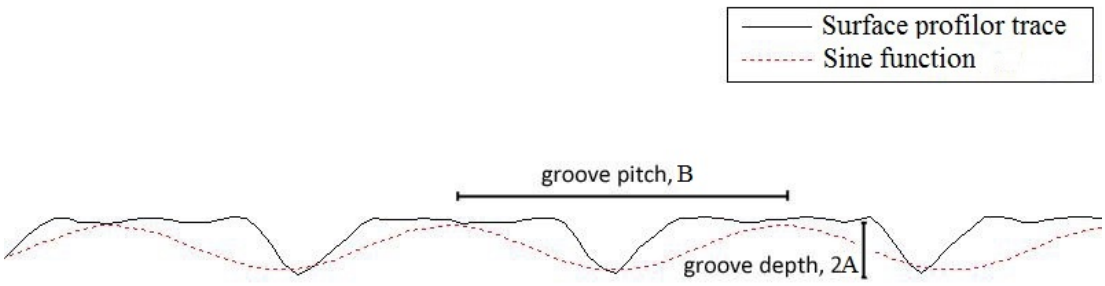

Figure 5.6: Superimposition of a sine function onto the surface profile of a distributed concentric grooved disk.

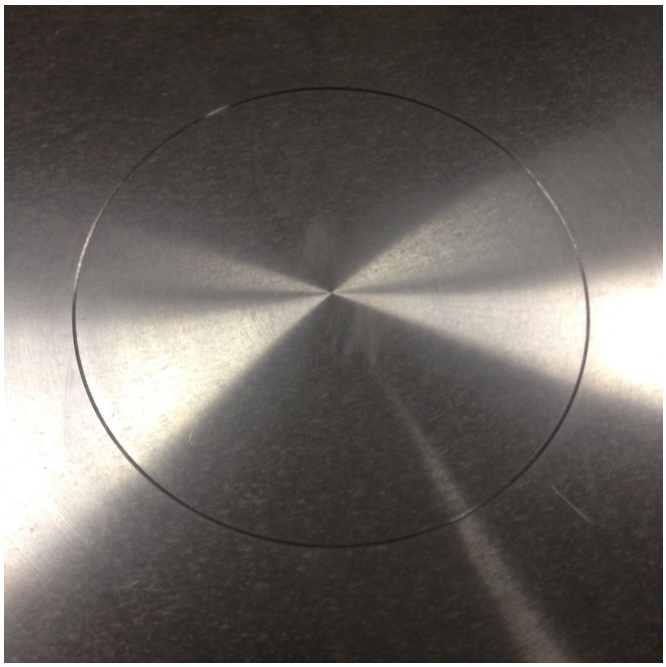

Figure 5.7: A single groove on the surface of a test disk. The diameter of the groove is 180 mm.

Then a single groove was cut in the polished surface of the disk. The depths of the grooves on two different disks are 0.5 mm and 1 mm and the diameter of the groove is 180 mm on both disks. An example of a single–grooved disk is illustrated in Figure 5.7.

5.5 Calibration

5.5.1 Introduction

In this study, a new way of calibration is introduced to resolve the questions and uncertainties that resulted from the investigations of Harris (2013) since, as mentioned before, it was difficult to draw definitive conclusions from his measurements. We refer to this new technique as the rotating–arm (RA) calibration method and it is presented in Section 5.5.3.

In the calibration of hot–film process, the most commonly used relationship between the velocity U^* and the voltage reading E from the hot–film is knows as King's law which is given by

$$E^2 = A + BU^{*n}. \tag{5.1}$$

Although this equation can be applied to a hot–film in water in principle, Wu and Bose (1993) reported that an extended King's law, of the form of

$$E^2 = A + BU^{*n} + CU^{*2n}, \tag{5.2}$$

can lead to an increase in accuracy over the simple King's law itself at low velocities. This improvement was also confirmed as a part of this study and thus the calibration curves obtained from extended King's law equation are used in the current study for changing the raw voltage measurements into velocity magnitudes.

Here, the calibration constants A, B, C and the exponent n are obtained by a least–squares curve fitting to the calibration data. Bruun (1995) reported that the exponential value n depends on the probe type, the calibration method, and the velocity range.

5.5.2 Calibration Against von Kármán Flow

The method of calibrating the hot–wire probe directly over a smooth rotating disk surface by means of the von Kármán flow was first introduced by Lingwood (1996) and then used in other studies, such as Imayama et al. (2012). This calibration technique will, hereinafter, be referred to as LK–calibration. It has already been revealed that this calibration technique is appropriate for the air–based rotating disk facilities as some of the previous results of Lingwood (1996) show a very good agreement with the velocity profiles obtained from the similarity solution of von Kármán (1921); refer to Section 2.2 for the corresponding figures. Therefore, it was thought that it is worth employing the same calibration method in our water–based rotating–disk experiments as well. The procedure for the LK–calibration is as follows.

The only known velocity for the rotating–disk flow is the rotational velocity of the disk Ω^* itself and thus the velocity of the fluid $v^* = \Omega^* r^*$ at a particular radial position r^* on the surface of the disk. Obviously, the flow velocity on the surface of the disk cannot be measured practically but the mean velocity profiles can be calculated by the similarity solution derived by von Kármán (1921). It is assumed that the actual mean velocities within the boundary layer are those predicted by the similarity solution and thus, in this method, the hot–film probes are calibrated against these theoretically predicted velocities.

For the rotating–disk flow in air–based facilities, the similarity solution accurately predicts the boundary–layer flow over the rotating disk, however, for the water–based facilities the boundary–layer flow has already been modified due to the finite size of the facility and thus the similarity solution does not exactly represent the real flow over the disk any longer. Nevertheless, the LK–calibration was reproduced in the current study for comparison with our newly proposed rotating–arm calibration method which will be introduced in Section 5.5.3.

To conduct the LK–calibration, the hot–film probe is positioned parallel to the disk surface and aligned in the flow direction correspondingly to measure the azimuthal component of the velocity. This is the dominant velocity component amongst the other two (radial and axial) in terms of their magnitude. The radial location of the probe can be adjusted by means of the 2–axis traverse system and its height over the surface of the disk can be changed precisely by the vertical vernier scale. Changing the location of the hot–film probe in both radial and axial directions leads to a calibration velocity range of $0 \leq U \leq 0.363$ m/s. The maximum velocity is defined as the maximum value that can be practically measured in the boundary–layer over the rotating disk while keeping the flow in the laminar region. This is important because the reference velocities are predicted by the similarity solution which is only valid in the laminar–flow region. Velocity profiles obtained by this method is compared with the ones produced by rotating–arm calibration method in Section 6.1.

5.5.3 Rotating–Arm Calibration Method

The basic idea of this new technique is that the rotational speed of the shaft on which the arm is mounted is known and thus the probe can be traversed/rotated in still water with known velocities by means of this arm which holds the hot–film probe. The description and the procedure for the rotating–arm calibration method are provided as follows.

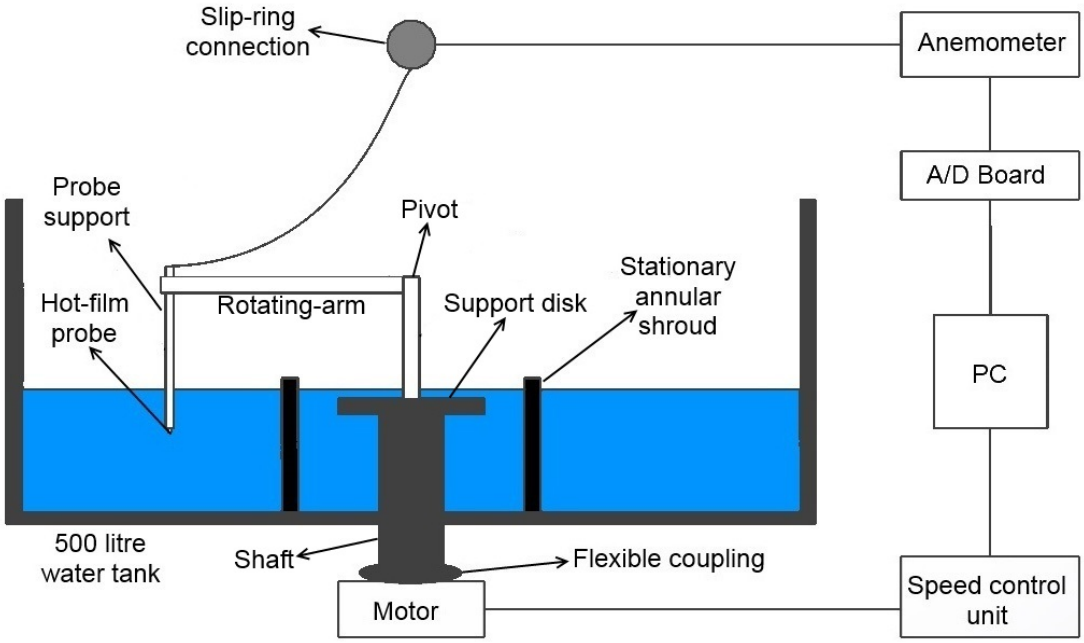

Figure 5.8: A sketch of the rotating–arm calibration method.

A simple device was manufactured particularly for this purpose. It consists of an aluminium bar (the rotating arm) with a probe support at one end and a pivot at the other end as illustrated in Figure 5.8. The pivot is secured on the support disk which is located on top of the shaft. The shaft is rotated with the motor and the angular frequency of the motor, f^*, can be controlled with a computer–based speed control unit. The rotational velocity Ω^* can be obtained by $\Omega^* = 2\pi f^*$ and also measured directly from the shaft by means of a mechanical tachometer to check the reliability of the motor. It was found that the angular frequency of the motor is in the maximum error margin of $\pm 1\%$. The linear velocity of the probe U^* in stationary water is calculated by $U^* = \Omega^* l^*$.

Here, l^* represents the length of the rotating arm from the pivot (the axis of the rotation) to the probe support that holds the probe. The connection between the rotating arm and the pivot is made by screws and thus the length of the arm l^* is adjustable. The electrical connection between the probe and the anemometer is made by a rotary slip–ring. The slip–ring is produced by Mercotac Inc and demonstrated in Figure 5.9. The connection through the slip–ring assembly is a standard technology to transfer electric signals between rotating and non–rotating systems without the requirement of cables. Although a mentor from the TSI company suggested that calibration through a slip–ring would not be possible, we tried it and managed to obtain accurate results due to the fact that the resistance of the slip–ring is less than 1 mΩ and it has extremely low electrical noise.

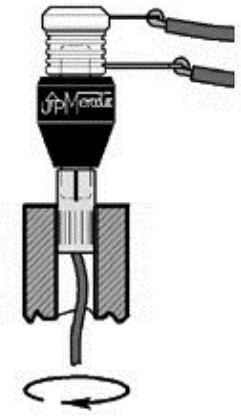

Figure 5.9: Slip–ring MERCOTAC Inc.

The motor is operated in the frequency range of $0 \leq f^* \leq 0.3183$ Hz which provides the rotational velocity range of $0 \leq \Omega^* \leq 2$ rad/s. The length of the rotating arm is fixed at $l^* = 0.3$ m which leads to the linear velocity range of $0 \leq U^* \leq 0.6$ m/s. This particular length of the rotating arm is the maximum value that can be chosen because in this case the required velocity range can be obtained with smaller angular velocities. This is important for keeping the disturbances minimum in the stagnant medium created by the rotation of the probe itself. The radius of the stationary annular shroud (*cf.* Figure 5.8) is

0.113 m which protects the stagnant medium from the wakes formed by the rotation of the support disk and the shaft. Therefore, when the arm length l^* is equal to 0.3 m, the probe is located at the middle of two stationary walls – water tank ($R^* = 0.5$ m) and annular shroud ($R^* \cong 0.1$ m) – and considered not to be affected by the wakes which may be reflected from these walls. In this manner the only disturbance in stagnant water resulted from the rotation of the probe itself and this effect is minimized by stopping the rotation of the arm after each set of voltage measurement at a known corresponding velocity and leaving water to be stagnant again before the next set.

While the probe is being rotated with various constant velocities, the hot–film output voltages obtained from the constant temperature anemometer are transferred to a PC using a 16 bit DAQ card. The input range of this card is from -10 V to $+10$ V with a sampling rate capability of 100 kilo-samples per second. The sampling frequency during the calibration is 1 kHz and this leads to a time resolution of 0.001 s. This calibration technique, hereinafter, will be referred to as RA–calibration.

5.6 Procedure for Velocity Measurements

After the completion of the calibration process, the hot–film probe is ready to take velocity measurements. The procedure for the velocity measurements is described as follows. Test disks are fixed on top of the support disk and levelled by means of three screws underneath. The hot–film probe is positioned at a required radial location above the test disk and then lowered until the probe heel barely touches the disk surface. This probe heel protects the thin wire of the probe from contacting any solid surfaces since these hot–film probes are specifically designed for boundary–layer measurements. The height of the probe heel was measured with a microscope and found to be 0.153 mm. When the probe heel touches the disk surface, therefore, the vertical position of the thin wire itself is known

with great accuracy. It can be then raised to any required vertical position using the reference height from the probe heel. Subsequently, the hot–film probe is positioned either to face the azimuthal or the radial velocity components. Note here, as a reminder, that the magnitude of the axial velocity component is much smaller than the other two and thus cannot be measured experimentally.

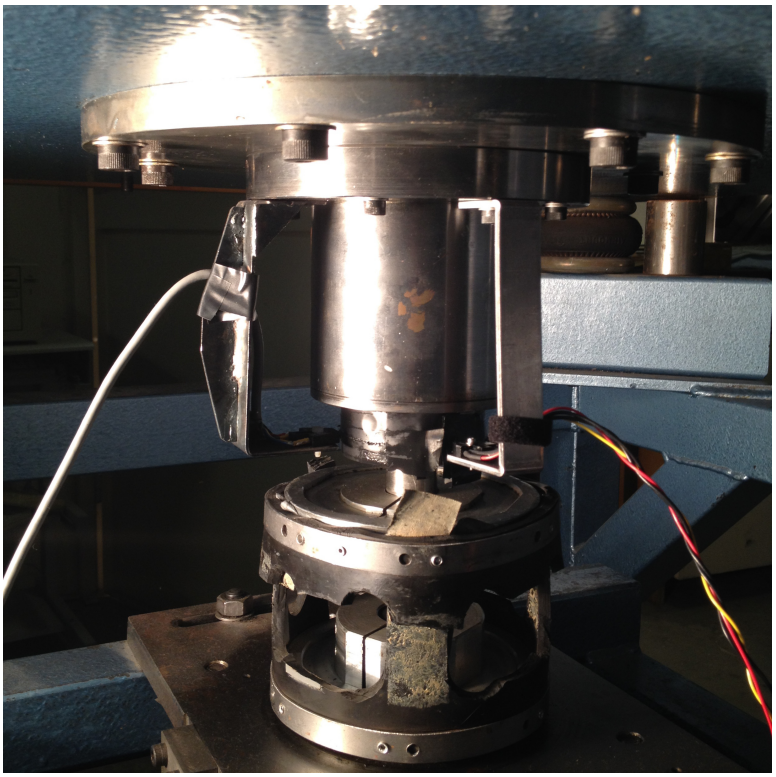

Figure 5.10: Triggering system consists of optical sensors and a metallic reflective mark on the shaft.

The motor and so the test disks are rotated at a required rotational velocity and the raw voltage signal from the CTA is digitized and recorded by means of the DAQ card at a sampling rate of 1000 data points per disk rotation. The CTA is triggered by means of optical sensors pictured in Figure 5.10 to acquire the data at exactly the same angular location at each rotation of the disk. This is performed using a metallic reflective mark attached on the main rotating shaft and thus the infrared sensor triggers the CTA every time it faces with this reflective at the same angular position of each rotation. The precision of the exact angular location becomes significant when, for instance, the velocity

and frequency fields need to be obtained by means of averaging the data over many rotations. This method is called ensemble averaging and employed in Sections 6.4, 6.6 and 6.9 of this thesis. It is very crucial to record each ensemble at the correct corresponding location at each rotation of the disk. Finally, a low pass filter of 300 Hz is applied to the recorded signal to eliminate the undesirable higher frequencies. Relevant calibration curves can then be used to transform the acquired raw voltage measurements into required velocity magnitudes.

Chapter 6

Experimental Results

6.1 Comparison of Calibration Methods

The LK–calibration was performed in the velocity range of $0 \leq U \leq 0.363$ m/s, whereas the velocity range of the new RA–calibration is $0 \leq U \leq 0.6$ m/s. This is due to the limitation on the maximum velocity determined in the first calibration method which was previously mentioned in Section 5.5.2. There are 14 calibration points used for the LK–calibration which are uniformly spaced in the related velocity range and 19 used for the RA–calibration. These numbers of calibration points are considered to be adequate since Bruun et al. (1988) reported that similar results can be obtained using 10, 20, or 40 calibration points. The DAQ card was regulated to take $100,000$ samples at a rate of 1 kHz.

Figure 6.1 compares the calibration curves produced from both methods. The exponent n of the extended King's law, given previously in Equation 5.2, was found to be 0.135 for both methods.

In order to evaluate these two calibration methods, the velocity profiles over a smooth rotating disk were produced using the derived calibration curves and these calculated profiles were then compared with the von Kármán flow. The comparison is illustrated in Figure 6.2 for the radial and in Figure 6.3 for the azimuthal velocity profiles.

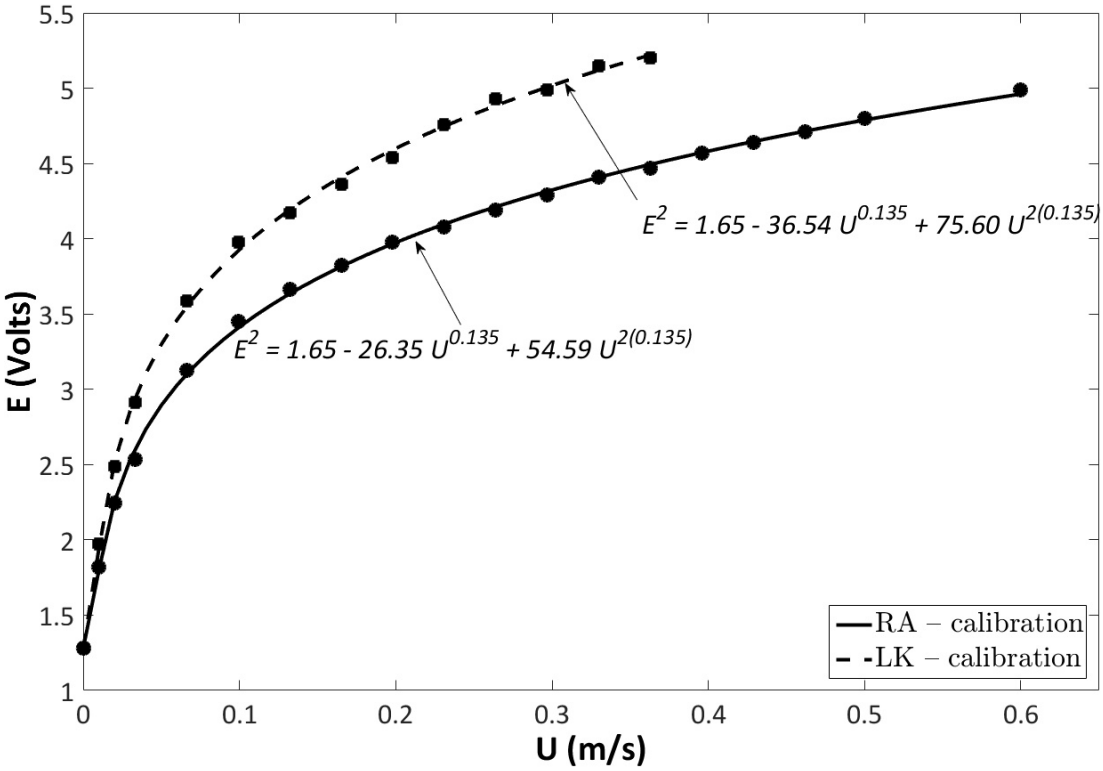

Figure 6.1: Calibration curves of extended King's law equation, $E^2 = A + BU^n + CU^{2n}$.

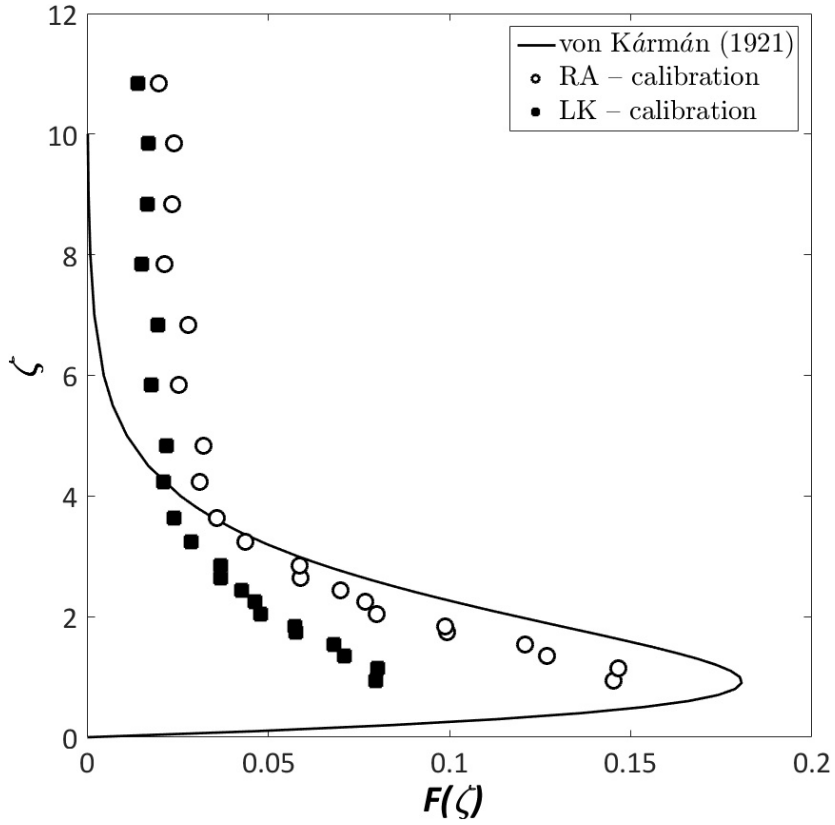

Figure 6.2: Radial velocity profiles.

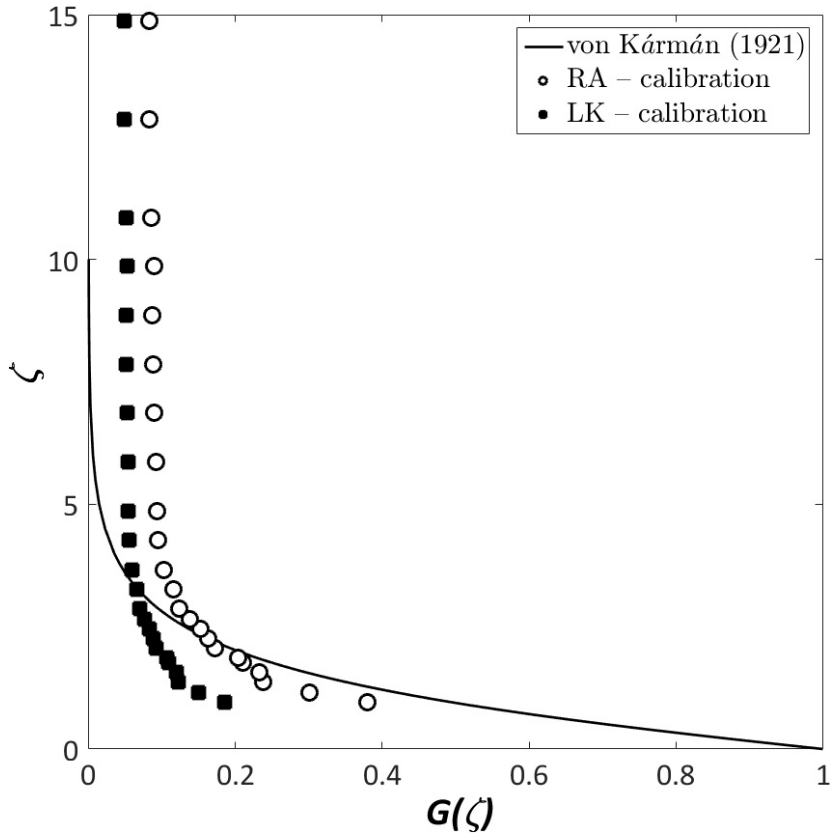

Figure 6.3: Azimuthal velocity profiles.

It can clearly be seen from these figures that the proposed RA–calibration technique is superior to the LK–calibration method. Both the radial and the azimuthal velocity profiles are still not perfectly agreed with the von Kármán flow, however, they better approximate to those theoretical curves with the use of the new method.

6.2 Yaw Angle Correction

The yaw–angle bias resulted from the along–wire cooling effect was previously mentioned in Section 4.2.2 where the experimental data of Colley et al. (1999, 2006) were referred. Due to the fact that none of the previous studies (Colley et al., 1999, 2006; Harris, 2013), corrected their data for the yaw–angle bias, it is important to employ this correction here in this study.

By the nature of the rotating–disk flow, there are two strong components

that have cooling effect on the hot–film probe close to the disk surface. If the probe is aligned to measure the azimuthal component of the velocity, for instance, it encounters a cooling effect caused by the radial flow component along the sensor or vice versa. Figure 6.4 illustrates the sketch of the along–wire cooling effect on a hot–wire probe.

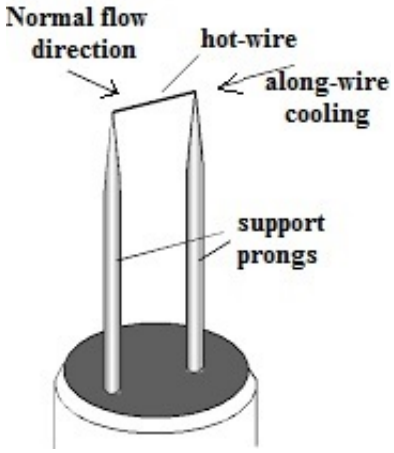

Figure 6.4: The sketch of the along–wire cooling effect on a hot–wire probe.

Usually it is the effective velocity V_e that the hot–film probes measure in the experiments which is given as

$$V_e^2 = U_N^2 + {k_y}^2 U_T^2. \tag{6.1}$$

Here, U_N is the normal velocity component which is wanted to be measured and U_T is the tangential velocity component that has the along wire cooling effect on the hot–film probe and results in the yaw–angle bias. One can calculate the normal velocity U_N when the yaw coefficient k_y in the above equation is known. To obtain the yaw coefficient k_y in this study, in the RA–calibration method, the probe was aligned to face the normal linear velocity where the yaw angle α_y of the probe is described as $\alpha_y = 0°$. This is the angle between the flow direction and the normal vector of the thin wire. In this position, the probe truly measures the linear velocity calculated by means of the rotational speed of the rotating–arm without any along–wire cooling effect, i.e. $\alpha_y = 0° \rightarrow U_N = \Omega^* l^*$ and $U_T = 0$.

Afterwards, this procedure was repeated again for the yaw angle of $\alpha_y = 90°$. In this case the voltage measured from the probe corresponds to only the along–wire cooling effect of the known linear velocity, i.e. $\alpha_y = 90° \rightarrow U_T = \Omega^* l^*$ and $U_N = 0$. The obtained voltage measurements for the yaw angles of $\alpha_y = 0°$ and $\alpha_y = 90°$ are plotted against the velocity in Figure 6.5.

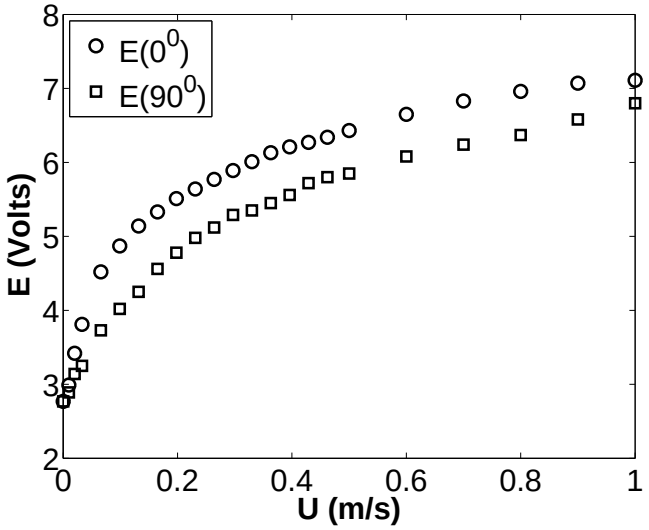

Figure 6.5: Data obtained by rotating–arm calibration method at $\alpha_y = 0°$ and $\alpha_y = 90°$.

The only remaining unknown in Equation 6.1 is now the yaw coefficient which can be calculated easily. The voltage measurements at the corresponding velocities and the calculated yaw coefficients are listed in Table 6.1.

The values of ${k_y}^2$ are then plotted against the velocity in Figure 6.6. It can be seen that for low velocities below 0.2 m/s and high velocities above 0.8 m/s, the ${k_y}^2$ values differ significantly. However, the range of the velocity mainly used in the current experiments is $0.2 - 0.6$ m/s. Therefore, the values of the yaw coefficient are decided to average in this velocity range and the acquired value is ${k_y}^2 \cong 0.067$. This is in the range of a typical value of ${k_y}^2$ which is reported as $0.04 \leq {k_y}^2 \leq 0.16$ by Bruun (1995).

Before the application of the yaw angle correction to the velocity profiles, the cooling effects of each velocity component on the other one were evaluated using Equation 6.1. When the hot–film probe is positioned perpendicular to the

Table 6.1: Yaw coefficient, k_y, data obtained by rotating–arm calibration method

$\mathbf{U(m/s)}$	$\mathbf{E(0^\circ)}$	$\mathbf{E(90^\circ)}$	$\mathbf{k_y}$	$\mathbf{k_y{}^2}$
0.000	2.77	2.77	1	1
0.010	2.99	2.89	1.020877	1.042191
0.020	3.42	3.14	0.508868	0.258947
0.033	3.81	3.25	0.309072	0.095525
0.066	4.52	3.73	0.35939	0.129161
0.099	4.87	4.02	0.396771	0.157427
0.132	5.14	4.25	0.409771	0.167912
0.165	5.33	4.56	0.478711	0.229164
0.198	5.51	4.78	0.501555	0.251558
0.231	5.64	4.98	0.536098	0.287402
0.264	5.77	5.12	0.539994	0.291593
0.297	5.89	5.29	0.56449	0.318649
0.330	6.01	5.35	0.532017	0.283042
0.363	6.13	5.45	0.520747	0.271177
0.396	6.21	5.56	0.535097	0.286328
0.429	6.27	5.72	0.588399	0.346213
0.462	6.34	5.8	0.593926	0.352748
0.500	6.43	5.85	0.571552	0.326672
0.600	6.65	6.08	0.57847	0.334628
0.700	6.83	6.24	0.569859	0.324739
0.800	6.96	6.37	0.572351	0.327585
0.900	7.07	6.58	0.632486	0.400039
1.000	7.11	6.8	0.750787	0.563681

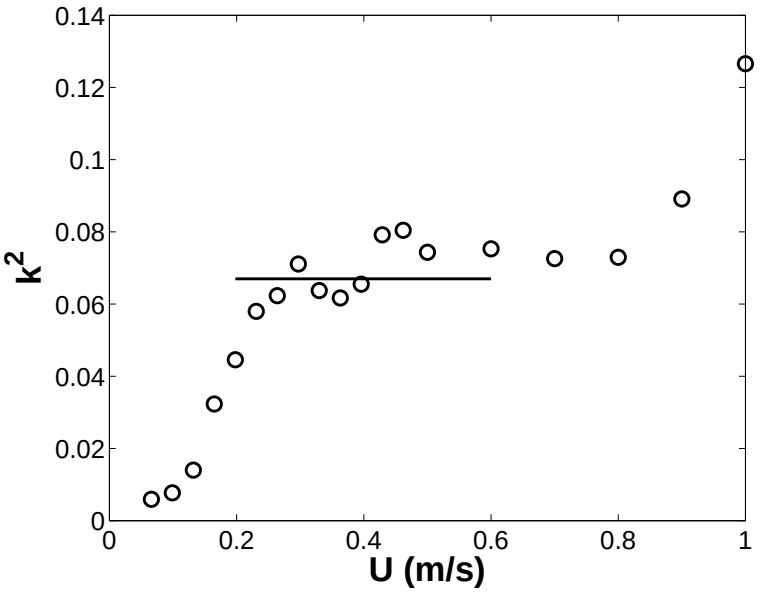

Figure 6.6: Yaw coefficient, $k_y{}^2$.

flow direction of the radial velocity component; U_N in Equation 6.1 represents the radial component and U_T represents the azimuthal component. In terms of the similarity solution by von Kármán (1921), these are $F(\zeta)$ and $G(\zeta)$, respectively, and Equation 6.1 takes the following form:

$$V_e^2 = F(\zeta)^2 + {k_y}^2 G(\zeta)^2. \tag{6.2}$$

Using the similarity solution, the magnitudes of the terms in Equation 6.2 can be obtained and the ratio of ${k_y}^2 G(\zeta)^2$ to $F(\zeta)^2$ is shown in Figure 6.7.

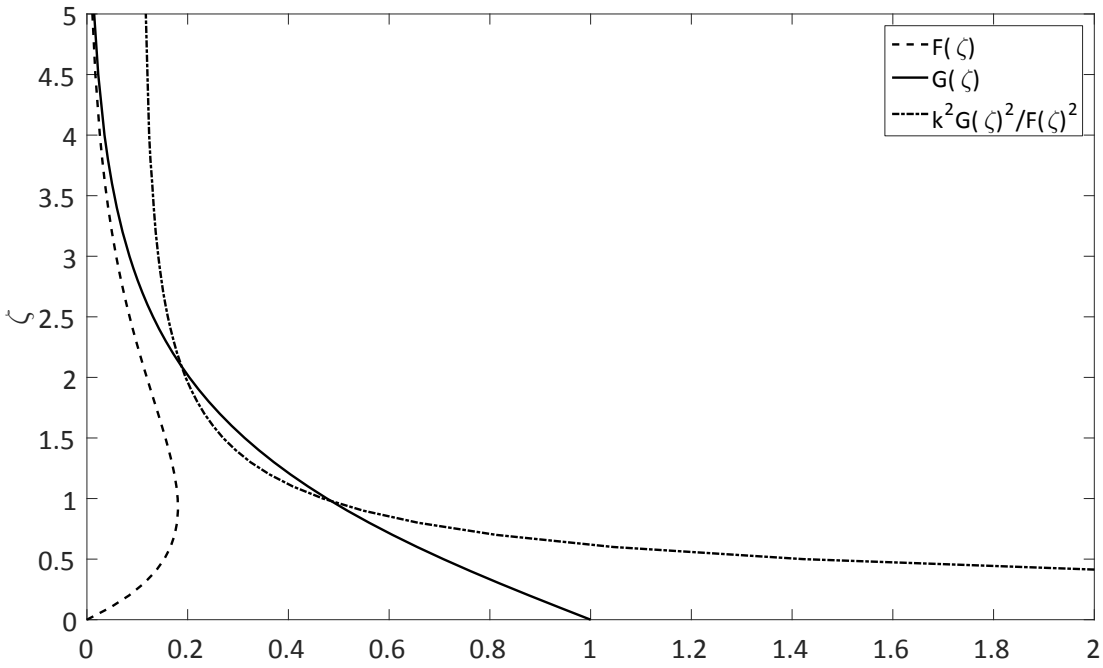

Figure 6.7: Effective cooling near the surface of the rotating disk.

It can be seen in Figure 6.7 that the ratio tends towards infinity in the vicinity of the disk surface where $\zeta < 0.5$. This indicates the significant effect of the azimuthal flow component on the radial component and makes the radial velocity component almost impossible to be distinguished and measured experimentally. In this study, however, the radial velocity component was acquired above the vertical location of approximately $\zeta \approx 0.57$ where the influence of azimuthal component on the radial component is modest. This vertical location is, nevertheless, the nearest position of the hot–film probe to the disk surface due to

the restriction arises from the heel of the probe.

Figure 6.7 also reveals that the cooling effect of the radial flow component on the azimuthal flow component is negligible and thus the velocity profiles of the azimuthal flow component in this study were not modified. However, all of the velocity profiles of the radial flow component illustrated in this study were corrected correspondingly by means of the yaw–angle coefficient.

To solve the '*real*' radial velocity component $F(\zeta)$ in Equation 6.2, the azimuthal velocity component $G(\zeta)$ needs to be known at each of the corresponding height above the disk surface. Therefore, $G(\zeta)$ was acquired using the same hot–film probe that was positioned perpendicular to the flow direction of the azimuthal velocity component.

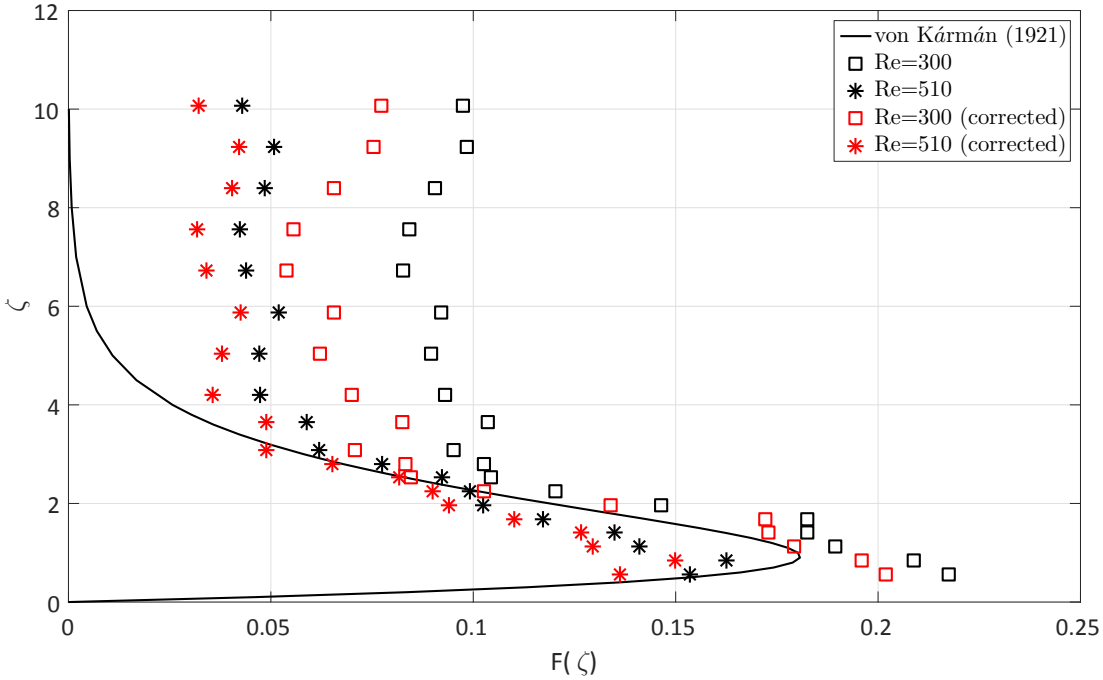

Figure 6.8: Radial velocity profiles with yaw–angle correction at $Re = 300$ and $Re = 510$. Red symbols indicate corrected profiles.

The corrected profiles of the radial component of the velocity over a smooth disk at $Re = 300$ and $Re = 510$ are illustrated as an example in Figure 6.8. Red symbols in the figure indicate the corrected velocity profiles and black symbols indicate the profiles without any yaw–angle correction. It can be seen that, with the correction, the magnitude of the radial velocity component is reduced of the

order of around $\Delta F \approx 0.02$ which corresponds to about 2% in comparison to the maximum value of $F \approx 0.18$. More importantly, in the region of approximately $0 \leq \zeta \leq 2$ where the magnitude of the azimuthal velocity component is substantial and thus its effect on the radial velocity component is significant; the radial velocity component seems to approximate the similarity solution with the applied yaw–angle correction.

6.3 Velocity Profiles

6.3.1 Velocity Profiles over Smooth Disk

Although some of the velocity profiles have already been provided in the preceding sections, the comprehensive presentation is given in this section. Also as a reminder, the operational procedure of the velocity measurements was described in Section 5.6. The rotational velocity of the disk was 1.25 rev/s during the measurements which corresponds to 7.85 rad/s. This enables us to compare our results directly with the previous studies by Colley et al. (1999, 2006) and Harris (2013). According to this rotational velocity, the maximum Reynolds number of the system is approximately $Re \cong 540$ for this investigation.

Figure 6.9 shows the radial velocity profiles that were obtained over the surface of a smooth disk. These measurements were taken at various radial locations which correspond to $Re = 200$, $Re = 300$, $Re = 400$, $Re = 510$ and $Re = 530$. Therefore, the entire flow domain was covered from the laminar to the fully turbulent flow. Note here that the critical Reynolds number for transition to turbulence varies but the common expectation is that the flow cannot be laminar beyond $Re > 508$ (Lingwood, 1996).

One of the main features seen in Figure 6.9 is the dependence of the flow profiles on the Reynolds number. The noisy data is expected for the higher Reynolds numbers where the flow is turbulent but the velocity profiles are also

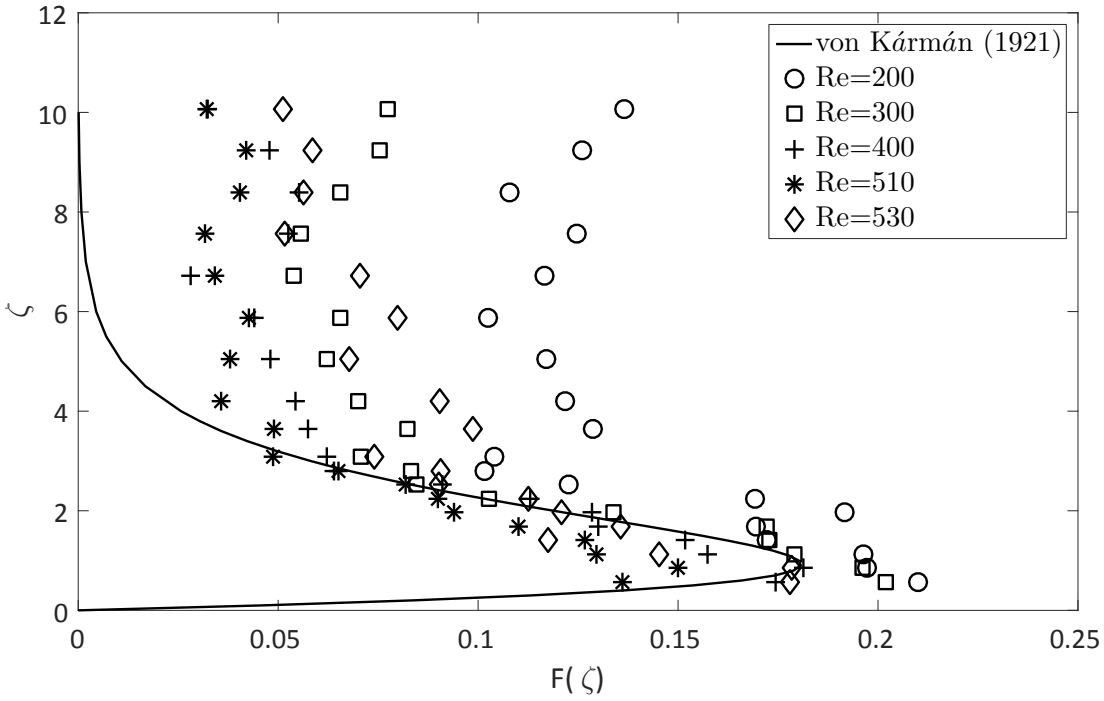

Figure 6.9: Radial velocity profiles $F(\zeta)$ obtained experimentally at radial locations that correspond to $Re = 200$, $Re = 300$, $Re = 400$, $Re = 510$ and $Re = 530$ at $\Omega = 7.85$ rad/s.

noisy in the laminar region, see for instance the profile at $Re = 200$. This is probably due to the deformation of the free–surface of water in the vicinity of the rotational axis and the whole the core rotation of water which occur unavoidably. This deformation is pictured in Figure 6.10. This strong vortex appearing in the vicinity of the rotation axis may, further, explain the reason why the magnitude of the core rotation is higher for the lower Reynolds numbers.

Although the radial flow profiles in Figure 6.9 seem to be a lot better than the ones provided by Harris (2013), please refer to Figure 6.1 in that study for comparison, our profiles are still not in good agreement with the von Kármán flow apart from a small vertical region of $1 \lesssim \zeta \lesssim 3$. Especially, after above $4 < \zeta$, the profiles are strongly modified in comparison to the similarity solution of Kármán (1921). This indicates that the use of an air–based experimental facility is required to achieve as good results as the ones provided by Lingwood (1996), Corke et al. (2007) and Imayama et al. (2012).

In addition to radial profiles, azimuthal flow profiles were obtained over

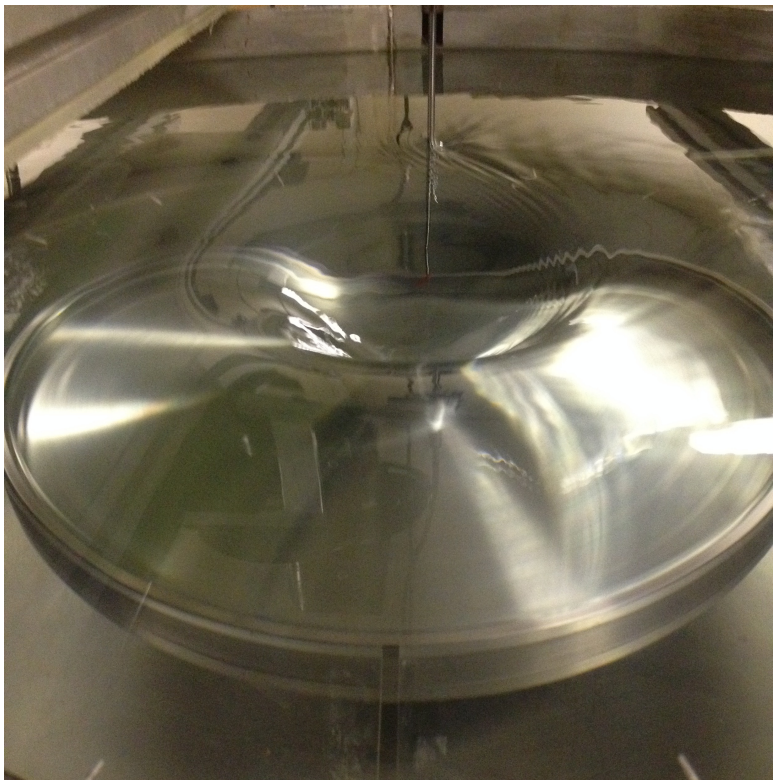

Figure 6.10: The deformation of the free–surface of water in the vicinity of the rotational axis.

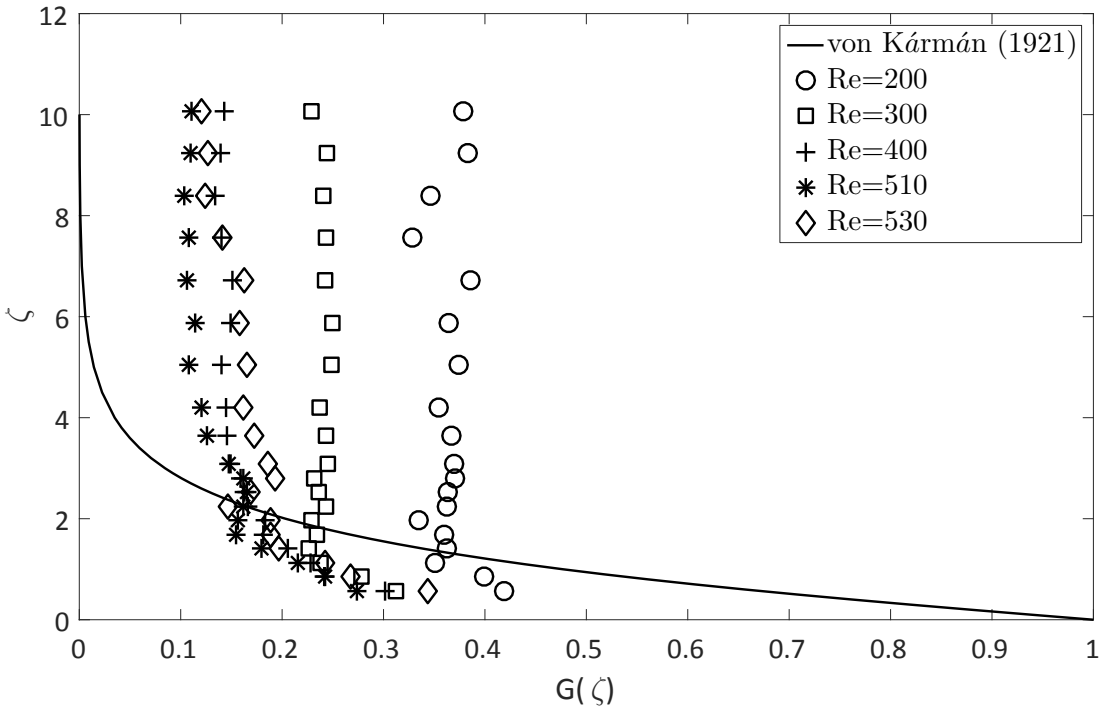

Figure 6.11: Azimuthal velocity profiles $G(\zeta)$ obtained experimentally at radial locations that correspond to $Re = 200$, $Re = 300$, $Re = 400$, $Re = 510$ and $Re = 530$.

the surface of a smooth disk and are presented here in Figure 6.11. Similar to the radial profiles, the azimuthal profiles are also dependent on Reynolds number. This dependence is more strong for low Reynolds numbers, see for instance $Re = 200$ and $Re = 300$. However, the dependence seems to vanish when the Reynolds number is increased to the values of $Re = 400$, $Re = 510$ and $Re = 530$. A similar feature is also observed in Figure 6.9 for radial velocity profiles. Also again, the magnitude of the core rotation of water is higher at low Reynolds numbers due to the same reason (strong vortex in the central domain) previously mentioned for the radial velocity profiles and this observation is consistent with our numerical results; refer to Section 4.3.

Moreover, despite the fact that the magnitude of the core rotation of the fluid far above the disk surface is dependent on Reynolds number for $Re = 200$ and $Re = 300$, it is constant approximately at $G(\zeta) \approx 0.15$ above the non–dimensional height of $\zeta > 3$ for the higher Reynolds numbers of $Re = 400$, $Re = 510$ and $Re = 530$.

6.3.2 Velocity Profiles over Rough Disks

Measurements of both radial and azimuthal velocity components were also acquired over disks with rough surfaces and the velocity profiles are illustrated in Figure 6.12 and Figure 6.13, respectively. The reduction in the maximum value of the radial jet flow with an increase in the roughness level can be observed in Figure 6.12. The cross sign '$\times$' in the figure corresponds to the highest roughness ratio $a = A/B = 0.3$ among the others. This is the disk with the groove depth of $A = 300$ μm and the groove pitch of $B = 500$ μm. This observation can be understood since it is the groove depth, i.e. the physical height of roughness, which blocks the fluid in the vicinity of the disk surface to flow radially outwards and thus results in the reduction in the magnitude of the radial jet flow. This effect of the roughness height is also consistent with our previously mentioned

numerical results.

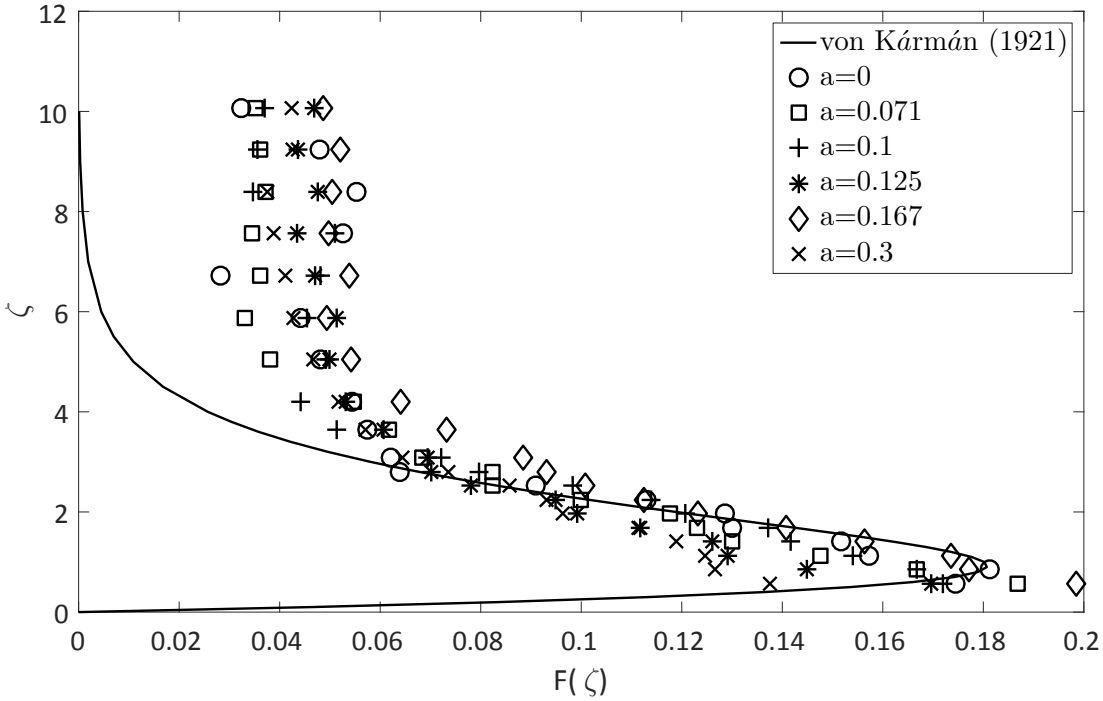

Figure 6.12: Radial velocity profiles $F(\zeta)$ obtained at $Re = 400$ and $\Omega = 7.85$ rad/s for concentric–grooved disks.

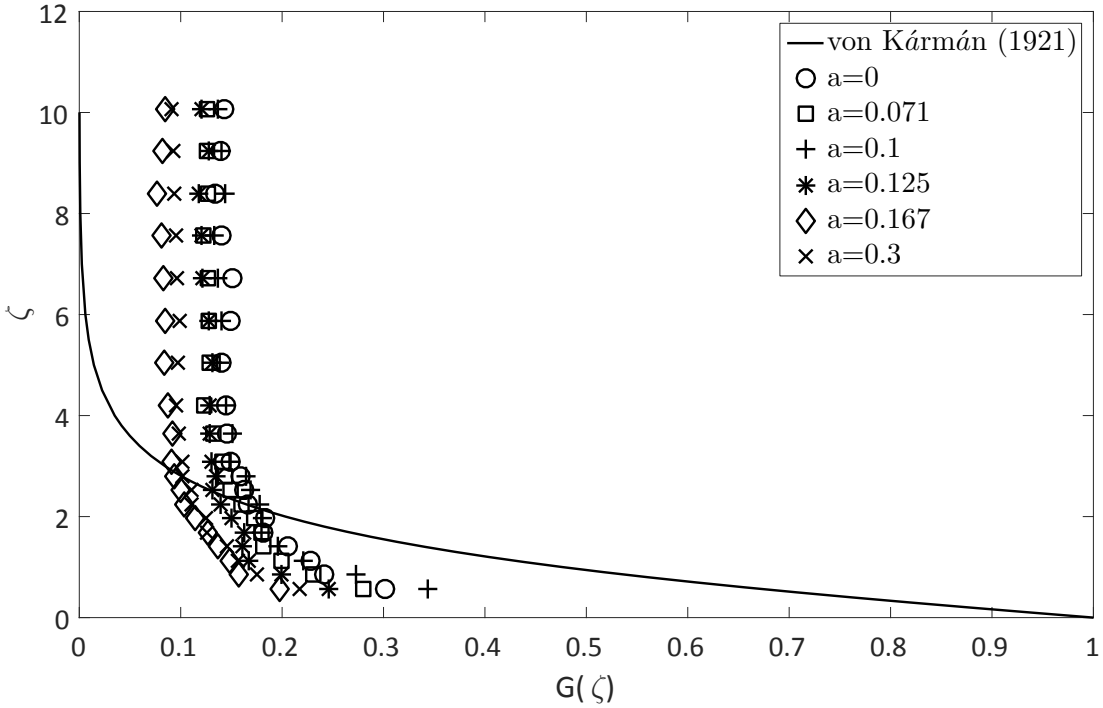

Figure 6.13: Azimuthal velocity profiles $G(\zeta)$ obtained at $Re = 400$ and $\Omega = 7.85$ rad/s for concentric–grooved disks.

The effect of roughness on azimuthal flow components are shown in Fig-

ure 6.13. One can observe from the figure that the magnitude of the core rotation of the fluid above approximately $\zeta > 3$ is decreased with an increase in the roughness level. The maximum difference between the magnitudes of core rotation that is caused by the roughness is approximately $\Delta \approx 0.05$. There is no physical explanation for this observation but the level of this difference is relatively small and may be considered as arising from the experimental errors.

6.4 Velocity Fields

Visualizing the velocity field for the entire flow domain of a rotating–disk boundary layer can give insights into the characteristics of the flow and the transition process from laminar to turbulent. For this visualization, the hot–film probe needs to be placed with the smallest possible increment in the radial direction from the centre to the edge of the rotating disk. This increment in radial direction was chosen as 0.005 mm since it is hard to distinguish the differences in the hot–film signals for even smaller increments than this value. Additionally, this was the value used by Harris (2013) who carried out experiments in the same experimental facility and this enables us to compare our results with this previous research.

Due to the existence of only one hot–film probe, the complete flow domain needs to be established by means of the combination of the individual measurements acquired at various radial locations. As a result of this limitation, any travelling waves or effects that vary in time cannot be observed. However, stationary waves or effects which do not change in time can be captured and this is sufficient in the context of this study since even a minute roughness element can increase the amplitude of the stationary modes which will then cover and dominate the entire flow field. Therefore, stationary modes are more amplified than the travelling modes for the rotating–disk boundary–layer flow. This issue was also addressed earlier in Section 2.6.

To visualize the characteristics of the whole flow domain, the hot–film probe was positioned at radial locations vary from $r = 0.04$ m to $r = 0.19$ m with 0.005 mm increments, remembering that the radius of the rotating disk is 0.194 mm. This range of the radial locations corresponds to the range of Reynolds numbers varies from $Re = 112$ to $Re = 531$ with increments of $Re = 14$. Therefore, the entire flow domain was captured from laminar to turbulent, including the transition region. The vertical location of the probe was $z \cong 0.44$ mm which corresponds to $\zeta = 1.3$. All the measurements for producing the velocity fields were taken at this vertical position above the surface of the rotating disk since this height was reported by Lingwood (1996) and Imayama et al. (2012) as the location where the maximum stationary perturbations occur. Instead of obtaining data only for a single rotation of the disk, 60 rotations were taken and then the ensemble averaging was applied to the data to reduce random fluctuations and obtain one velocity trace for a single rotation. This method was previously used, for instance, by Jarre et al. (1996a), Lingwood (1996), Colley et al. (1999), and Harris (2013). By means of this ensemble averaging, any effects caused by the travelling waves were removed and thus the fluctuations in the velocity traces correspond to the stationary waves only. The signal–to–noise ratio is proportional to the square root of the number of ensembles (Skoog et al., 2007) and thus it is $\sqrt{60}$ in the current study. Velocity fields were produced for the smooth disk, the single–grooved disks, and the concentric–grooved disks. The rotational velocity was $\Omega = 7.85$ rad/s during these measurements which corresponds to a boundary layer thickness of $\delta \cong 2$ mm.

Harris (2013) also, previously, performed these investigations using an uncalibrated hot–film probe and thus the flow field had to be displayed only in terms of raw voltage measurements in that study. However, we are able to use a calibrated probe in the current investigation and therefore the flow domain can be represented in terms of velocity magnitudes. This improvement in the current study also enables us to perform the approach of Imayama et al. (2012), intro-

duced previously in Section 2.6, for the investigation of the transition process by means of the PDF contour plots of the fluctuation velocities. This investigation is addressed in Section 6.9.

6.4.1 Velocity Fields over Smooth Disks

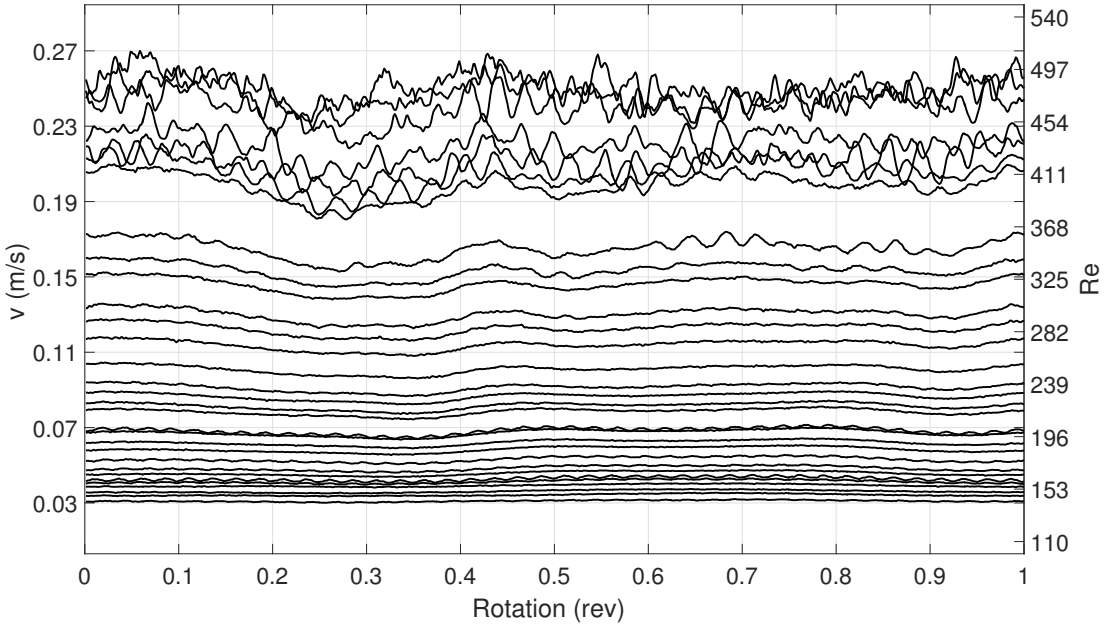

Figure 6.14: Ensemble averaged azimuthal velocity traces taken over the smooth disk at $\zeta = 1.3$ and $\Omega^* = 7.85$ rad/s.

The velocity field over the smooth rotating disk is illustrated in Figure 6.14. The x–axis represents the rotation of the disk and the data shown here is for a single rotation but produced from the ensemble averaging of 60 revolutions. Apart from tiny fluctuations in the velocity traces at $Re = 155$ and $Re = 200$, the data shows the laminar region of the flow clearly up to the Reynolds number of approximately $Re = 280$. These small fluctuations in the early Reynolds numbers might result from the disturbances reflected from the deformation of the free-surface of water in the vicinity of the rotational axis which was previously pictured in Figure 6.10 and/or the mains frequency of 50 Hz.

Subsequent to the laminar region described above, the velocity traces between approximately $Re = 280$ and $Re = 410$ show the appearance of discrete

waves which are growing in amplitude with the increase in the Reynolds number. These waves observed in the velocity traces represent the stationary vortices with respect to the rotation of the disk, remembering that any travelling waves were removed with the application of the ensemble averaging. The number of the waves on velocity traces in Figure 6.14 may not be easily recognized, however, including the waves with very small amplitudes, on a single trace one may still notice approximately 30–31 waves. This is in the range of typical values of stationary vortices between 28 and 31 which was previously mentioned in Section 2.6. Beyond $Re = 410$, the velocity traces lost their periodicity, however, one can still observe the stationary vortices up to approximately $Re = 480$. Beyond this Reynolds number, the stationary vortices cannot be tracked any more and the flow is transformed into fully turbulent regime.

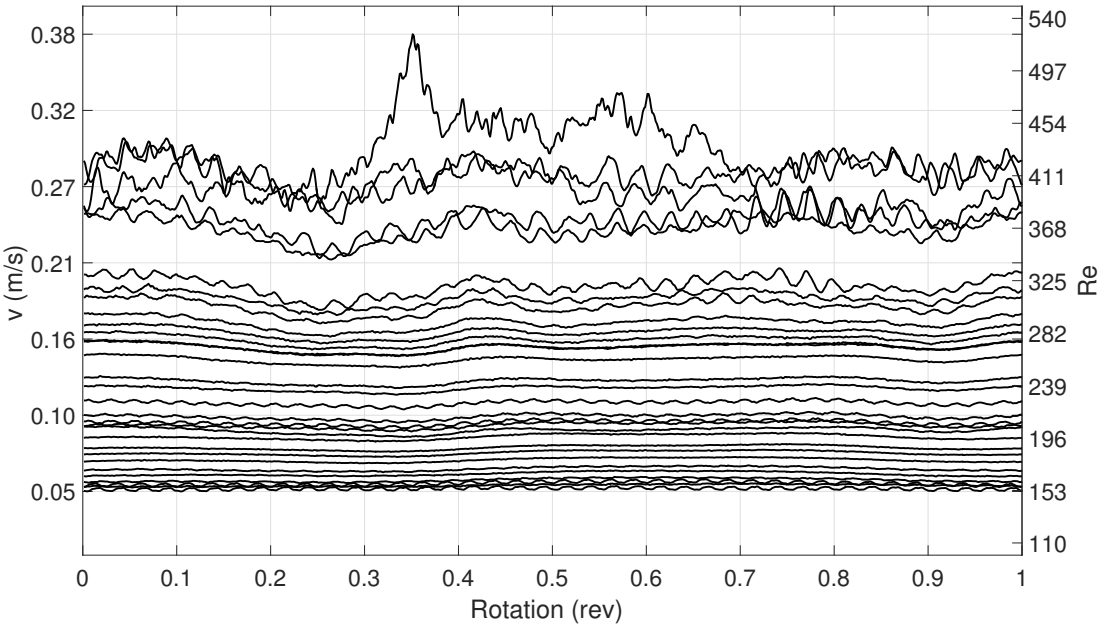

Figure 6.15: Ensemble averaged azimuthal velocity traces taken over the smooth disk which was deliberately positioned off–centre. The data were collected at $\zeta = 1.3$ and $\Omega^* = 7.85$ rad/s.

The rotational symmetry in the experiments is significantly important because even small misalignment of the test disk may lead to a considerable oscillation at high rotational speeds. The vibrations result from the oscillation of the disk may lead to substantial fluctuations and ruin the boundary–layer flow. In

order to see this importance of the rotational symmetry, the central point of the smooth disk was deliberately positioned off–centre, i.e. the difference between the centre of the support disk and the centre of the smooth test disk was 4 mm. Figure 6.15 shows the ensemble averaged velocity traces for this off–centred smooth disk. As expected, the off–centre rotation results in large oscillations in the flow field, especially at the radial positions where the probe was close to the edge of the disk where $Re \gtrsim 410$. The laminar region can still be observed but the tiny fluctuations in the velocity traces at small Reynolds numbers are more than the properly centred smooth disk (*c.f.* Figure 6.14). Due to these detrimental effects of the off–centred rotation, test disks need to be placed and positioned on top of the support disk with a high precision as it has been done in the current study.

6.4.2 Velocity Fields over Single–Grooved Disks

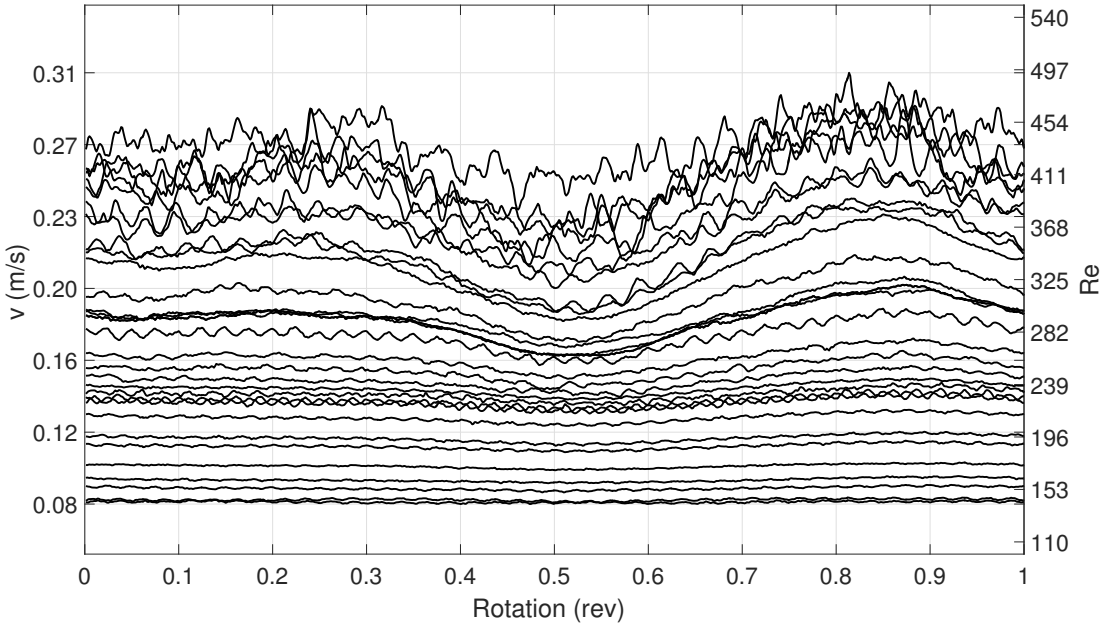

Figure 6.16: Ensemble averaged azimuthal velocity traces taken over a single–grooved disk with a groove depth of $A = 1$ mm. The data were collected at $\zeta = 1.3$ and $\Omega^* = 7.85$ rad/s. The groove is at $Re = 252$.

The velocity field obtained for a single–grooved disk is illustrated in Figure 6.16. Due to the single circular groove at the radial location of $r^* = 0.09$ m and with a groove depth of 1 mm, the transition from laminar to turbulent is trig-

gered at $Re = 252$. This transition can be seen in Figure 6.16 between $Re = 252$ and $Re = 368$. Beyond $Re \cong 368$, the flow seems to be fully turbulent. Additionally, the existence of the single groove seems to result in very large oscillations of velocity traces beyond $Re \cong 300$. These type of large oscillations are not observed even in Figure 6.15 which shows the flow field over the deliberately off–centred smooth disk.

6.4.3 Velocity Fields over Concentric–Grooved Disks

Furthermore, the velocity fields were produced for the disks with distributed concentric grooves. Figure 6.17, for instance, illustrates the velocity field for the disk with $A = 0.05$ μm and $B = 0.7$ μm and thus the roughness ratio is $a = A/B = 0.071$. In comparison with the smooth disk case shown in Figure 6.14, the transition seems to start earlier for the rough disk with $a = 0.071$ at approximately $Re \cong 240$ and exists until around $Re \cong 410$. Beyond this Reynolds number the flow seems to be fully turbulent.

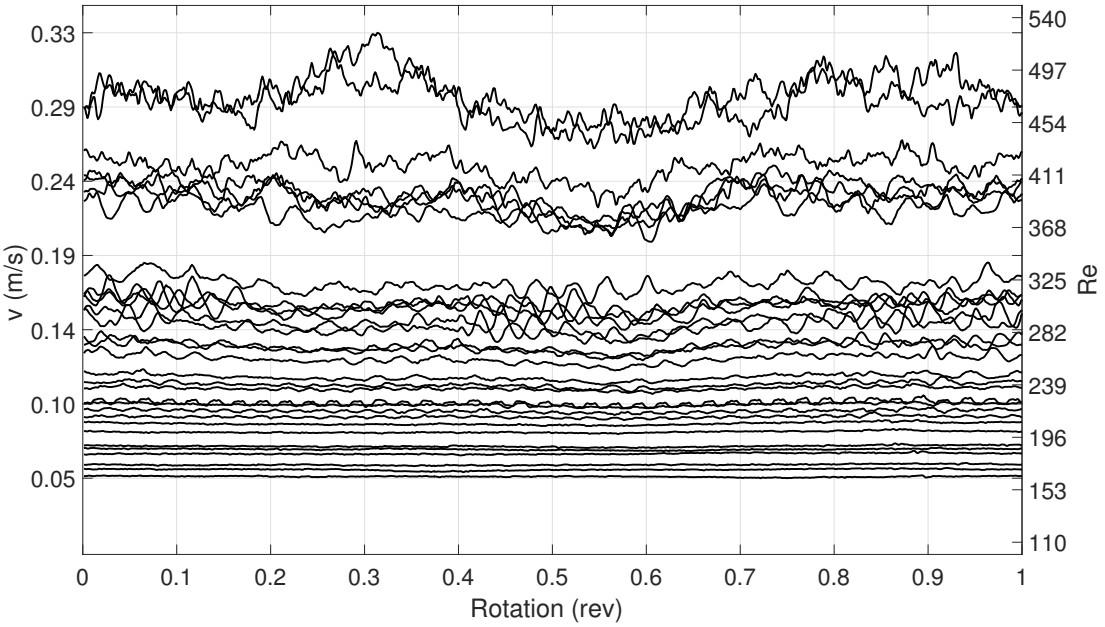

Figure 6.17: Ensemble averaged azimuthal velocity traces taken over the disk with distributed concentric grooves, $a = 0.071$. The data were collected at $\zeta = 1.3$ and $\Omega^* = 7.85$ rad/s.

Figure 6.18 shows the corresponding data for the disk with the roughness

ratio of $a = 0.167$. As a result of the increased roughness ratio, in this figure, the oscillations seem to be larger than the ones obtained for the roughness ratio of $a = 0.071$ shown in Figure 6.17. Moreover, the transition seems to start at approximately $Re \cong 282$ and the flow appears to be fully turbulent beyond $Re \gtrsim 368$. Additionally, there is an area of large fluctuations in the velocity field between $Re = 282$ and $Re = 460$ and in the range of a rotation between 0.75 and 1. There could not be drawn any general conclusions regarding this feature.

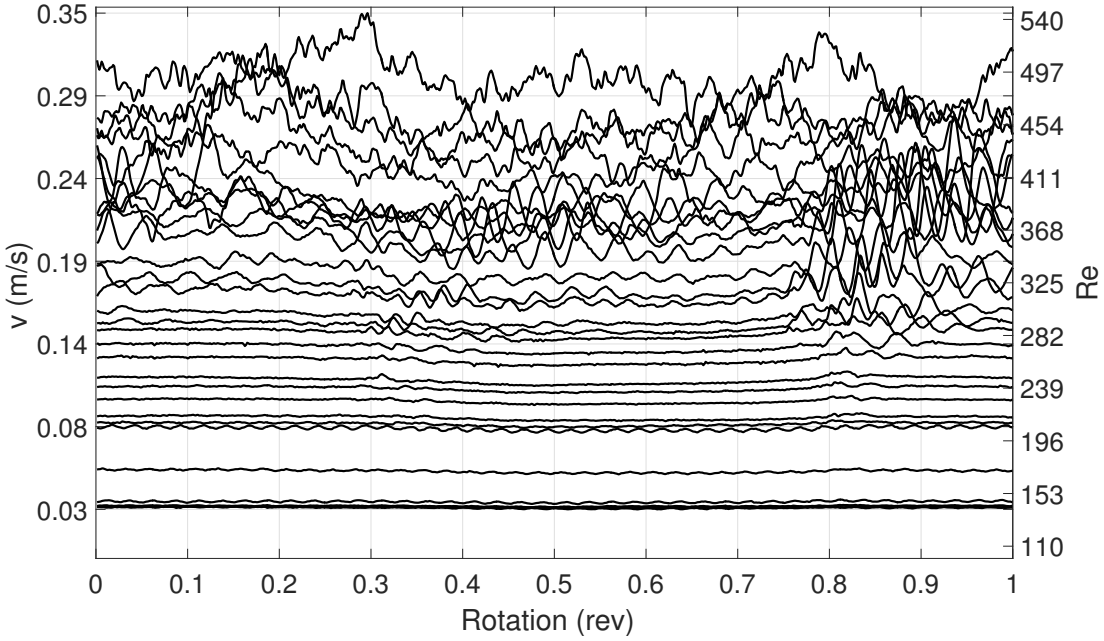

Figure 6.18: Ensemble averaged azimuthal velocity traces taken over the disk with distributed concentric grooves, $a = 0.167$. The data were collected at $\zeta = 1.3$ and $\Omega^* = 7.85$ rad/s.

Although it is hard to make conclusive comments from the figures provided in this section about the effects of roughness on the velocity fields, they make valuable contributions to the understanding of the flow field for disks with various types of surfaces. Nonetheless, Sections 6.6 and 6.9 will include figures which can better visualize the flow field and provide additional information for drawing comprehensive conclusions.

6.5 RMS Values of Velocity Profiles

Following Imayama et al. (2012), as previously introduced in Section 2.6, the root mean square (rms) values of the azimuthal fluctuation velocity v^*_{rms} at various Reynolds numbers were obtained over the smooth disk using 1600 data points per disk rotation recorded by means of the hot–film probe.

To obtain the appropriate figure associated with v^*_{rms}, the hot–film probe was located at various radial locations that correspond to Reynolds numbers of $Re = 200$, $Re = 430$, $Re = 470$, $Re = 510$, $Re = 550$, $Re = 590$ and $Re = 630$. These Reynolds numbers were chosen to enable a direct comparison with the previous study by Imayama et al. (2012). The rotational velocity of the disk was 2 rev/s which corresponds to $\Omega^* = 12.57$ rad/s and thus the maximum Reynolds number of the system was $Re = 686$ during these measurements.

The azimuthal velocity fluctuations v^*_{rms} were normalized with the wall speed at the corresponding radial location as $v_{rms} = v^*_{rms}/(\Omega^* r^*)$. These non–dimensional values of v_{rms} were then plotted on a logarithmic scale against the non–dimensional vertical height ζ which is shown in Figure 6.19.

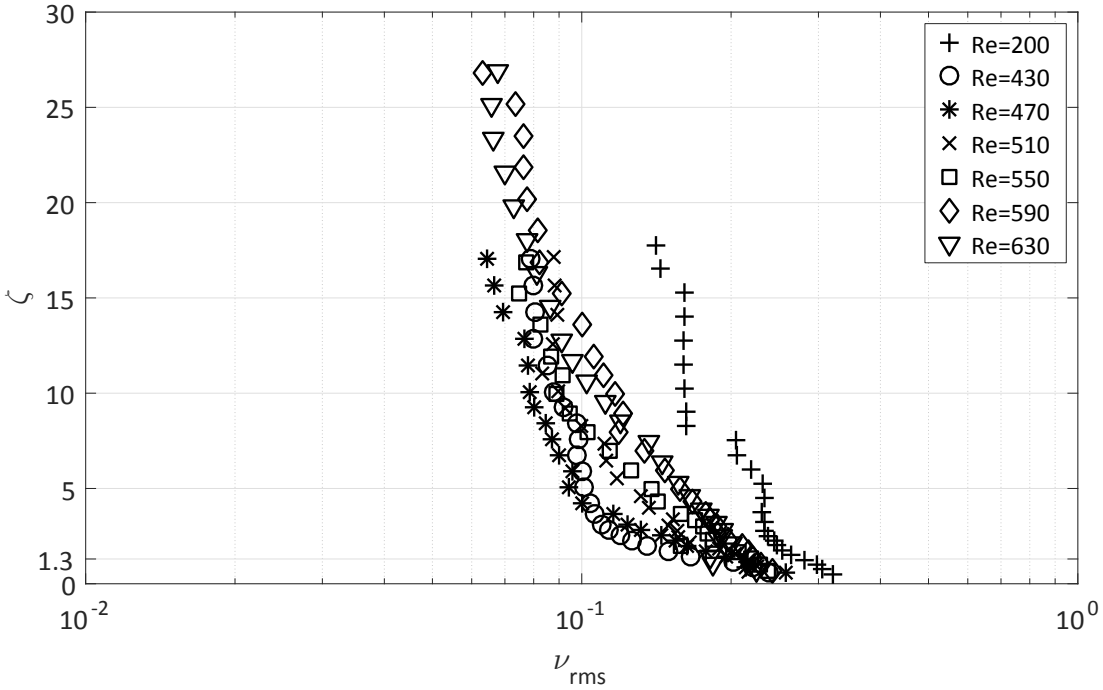

Figure 6.19: Profiles of v_{rms} at $\Omega^* = 12.57$ rad/s.

In contrast to the data of Imayama et al. (2012), (*c.f.* Figure 2.9 in Section 2.6), our v_{rms} profiles seem to be better organized at a v_{rms} range of approximately between 0.06 and 0.3. However, the v_{rms} values at $Re = 200$ slightly differ from others with indicating more fluctuations in the flow field at this Reynolds number. Theoretically, the flow is known to be laminar at this Reynolds number but the deformation of the free–surface of water shown in Figure 6.10 might be the explanation of these fluctuations at $Re = 200$ where the radial location of this measurement is close to the mentioned deformed flow region.

The v_{rms} profile at $Re = 510$ in Imayama et al. (2012) has developed a well–defined maximum at the vertical location of approximately $\zeta = 1.3$. This maximum is important since it describes the vertical position where the radial disturbances, such as stationary vortices, strongly appear. However, none of our v_{rms} profiles show that type of maximum and their magnitudes continue to increase towards the disk surface. Due to the practical restrictions, such as the probe heel height, mentioned in Section 5.6, we cannot take measurements below the vertical location of $\zeta \cong 0.18$. Therefore, and as a result of the risk of damaging the probe at very close locations to the disk surface, in the current study, we decided to take the measurements at the same value of $\zeta = 1.3$ as Imayama et al. (2012) for producing the frequency fields (Section 6.6) and the PDF contour maps (Section 6.9).

6.6 Frequency Spectra

The velocity fields, shown in Section 6.4, provide valuable flow characteristics but it can be difficult to distinguish and decide the accurate number of stationary vortices in the flow domain from those figures. Therefore, it is helpful to illustrate the flow field with a different technique. For this purpose, following Jarre et al. (1991), the velocity traces from Section 6.4 were converted from the time domain to the frequency domain by applying a Fast Fourier Trans-

form (hereinafter FFT). By means of this transformation, 60 frequency–amplitude plots were obtained at each Reynolds number. Note that the velocity fields shown in Section 6.4 were obtained based on the ensemble averaging of 60 individual velocity traces and here the FFT was applied to these individual traces before ensemble averaging. However, the FFT was also applied to the velocity traces after the ensemble averaging and the frequency–amplitude plots obtained by these two approaches were found to be identical and thus the FFT can be applied to either individual velocity traces which are then ensemble–averaged or directly to ensemble–averaged velocity traces, i.e. the sequence does not make any difference. Eventually, all frequency–amplitude plots obtained at different Reynolds numbers were plotted together in 3–D frequency field plots. These 3–D frequency field figures indicate the most commonly existing frequencies and their amplitude and thus any periodic flow structures can be visualized. This enables us to distinguish the exact number of stationary vortices in the boundary layer.

6.6.1 Frequency Spectra over Smooth Disks

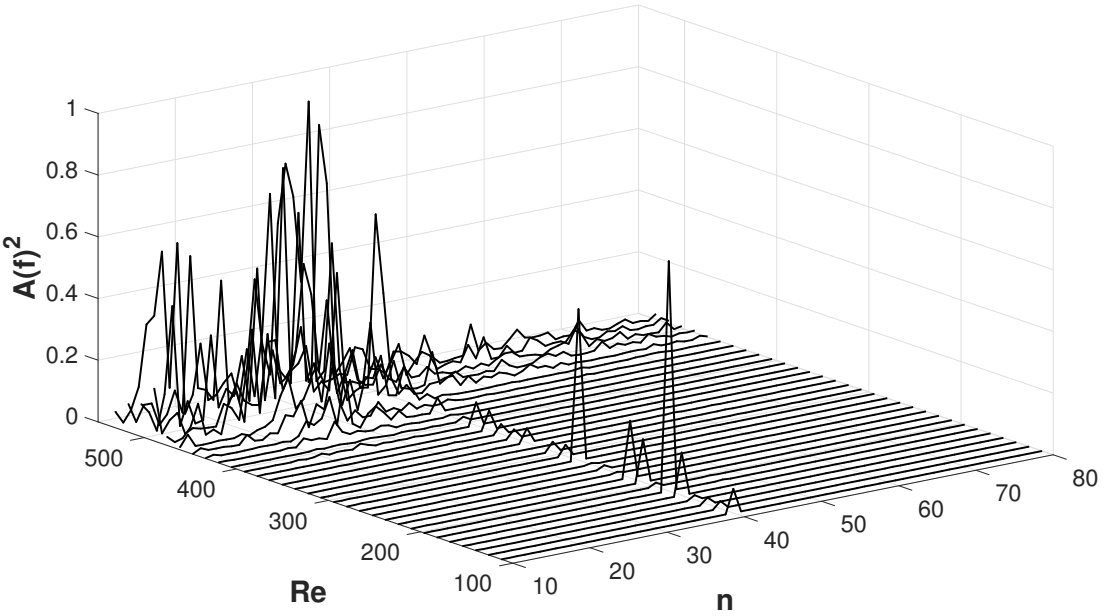

Figure 6.20: Three dimensional view of the Fourier energy spectrum. The data were collected over the smooth disk at $\zeta = 1.3$ and $\Omega^* = 7.85$ rad/s.

Figure 6.20 shows the frequency field for the smooth disk rotating at $\Omega^* = 7.85$ rad/s. Each line in the figure illustrates the frequency–amplitude plots at the radial positions varying from $r = 0.04$ m to $r = 0.19$ m with 0.005 m increments which correspond to the Reynolds numbers varying from $Re = 112$ to $Re = 531$ with increments of $Re = 14$. The non–dimensional frequency n was obtained by dividing the physical frequency f by the frequency of the disk f_D which is 1.25 rev/s for these measurements. This method was previously used by Colley et al. (1999) and employed in the current study to show the disturbances per disk rotation rather than disturbances per second. Therefore, any peak in the frequency domain illustrates directly the number of disturbances in the flow for a single rotation of the disk. The z–axis of the plot represents the non–dimensional energy content of the flow $A(f)^2$ which is the square of the amplitude of the Fourier spectra (Press et al., 1992, p. 549). Consideration of this data in terms of the energy content is useful to produce the experimental neutral stability curves which are addressed in Section 6.8. The data were normalized against the maximum value of the energy content in the flow and thus the z–axis varies from 0 to 1. Furthermore, the frequency domain only shows the values of $n \geq 10$ to eliminate the lower frequency noise. A similar range of frequency domain was used, for instance, in Colley et al. (1999, 2006).

The first obvious observation from Figure 6.20 is the peaks in the frequency domain appearing at $n = 40$ at every Reynolds number. It is believed that the mains frequency of 50 Hz which was normalized against the disk frequency of $f_D = 1.25$ Hz causes these peaks at $n = 40$. This mains frequency peak was also observed by Harris (2013, p. 90) who used the same experimental facility but a different anemometry system. Although the changes in the amplitude of this mains frequency at different Reynolds numbers cannot be explained by any physical reason, it was not filtered out and left in the frequency domain since in the opposite case there is a risk of loosing any flow structures appearing at $n = 40$. Nevertheless, the reason of these peaks at $n = 40$ is known, hence they

can be ignored while analysing these plots.

Apart from these peaks, Figure 6.20 shows the most disturbed frequencies start to appear at approximately $Re = 400$ and grows in energy with an increase in Reynolds number. The broadband spectrum at Reynolds numbers of approximately $490 \lesssim Re$ indicates a fully turbulent flow region. Moreover, many disturbances seem to appear in the range of $10 < n < 60$ per disk rotation. The location, where the peaks in the frequency domain are centred, should indicate the number of stationary vortices in the flow field. However, it might be hard to pick this location out from Figure 6.20 and thus the same data is illustrated in a contour plot shown in Figure 6.21.

6.6.1.1 Contour Plots of Frequency Spectra

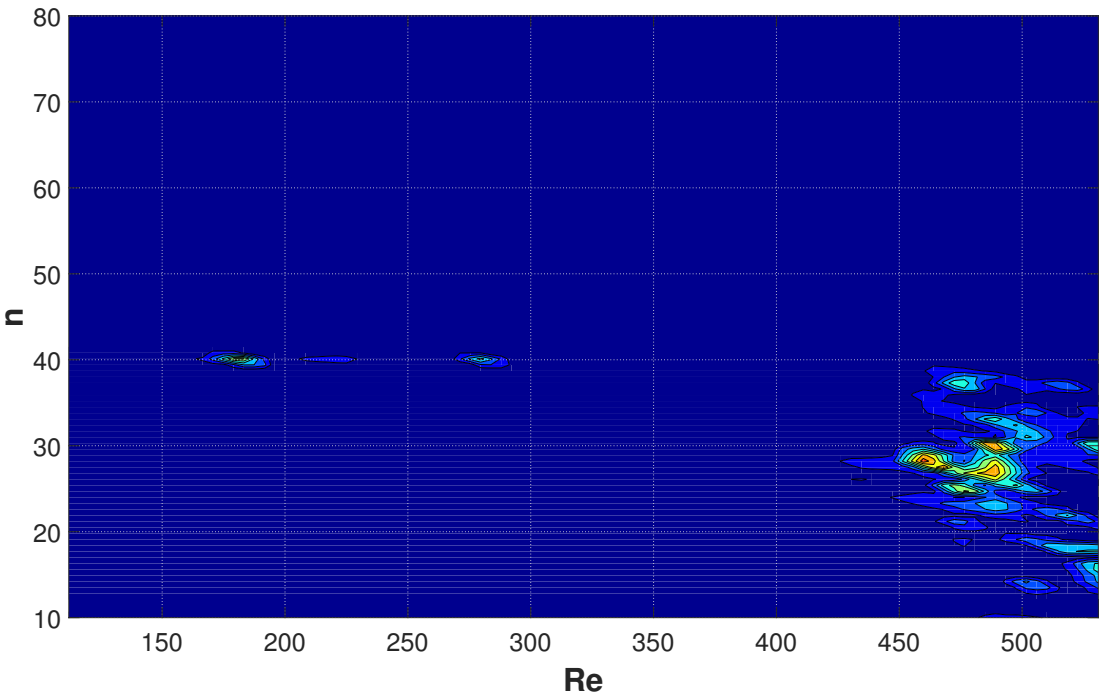

Figure 6.21: The contour plot of the Fourier energy spectrum. The data were collected over the smooth disk at $\zeta = 1.3$ and $\Omega^* = 7.85$ rad/s.

In Figure 6.21, blue colour represents the minimum value of non–dimensional energy content of the flow $A(f)^2$ and red colour indicates the maximum value of the same quantity. Therefore, the coloured area outside the blue area is the in-

dication of disturbances in the flow field. Thus, in Figure 6.21 the vortex peak appears markedly at approximately $n \cong 28 - 29$ and at the Reynolds number of around $Re \cong 455$. This is almost equal to the number of vortices observed in Figure 6.14 for the same smooth disk. By means of this distinct illustration of vortex peak on contour plots, the number of vortices for all test disks were acquired and the results are presented in Section 6.7.

Moreover, in Figure 6.21, the peaks at $n = 40$ and at the Reynolds numbers of approximately $Re = 180$ and $Re = 280$ can be ignored since they represent the mains frequency which was also observed previously in Figure 6.20.

Figure 6.21, however, does not show the broadband disturbances appearing in Figure 6.20 above $Re = 480$. It may be due to the dominance of the maximum value of $A(f)^2$ suppress these relatively small disturbances on the contour plot. Nevertheless, this is not important in the context of our investigation of the vortex peak from these contour plots.

Figure 6.21 has also been produced on a logarithmic scale to try to capture structures at earlier stages of their growth but this approach did not provide any additional benefits and thus all contour plots in the current study are produced on a linear scale. An example of a contour plot produced on a logarithmic scale can be seen in Figure 7.1 in the Appendix.

6.6.2 Frequency Spectra over Concentric–Grooved Disks

The effect of the surface roughness on the Fourier energy spectra can be seen, for instance, in Figure 6.22. This plot shows the spectra for the disk with distributed concentric grooves which has the groove depth of $A = 0.15$ μm and the groove width of $B = 1.5$ μm and thus the roughness ratio of $a = 0.1$. Firstly, in comparison with the smooth disk (*c.f.* Figure 6.20), the roughness seems to trigger the transition earlier where the disturbances start to appear at approximately $Re = 300$ and then grow in energy towards the edge of the disk. The peaks

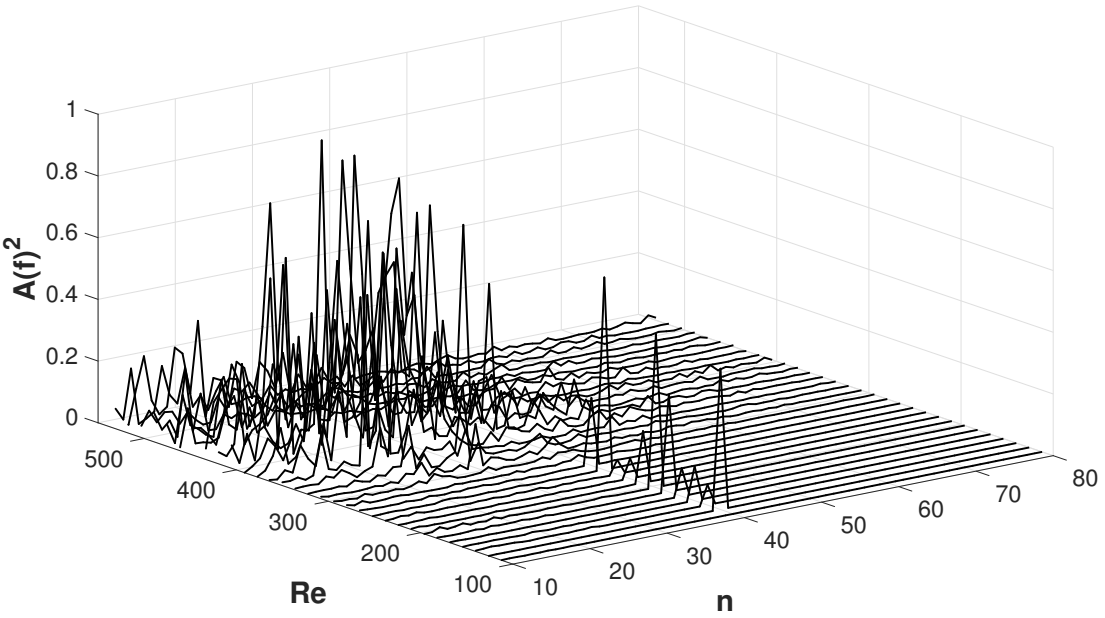

Figure 6.22: Three dimensional view of the Fourier energy spectrum. The data were collected over the concentric–grooved disk with $A = 0.15$ μm, $B = 1.5$ μm, $a = 0.1$ at $\zeta = 1.3$ and $\Omega^* = 7.85$ rad/s.

raising from the mains frequency at $n = 40$ can also be seen in this figure and as well as in every corresponding figures produced for all disks. It is, therefore, confirmed that this is due to the mains frequency and unavoidable.

6.6.2.1 Contour Plots of Frequency Spectra

Figure 6.23 shows the Fourier energy spectra on a contour plot for the same disk with a roughness ratio of $a = 0.1$. It is clearly seen that the vortex peek appears at around $n = 21 - 22$ and at an earlier Reynolds number of approximately $Re = 350$ than the smooth disk which is $Re = 455$. The number of stationary vortices is evidently decreased with the effect of distributed surface roughness, however, an overall conclusion and the results for all disks are provided in Section 6.7.

6.6.3 Frequency Spectra over Single–Grooved Disks

The Fourier energy spectra for the single–grooved disks were also produced and are shown in Figure 6.24 for the groove depth of $A = 1$ mm and in Figure 6.25

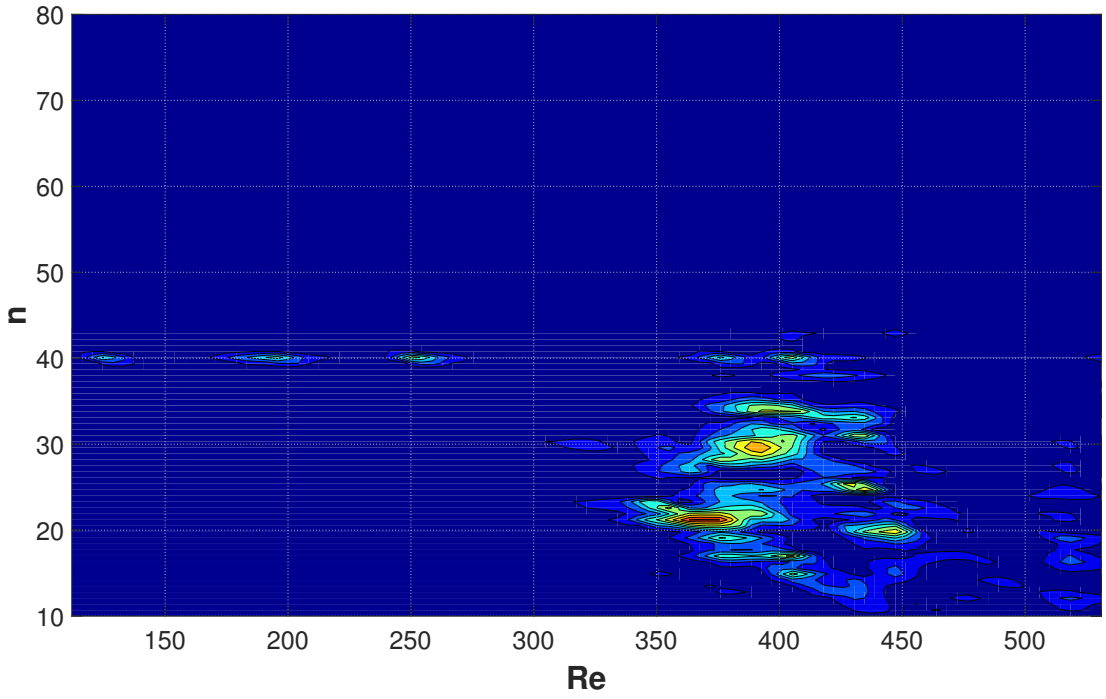

Figure 6.23: The contour plot of Fourier energy spectra. The data were collected over the concentric–grooved disk with $A = 0.15$ μm, $B = 1.5$ μm, $a = 0.1$ at $\zeta = 1.3$ and $\Omega^* = 7.85$ rad/s.

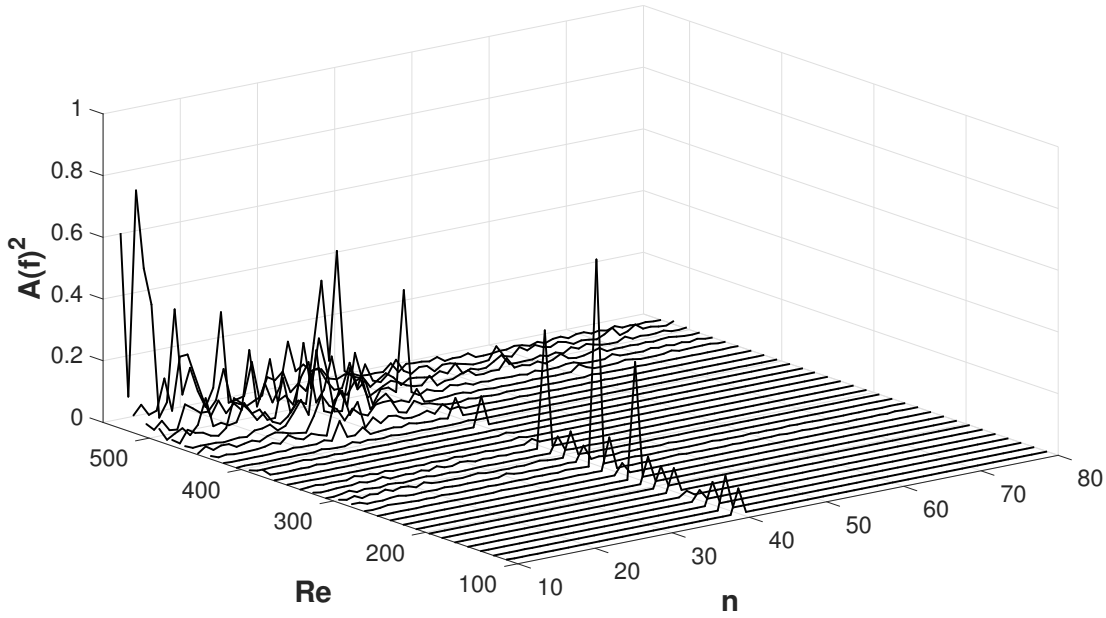

Figure 6.24: Three dimensional view of the Fourier energy spectrum. The data were collected over the single–grooved disk with $A = 1$ mm at $\zeta = 1.3$ and $\Omega^* = 7.85$ rad/s.

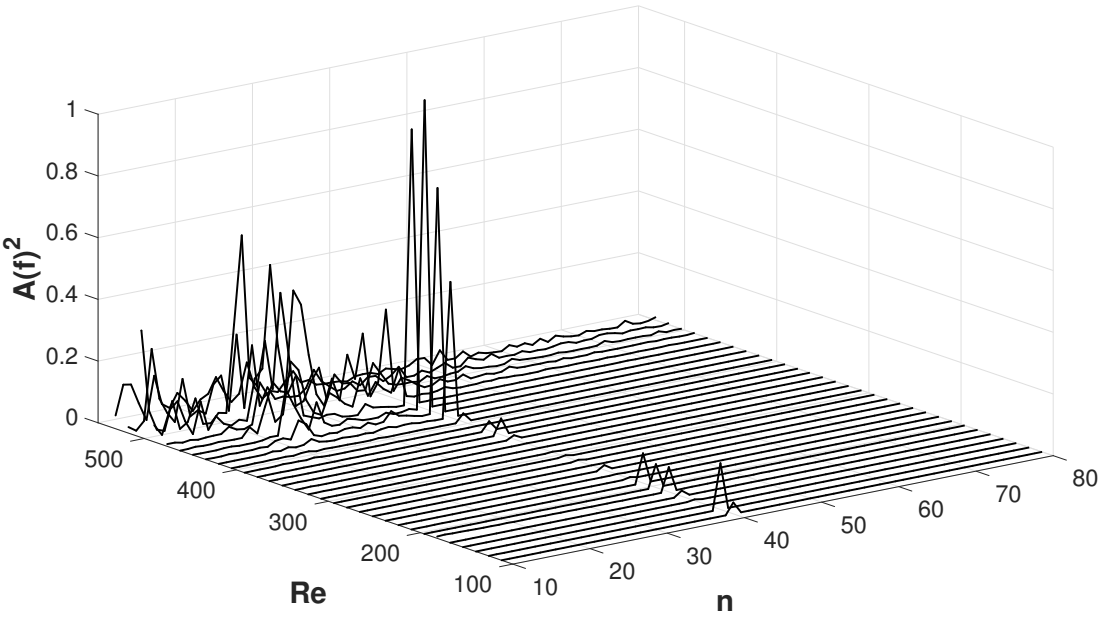

Figure 6.25: Three dimensional view of the Fourier energy spectrum. The data were collected over the single–grooved disk with $A = 0.5$ mm at $\zeta = 1.3$ and $\Omega^* = 7.85$ rad/s.

for the groove depth of $A = 0.5$ mm. Figure 6.24 shows no significant changes from Figure 6.20 that is for the smooth disk apart from small disturbances appearing at approximately $Re = 294$. This is expected since the circular groove with a depth of $A = 1$ mm is cut in the surface of the disk at the radial location that corresponds to the Reynolds number of $Re = 252$. However, these disturbances does not grow in energy towards the edge of the disk and dies out after around $Re = 322$. When the depth of the single groove is smaller $A = 0.5$ mm, one cannot even observe the small disturbances result from the single groove in the corresponding region of the Reynolds number $252 < Re < 322$, see Figure 6.25. This means that the disk with a single circular groove, where the groove depth is $A = 0.5$ mm, and the smooth disk behave similarly in the context of the transition from laminar to turbulent process.

6.6.3.1 Contour Plots of Frequency Spectra

However, both of the disks with a single groove on their surfaces demonstrate features that are different from the smooth disk in the corresponding con-

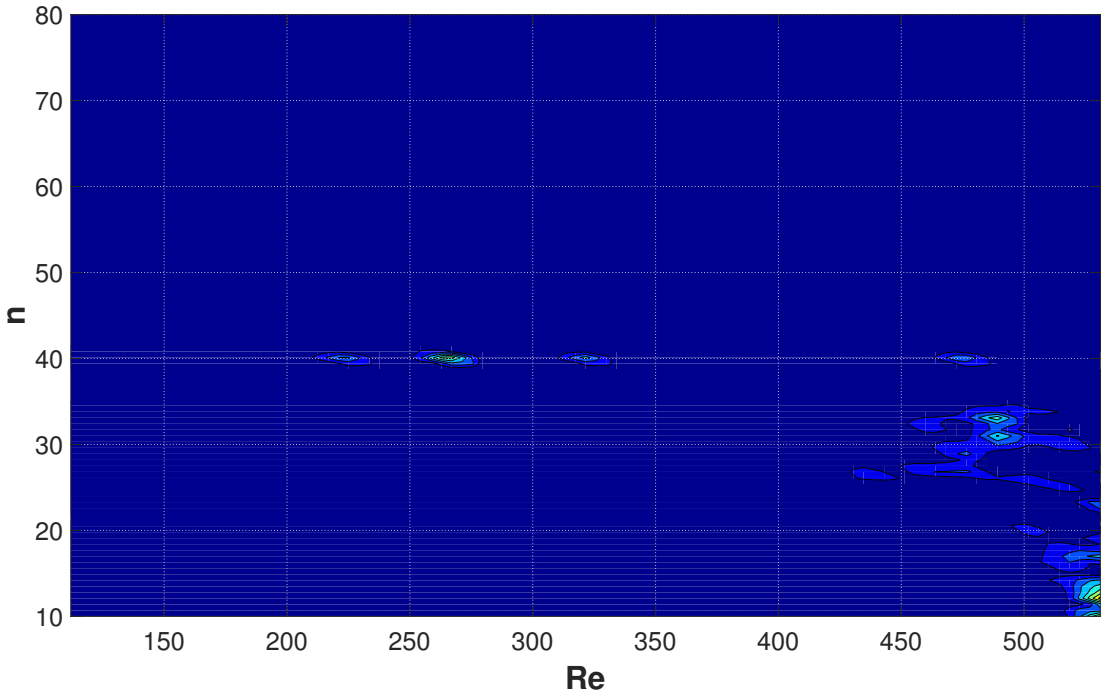

Figure 6.26: The contour plot of the Fourier energy spectrum. The data were collected over the single–grooved disk with $A = 1$ mm at $\zeta = 1.3$ and $\Omega^* = 7.85$ rad/s.

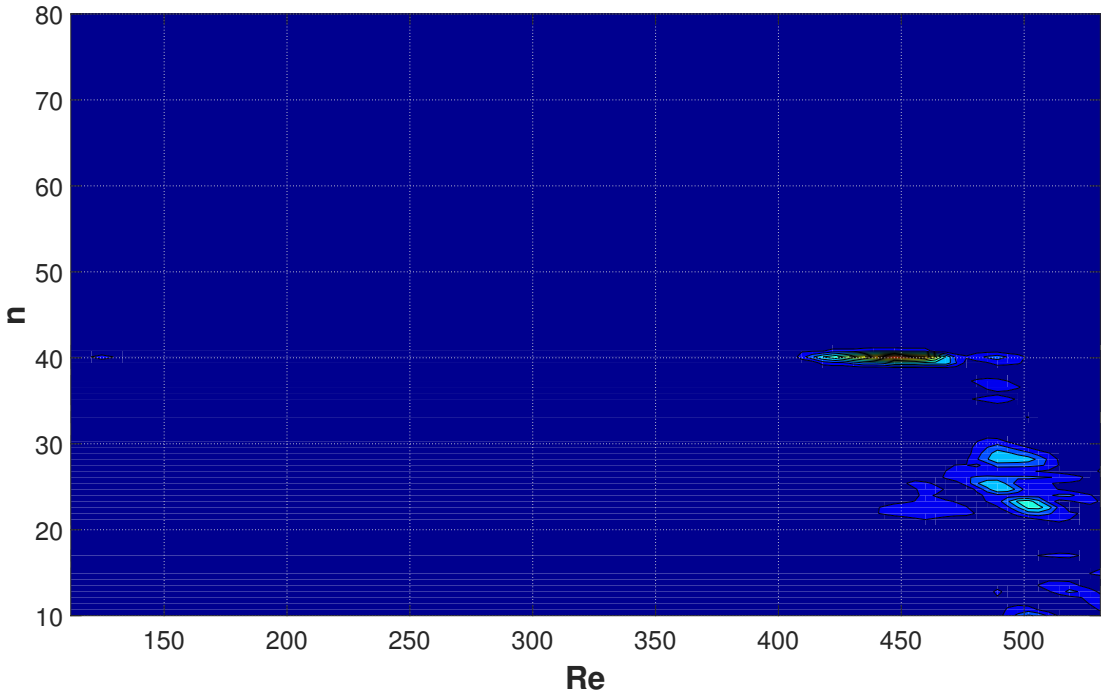

Figure 6.27: The contour plot of the Fourier energy spectrum. The data were collected over the single–grooved disk with $A = 0.5$ mm at $\zeta = 1.3$ and $\Omega^* = 7.85$ rad/s.

tour plots shown in Figure 6.26 for the groove depth of $A = 1$ mm and in Figure 6.27 for the groove depth of $A = 0.5$ mm. Unlike Figure 6.21 for the smooth disk, both of these figures for disks with a single groove show no clear vortex peak. There is a peak in Figure 6.27 at $n = 40$ and at $Re = 450$ but this is due to the mains frequency and needs to be ignored. Nevertheless, the vortex peaks may still be read as $n \approx 28$ in Figure 6.26 and as $n \approx 27$ in Figure 6.27 which are virtually equal to the number of vortices $n \cong 28 - 29$ for the smooth disk.

6.6.4 Fourier Power Spectra

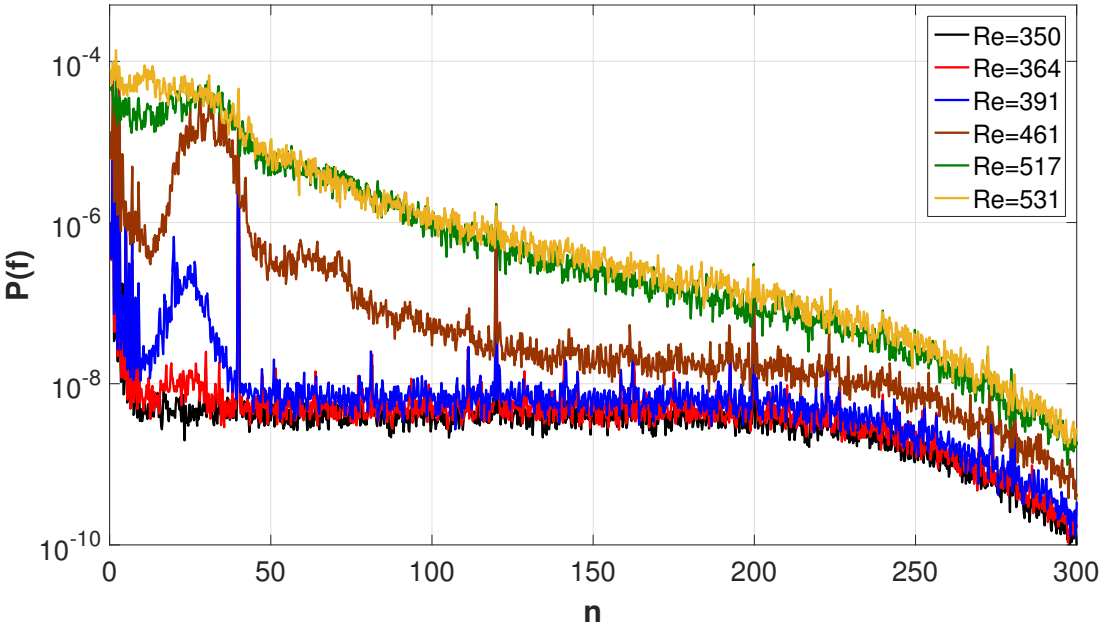

Figure 6.28: Fourier power spectra for ensemble–averaged time series measured over the smooth disk at $\zeta = 1.3$ and $\Omega^* = 7.85$ rad/s.

In addition to the 3–D view of the frequency spectra, it can be useful to show the development of the disturbance spectrum which was obtained over the smooth disk at $\zeta = 1.3$ and $\Omega^* = 7.85$ rad/s for various individual Reynolds numbers to find the exact range of the Reynolds numbers where the stationary vortices appear, in other words to find the transition region. Figure 6.28 shows the power spectral amplitudes $P(f)$ calculated from the ensemble–averaged time series against the non–dimensional quantity $n = f/f_D$. At $Re = 350$ (the black

line), there is no sign of a peak in the signal but at $Re = 364$ (the red line) a broad peak appears with a small amplitude and centred around $n = 30$. This clearly shows that the initial instability occurs somewhere between $Re = 350$ and $Re = 364$. As a reminder, the point of initial instability for the smooth disk was numerically found to be at $Re \approx 287$ (Mack, 1985; Malik, 1986) and at $Re = 290$ (Lingwood, 1995). Experimentally, it was reported to occur in the range of $294 \lesssim Re \lesssim 377$ (Kobayashi et al., 1980; Malik et al., 1981). Therefore, the point of initial instability found in the current experimental investigation is well agreed with the data in literature. Furthermore, the amplitude of the peak grows with Reynolds number and still centred around $n \approx 30$ which indicates the number of stationary vortices and this is also in good agreement with previous observation $n \cong 28 - 29$ in Figure 6.21. At $Re = 517$ (the green line), the peak is still observed but its amplitude is decreased which shows that the stationary vortices has already begun to vanish and the flow is becoming turbulent. At $Re = 531$ (the gold line), the peak totally disappears and the spectrum displays the fully turbulent nature of the boundary layer.

6.7 Vortex number

The number of stationary vortices were acquired using the corresponding contour plots introduced in Section 6.6. Figure 6.29 displays these vortex numbers obtained from the corresponding contour plots for all disks with distributed concentric grooves against their roughness ratio a. Note here that there are 4 disks with the same roughness ratio which is $a = 0.1$ and the vortex number shown in Figure 6.29 for this roughness ratio is the mean value of these 4 disks. The general trend in the figure is that there is a decrease in the number of stationary vortices with an increase in the roughness ratio a. This effect was also mentioned by Cooper et al. (2015) in their theoretical paper with such a comment which is that a concentric–grooved disk tends to reduce the number of stationary vortices

and the current results are the first experimental evidence of their numerical prediction. It is these stationary vortices which represent the Type–I (cross–flow) instability in the flow field and thus from Figure 6.29 it can be concluded that the increased roughness ratio of distributed concentric grooves has a stabilizing effect on Type–I instability.

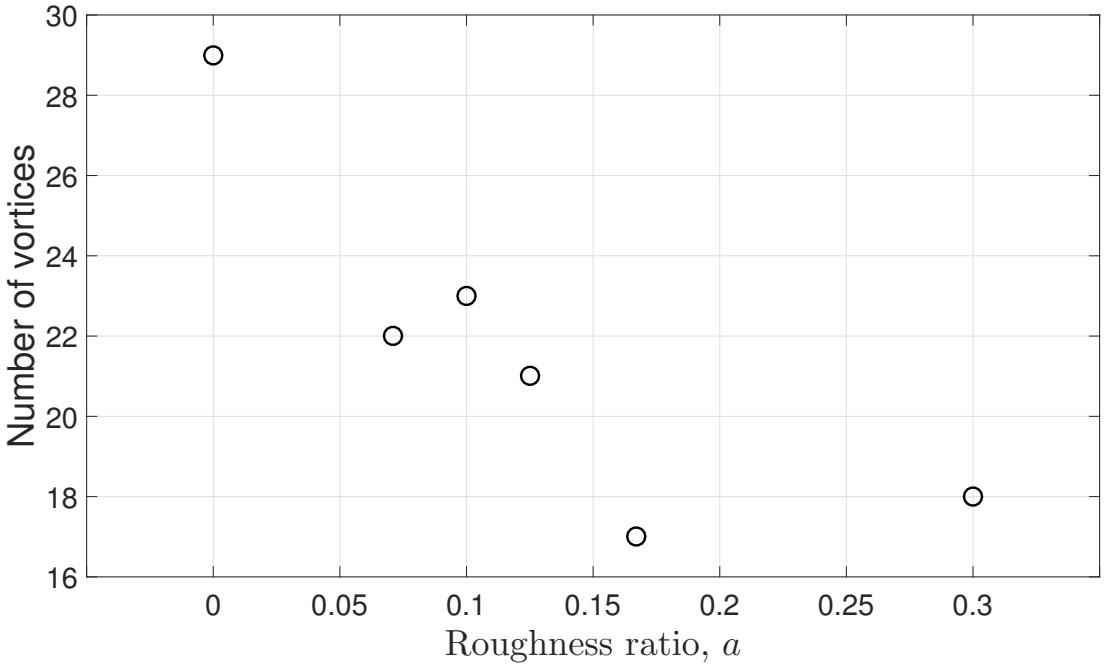

Figure 6.29: The number of vortices acquired from the frequency contour plots which are shown in Section 6.6 against the roughness ratio a.

The detailed investigation of Figure 6.29 reveals that although there is a general decreasing trend in the number of vortices with an increase in the roughness ratio, some of the cases seem to not follow this trend perfectly. The number of vortices, for instance, for the roughness ratio of $a = 0.071$ is lower than the expectation regarding the trend in the figure. It is expected to be between the number of vortices for the smooth disk and for $a = 0.1$. Moreover, the cases for $a = 0.167$ and/or $a = 0.3$ does not develop a good decreasing trend. Examination of additional figures possibly provides better understanding of the effects of roughness, which is distributed concentric grooves, on the number of stationary vortices and thus on the Type–I instability.

In addition to the change of the number of vortices with the effect of the

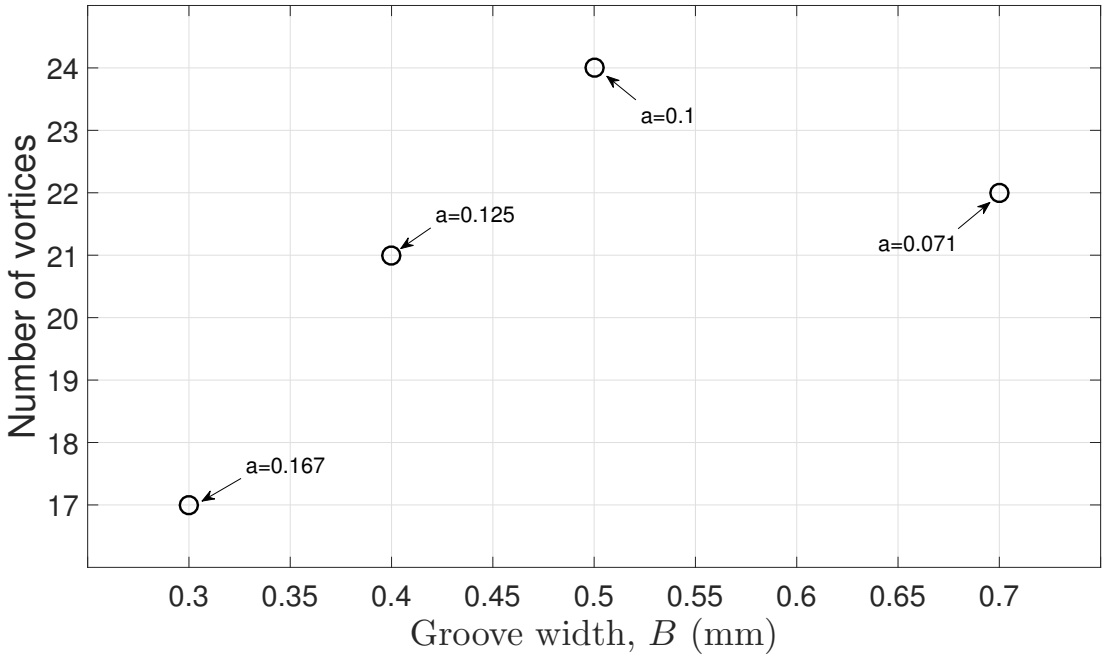

Figure 6.30: The number of vortices against the groove width B in mm where the groove depth A is kept constant at $A = 0.05$ mm.

roughness ratio a, the correlation between the number of vortices and the groove width B is shown in Figure 6.30 where the groove depth A is kept constant at $A = 0.05$ mm. Apart from the data for $B = 0.7$ mm, Figure 6.30 shows a clear increase in the number of vortices with an increase in the groove width B. This result is consistent with the outcome obtained from Figure 6.29 because the increase in the groove width B, when the groove depth A is not changing, means a decrease in the roughness ratio. Therefore, the decline of the roughness ratio results in an increase in the number of vortices as it is concluded from Figure 6.29.

Figure 6.31 may provide additional information about the effects of the distributed concentric grooves on the number of stationary spiral vortices since the data for all disks are included in this figure with their groove depths, widths and so roughness ratios. Furthermore, the x–axis of this plot represents the non–dimensional roughness height which was used previously by Harris (2013) and defined as below.

$$\text{Non-dimensional roughness height} = A\sqrt{\frac{\Omega^*}{\nu^*}} \tag{6.3}$$

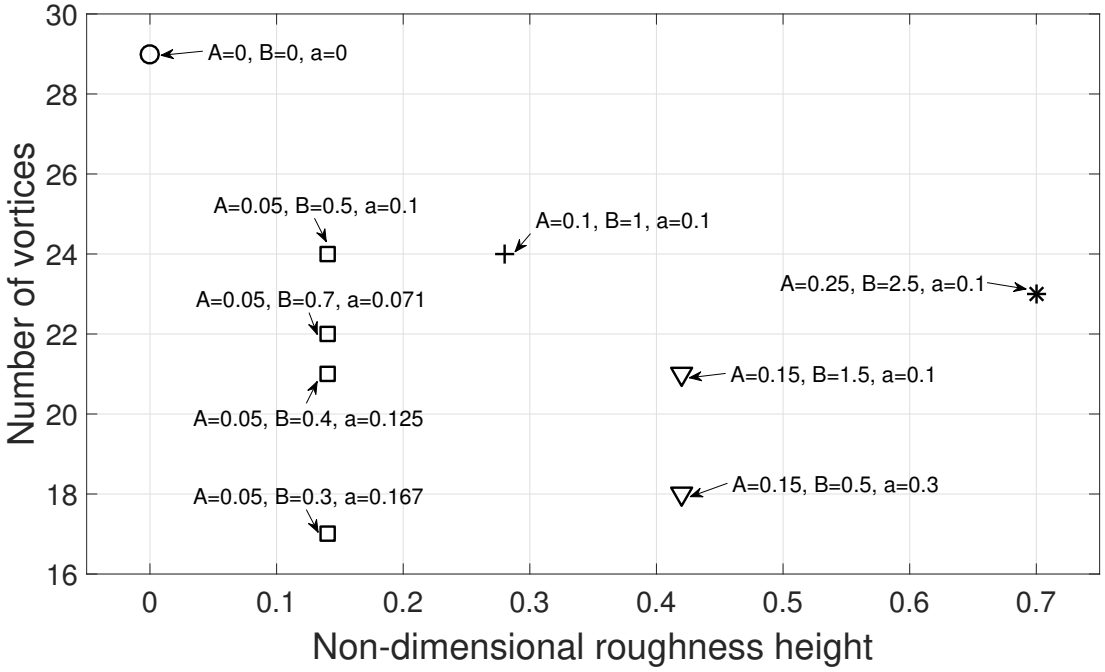

Figure 6.31: The number of vortices against the non–dimensional roughness height, $A\sqrt{\Omega^*/\nu^*}$. The disks with same non–dimensional roughness height are represented with the same symbols.

This was performed by Harris (2013) to include the rotational velocity Ω^* in the roughness parameter since the number of vortices were produced for each of the disks with various rotational velocities and each rotational velocity causes different number of vortices. This makes the comparison plots of the number of vortices with the roughness ratio in Harris (2013) unclear which is not a concern in the current study. Nevertheless, the number of vortices were plotted against the non–dimensional roughness height and illustrated in Figure 6.31 which shows no clear correlation between these two quantities. However, it is still good to display every data in one plot because, for instance, one can see the number of vortices for the disks with the same roughness ratio of $a = 0.1$ can vary from 21 to 24 depending on the geometry of their concentric grooves representing in terms of the groove depth A and the width B.

6.8 Neutral Stability Curves

As it was mentioned previously in Section 6.6, the square of the amplitude of the Fourier spectra represents the energy in the signal. Thus, the Fourier transformed data in Section 6.6 can be reused to produce and observe the energy levels at each frequency for the whole range of Reynolds numbers in the flow field. The energy in the signal can indicate any disturbances appearing in the boundary layer where the data was collected. Note here that the data was acquired at $\zeta = 1.3$ in this study where the boundary layer thickness is equal to $\zeta = 5.5$. The response in the energy can reveal whether a disturbance grow or diminish with an increase or decrease in the Reynolds number at a specific frequency. For instance, if the energy decreases, the disturbance is expected to be weaken and vanish, whereas if the energy increases, the disturbance is expected to be strengthened and thus the instability will grow. Therefore, at a minimum point of an energy plot, the disturbance will neither grow nor vanish, i.e. a minimum point of an energy plot at a specific frequency reveals a critical Reynolds number which is used to form a neutral stability curve.

This approach was previously employed by Jarre et al. (1996a) to produce neutral curves from their experimental data and compare them with the theory. Additionally, the same technique has been used to create neutral curves by Colley et al. (1999) for compliant disks and by Harris (2013) for the rough disks with distributed concentric grooves which were also used in this study. Recalling that the experimental results obtained by Harris (2013) have been reproduced and considerably improved as a part of the current study.

To produce a neutral stability curve, the content of energy at each of the frequencies varies from $f = 12.5$ to $f = 87.5$ Hz were plotted against the Reynolds number varies from $Re = 112$ to $Re = 531$. Figure 6.32 shows, for instance, the amplification diagram for the frequency of 18 Hz for a disk with a single groove on it which has a groove depth of $A = 1$ mm. The data of the energy content in the

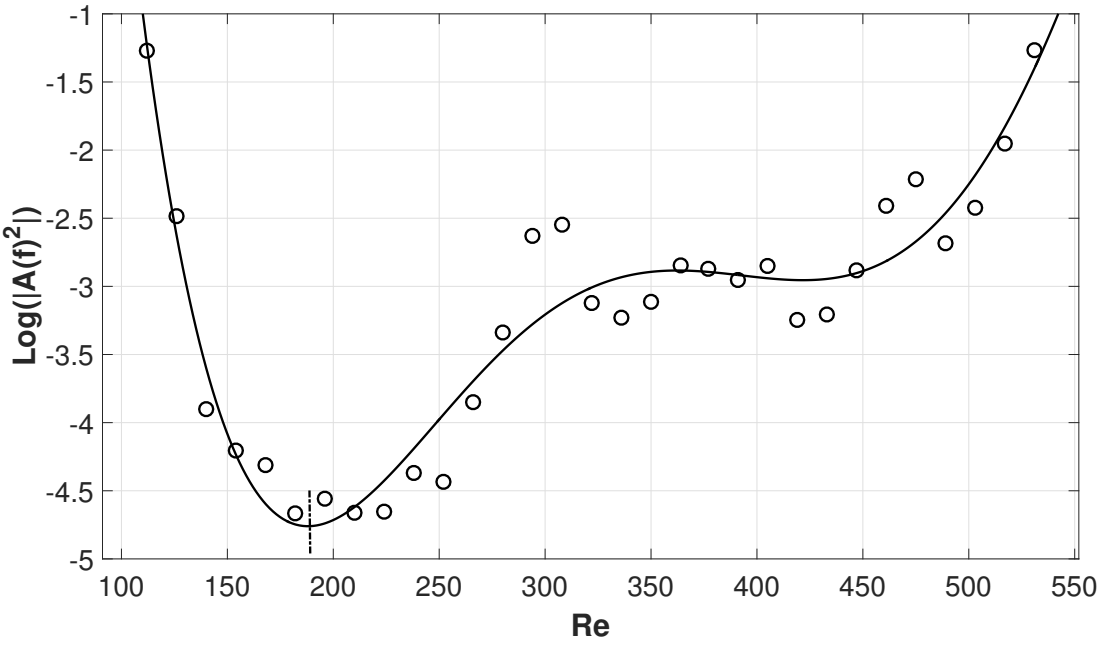

Figure 6.32: Amplification diagram for the frequency of 22.5 Hz for a disk with a single groove which has a depth of $A = 1$ mm. Data was smoothed with a 3–point moving average filter. Vertical line shows the point of minimum energy. Interpolation curve (solid line) is a 5^{th} degree polynomial.

signal (circles) is plotted against the Reynolds number where the y–axis is plotted on a logarithmic scale to make it easy to spot the point of minimum energy. The energy data was smoothed with a 3–point moving average filter and the curve fitted to the data (solid line) is 5^{th}–order polynomial. The vertical dash–dot line indicates the minimum of the curve where the corresponding critical Reynolds number can be obtained.

This method was repeated for each value of the frequency domain illustrated in Section 6.6 and the critical Reynolds numbers were recorded. These critical Reynolds numbers were then plotted against their corresponding frequencies and eventually the neutral stability curves were formed. In the neutral stability curves the frequency axis is represented by the number of disturbances per disk rotation $n = f/f_D$. Therefore, the number of stationary vortices with respect to the rotation of the disk can also be obtained from these figures.

Figure 6.33, for instance, displays the experimental data relating to the neutral stability curve produced for a smooth disk rotating with the rotational

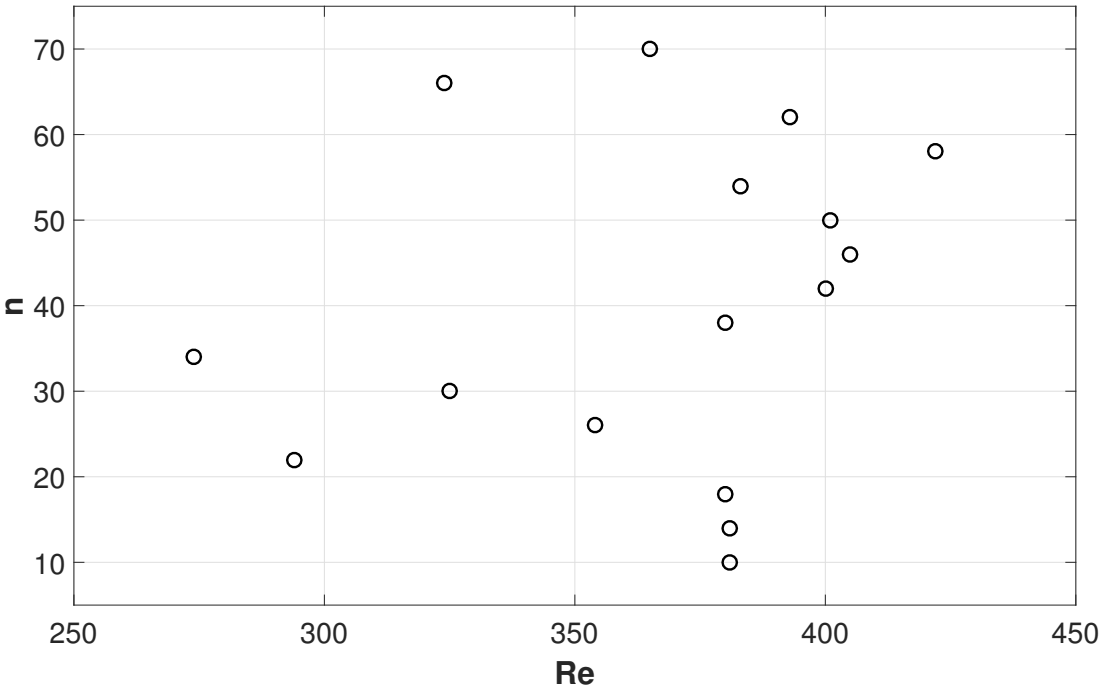

Figure 6.33: Experimental data relating to the neutral stability curve for the smooth disk rotating at $\Omega^* = 7.85$ rad/s.

velocity of $\Omega^* = 7.85$ rad/s. Apart from the two data points at $n = 66$, $Re = 325$ and $n = 70$, $Re = 365$, the data shows a clear peak around $n \approx 25 - 32$ which is reasonable since the previous observations for the smooth disk in Section 6.4 and 6.6 reveal that the number of stationary vortices is around $n \cong 28 - 30$. Additionally, this is in the range of typical values for the rotating–disk flow reported in the literature, see Section 2.6. Additionally, the corresponding critical Reynolds number indicating the region of initial instability falls to a value of approximately $Re = 275$. Values of the critical Reynolds number are, otherwise, centred around at approximately $Re = 370$. This value is around $Re = 375$ in Harris (2013) and $Re = 310$ in Colley et al. (1999). Moreover, it is also in the range of the point of initial instability which was found experimentally as $Re \approx 294 - 377$ by Kobayashi et al. (1980) and Malik et al. (1981).

In addition to considering, only independently, the variation with the Reynolds number for each of the individual mode numbers, two–dimensional fitting was attempted to smooth the data used for construction of the stability curves. However, this attempt did not help to remove the jaggedness observed in

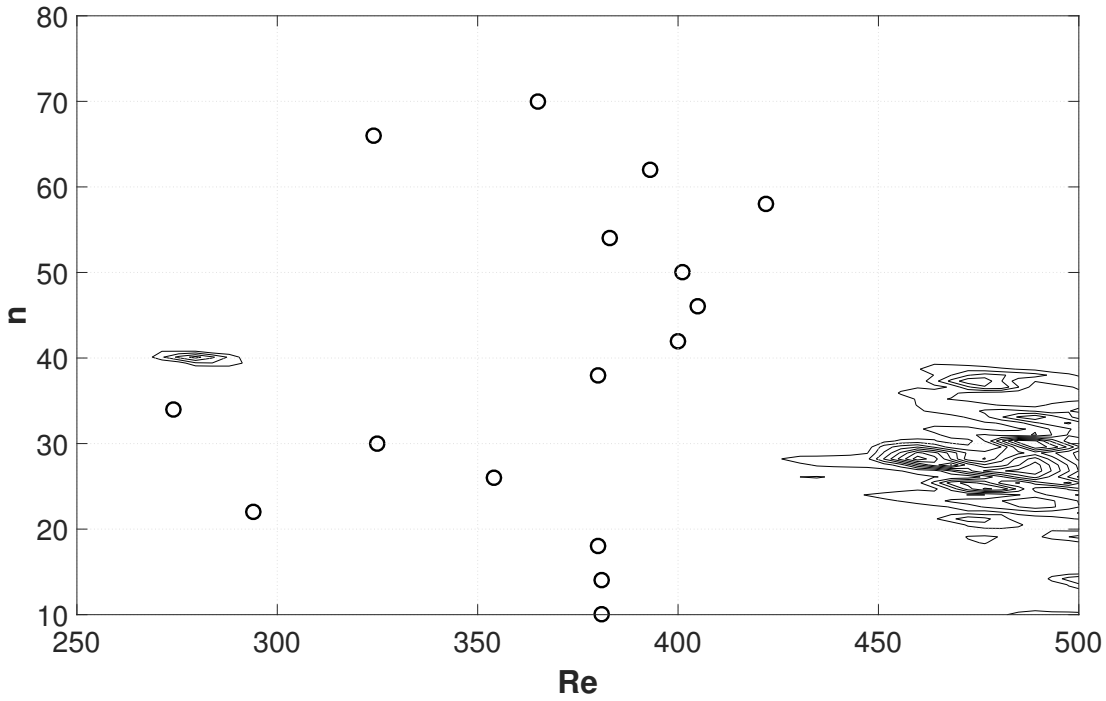

Figure 6.34: Experimentally obtained neutral stability data superimposed on the frequency contour map for the smooth disk rotating at $\Omega^* = 7.85$ rad/s.

Figure 6.33 because it is hard to produce a sufficient 2–D surface function to analyse its minimum points with the existing experimental data. The coefficient of determination, for instance, for the obtained polynomial surface is $R^2 = 0.5828$, see Figure 7.2 in the Appendix.

Figure 6.34, furthermore, superimposes the experimental data relating to the neutral stability curve on the contour plot of frequency field where both of them are for the smooth disk rotating at $\Omega^* = 7.85$ rad/s. The contour plot here is a replica of Figure 6.21, however, it is not filled with colours in this case for the simplicity of Figure 6.34 where the circles denote exactly the same experimental data in Figure 6.33. Nevertheless, the instability region can still be recognized without the use of a filled contour plot and Figure 6.34 can clearly compare the figures produced with two different approaches.

As it was previously mentioned in Section 6.6, the instability region formed in Figure 6.34 at $n = 40$ and in the range of $260 \lesssim Re \lesssim 290$ results from the mains frequency of 50 Hz which cannot be prevented and thus can be ignored. As

a reminder the mains frequency of 50 Hz corresponds to $n = 40$ because $n = f/f_D$ and in this case the disk rotation is $f_D = 1.25$ rev/s.

Apart from this effect results from the mains frequency, there are clear peaks in both the experimental data relating to the neutral curve and the contour plot in the same range of $25 \lesssim n \lesssim 32$. Additionally, according to the points of the neutral curve, the instability region seems to occur earlier than it is indicated by the contour plot. This is probably because the low levels of disturbances are suppressed in the contour plot and thus are not shown. Aside from this, in general, there is a qualitative agreement between the experimental data and the numerical contour plot. This provides validation of the method to experimentally produce these neutral stability curves and therefore they can be used to compare the effects of roughness on the stability region.

6.8.1 Effect of Roughness on Neutral Stability Curves

The experimental data relating to the neutral stability curves produced for all rough disks with distributed concentric grooves are illustrated in Figure 6.35. The figure clearly shows the stabilizing effect of an increased roughness ratio up to a certain limit. For instance, the initial instability occurs at around $Re \cong 280$ for the smooth disk $a = 0$, whereas this value is approximately $Re \cong 460$ for $a = 0.071$, $Re \cong 470$ for $a = 0.125$ and $Re \cong 510$ for $a = 0.167$. However, when the roughness ratio is increased even more to $a = 0.3$, the initial instability falls to a value which is approximately equal to the one for the smooth disk. This outcome implies that there can be a right sort of roughness which can increase the critical Reynolds number for the initial instability and may bypass the transition from laminar to turbulence.

It can also be beneficial to compare our experimental and numerical (obtained from our CFD simulations) results with the numerical solution by Harris (2013). Figure 6.36 illustrates this comparison for the smooth disk case. Black

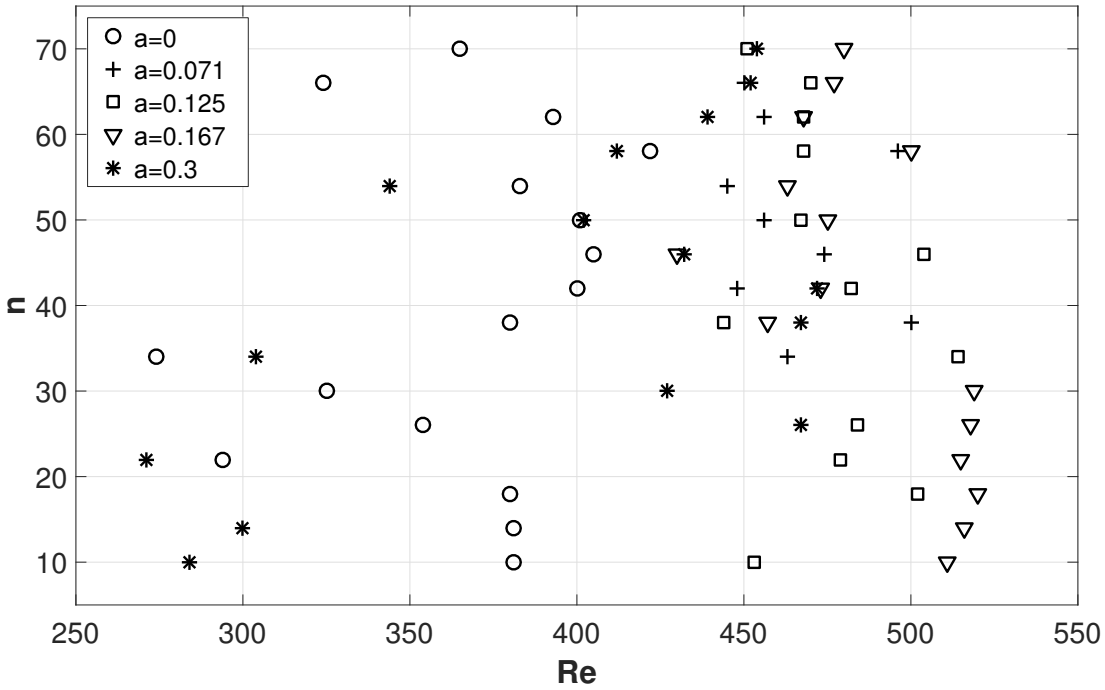

Figure 6.35: Comparison of the experimentally obtained neutral stability data for disks with distributed concentric grooves rotating at $\Omega^* = 7.85$ rad/s.

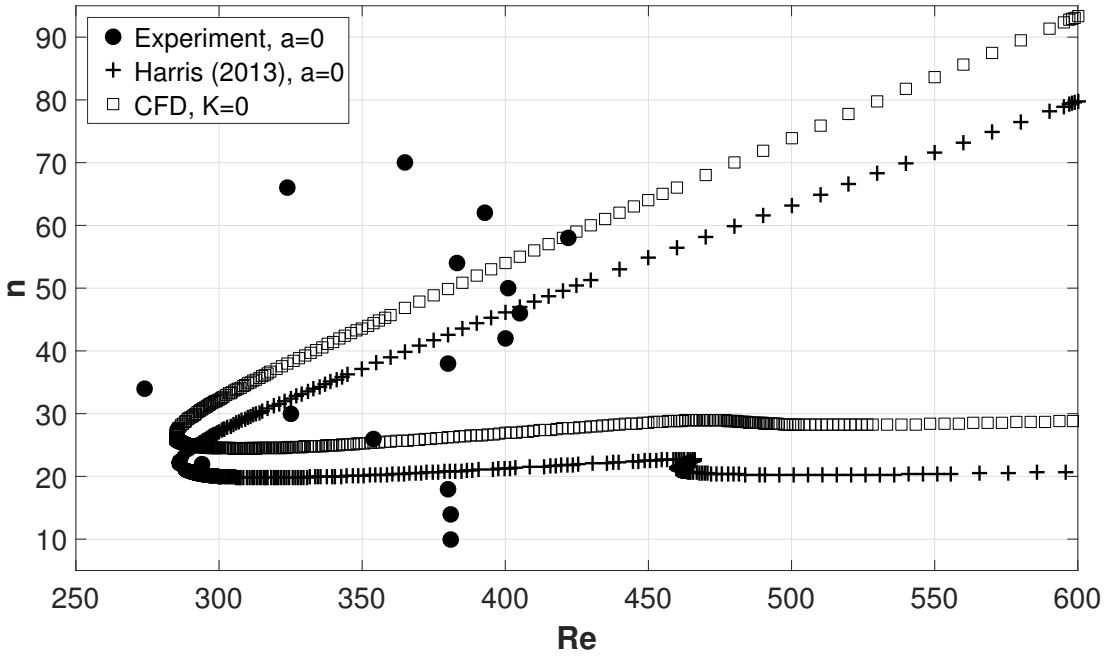

Figure 6.36: Neutral stability data for a smooth disk. Comparison of our numerical (CFD) and experimental data with the numerical results by Harris (2013).

coloured circle markers in this figure represent our experimental data and squares stand for our numerical results produced by our CFD simulations. Plus signs show the numerical solution by Harris (2013) and all of these results are for the smooth disk. Both of the numerical results show a very good qualitative and quantitative agreement apart from a slight difference which is constant for the whole range of the Reynolds number. The onset of the initial instability is same for both numerical approaches at around $Re \cong 280$ which also coincides with our experimental results. Our experimental data, furthermore, shows a clear peak at around $n \cong 20 - 30$ which is also the case for the data obtained by two numerical methods. Figure 6.36, therefore, provides further validation of both our experimental and computational results.

As a reminder, the surface roughness in our CFD simulations was implemented by the modification of the law of the wall according to the geometric roughness height defined in the simulations, refer to Section 3.6 for a detailed explanation. Therefore, our numerical results presented here are in terms of the geometric roughness height K directly, where there are 4 cases $K = 0$, $K = 100$ μm, $K = 300$ μm and $K = 500$ μm. These particular values of geometric roughness heights were chosen since they represent approximately the range of typical roughness heights one would expect to find associated with applications involving drag–reduction techniques in practice. Additionally, these are in the range of roughness heights used in our experiments. The depths of the concentric grooves in our experiments vary from 100 μm to 500 μm, see Table 5.1.

Harris (2013), on the other hand, defined the surface roughness with a sinusoidal function, following the method by Yoon et al. (2007), in his numerical investigations. The surface roughness, thus, can be characterized by the amplitude and the wavelength of this sinusoidal function. In terms of our experiments, they correspond to the depth A and the width B of the concentric grooves, respectively, which are distributed on the surfaces of our rough disks. Therefore, the roughness ratio of these rough disks can be modelled with the technique used

by Harris (2013) for a direct comparison. However, it should be reminded that neither the amplitude nor the wavelength of this sinusoidal function used for modelling the surface roughness individually correspond to any physical dimensions of roughness. Therefore, they can only be compared in terms of the roughness ratio which is impossible to be defined in our numerical simulations since we used real roughness heights. Apart from the smooth disk case, thus, it is impossible to directly compare our numerical results with those in Harris (2013). Nevertheless, the comparison of these three different approaches that are our experimental and computational results and the numerical results by Harris (2013) might be useful in the context of the investigation of the effects of surface roughness on the flow field.

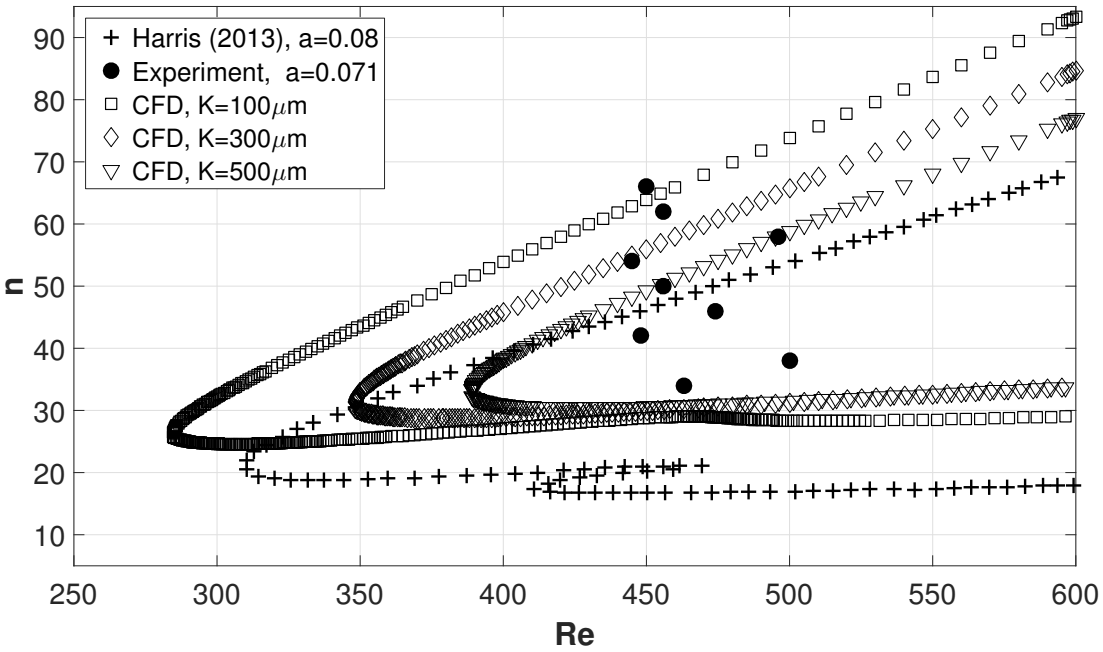

Figure 6.37: Neutral stability data for rough disks. Harris (2013) for $a = 0.08$, Experiments for $a = 0.071$ and CFD simulations for $K = 100$ μm, $K = 300$ μm, $K = 500$ μm.

The numerical data by Harris (2013) shown in the Figure 6.37 and 6.38 for the rough disks with roughness ratios of $a = 0.08$ and $a = 0.16$ were obtained and reproduced from Figure 4.3 in Harris (2013, p. 50). These roughness ratios were chosen from Harris (2013) since they are the only pertinent ones presented in that study which are closest to the values of the roughness ratios of our experimental

rough disks, i.e. one can see the differentiation between Table 5.1 showing the roughness ratios of our rough disks and Figure 4.3 in Harris (2013) showing the available data for comparison. All of the numerical data obtained from our CFD simulations for all of the disks with different roughness heights were included in Figure 6.37 and 6.38 for comparison. This is because of our inability to represent the geometric roughness height used in our CFD simulations in terms of the roughness ratio for a direct comparison with the numerical results by Harris (2013). However, it is beneficial to use the geometric roughness height in our CFD simulations and include the results in these figures for a comparison because it can provide a relation between the theory–based roughness modelling and the real roughness height. This relation can subsequently be useful for the possible practical applications of this theory–based roughness modelling.

The first observation from Figure 6.37 is the stabilizing effect of the increased roughness height in our CFD simulations. The initial instability, for instance, for our CFD simulations for the geometric roughness heights of $K = 100$ μm, $K = 300$ μm and $K = 500$ μm occurs at approximately $Re \cong 280$, $Re \cong 350$ and $Re \cong 390$, respectively. This effect was previously summarized in Chapter 4. In addition to this reminder, there is an overall qualitative agreement between our computational results and the numerical data by Harris (2013). The region of the initial instability for $a = 0.08$ by Harris (2013) appears at approximately $Re \cong 310$ which is between the points of initial stability for the CFD cases of $K = 100$ μm and $K = 300$ μm. This implies that the theory–based surface roughness of $a = 0.08$ may correspond to a real roughness height which varies from 100 μm to 300 μm inasmuch as it is more closer to 100 μm. Additionally, the Type–II instability represented by a lower lobe in the curve by Harris (2013) disappears in our CFD curves for a single temporal frequency. This observation was also mentioned previously in Section 4.5.3 of Chapter 4. The experimental data, moreover, for the rough disk with a roughness ratio of $a = 0.071$ are illustrated in Figure 6.37. Although the roughness ratio of the rough disk investigated

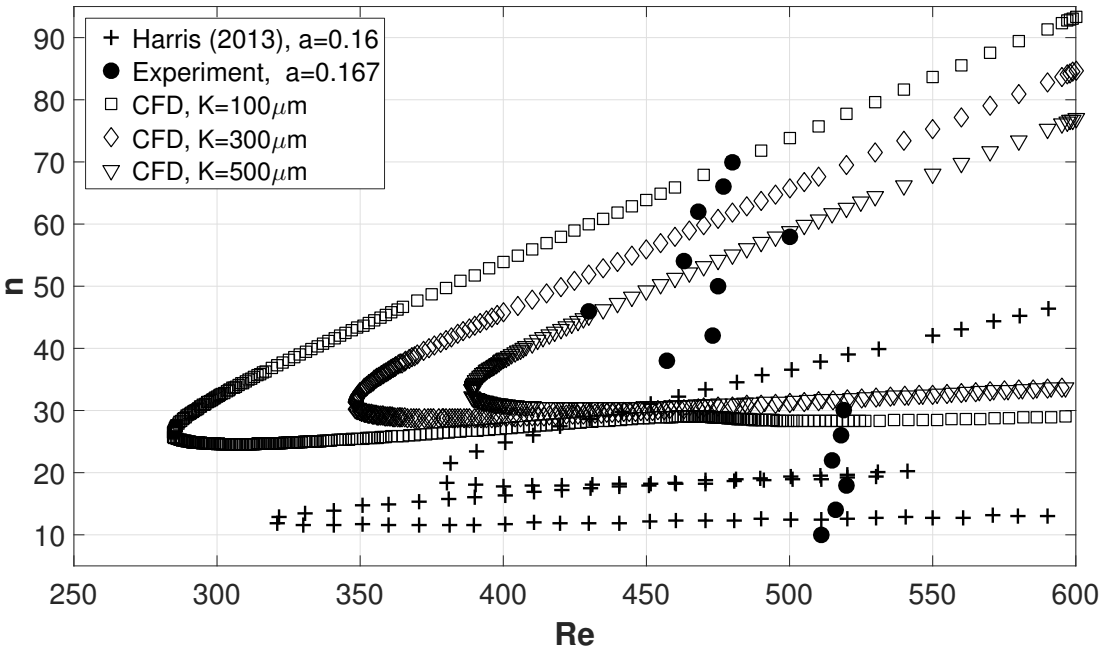

Figure 6.38: Neutral stability data for rough disks. Harris (2013) for $a = 0.16$, Experiments for $a = 0.167$ and CFD simulations for $K = 100$ μm, $K = 300$ μm, $K = 500$ μm.

approximate the value of $a = 0.08$, the experimental data show no similarity with both our CFD simulations and the numerical data by Harris (2013). This may be because of the experimental uncertainties associated only with this rough disk which has the roughness ratio of $a = 0.071$. Previous plots in Section 6.7, Figure 6.29 and 6.30, support this argument since the data associated with this particular disk diverge from the general trend seen in those figures.

Figure 6.38 shows the numerical results by Harris (2013) for the roughness ratio of $a = 0.16$ where our experimental data for the rough disk with a roughness ratio of $a = 0.167$ are also displayed. Additionally, the CFD data shown in this figure are identical to those in Figure 6.37. The Type–II instability is not seen in our CFD data as previously mentioned, whereas in Harris (2013), it seems to be strengthened and in fact outweighed the Type–I instability with an increase in the roughness ratio and it becomes the dominant instability mode. In Harris (2013), the Type–I mode of instability appears at around $Re \cong 380$ which is between the corresponding values of our CFD data for the cases of 300 μm and 500 μm. The Type–II mode, moreover, occurs at approximately $Re \cong 320$ and this is

between the cases of 100 μm and 300 μm. This indicates that the region of the initial instability seen in Harris (2013) for the roughness ratio of $a = 0.16$ may be somehow linked to the geometric roughness height varies from 100 μm to 500 μm. The experimental data for the rough disk with a roughness ratio of $a = 0.167$ are also illustrated in the same figure. This data show a better qualitative agreement with our CFD simulations rather than the numerical results by Harris (2013). For instance, the first five data points starting from the bottom of the figure are at around $Re \cong 510$ and below $n = 30$ where the flow is stable according to our CFD neutral curves, whereas it is unstable according to the curve by Harris (2013). Beyond $n = 30$, there is a peak in our experimental data which also coincides with the peaks appearing at the same region in our CFD curves. Additionally, there are three experimental data points perfectly agreed with our neutral curve for the roughness height of $K = 500$ μm. These are the ones at $Re \cong 430$, $n \cong 47$; $Re \cong 460$, $n \cong 54$ and $Re \cong 500$, $n \cong 58$. Furthermore, there are other experimental data points in the range of $460 \lesssim Re \lesssim 480$ and $62 \lesssim n \lesssim 70$ which are in good agreement with the neutral curves for $K = 100$ μm and $K = 300$ μm. Although the roughness height (the groove depth) of this disk is 100 μm, there is the groove width of 300 μm as well, see Table 5.1, which changes the characteristics of the surface roughness. Therefore, a direct comparison between the experimental data and the CFD results is not quite straightforward. However, as a result of the above mentioned similarities, it may be possible to find a relation between the geometric roughness height used in the CFD simulations and the wavy surface roughness of the rough disk with the roughness ratio of $a = 0.167$.

6.9 PDF Contour Maps

A probability density function (PDF) is a function of an arbitrary continuous variable, whose integral over an interval provides the probability that

the value of this variable is found inside the same interval. The use of the PDF contour plots as a means of a graphical representation of the transition characteristics of a rotating–disk boundary–layer flow was introduced by Imayama et al. (2012). Following their study which is based on an air–based rotating–disk facility, we have produced the relevant PDF contour plots for the experimental data acquired from our water–based facility. The rationale behind the production of these PDF plots is twofold: trying to reproduce the results of Imayama et al. (2012) to support this study with an alternative experimental rig and observing the effects of surface roughness, if possible, with this new way of describing transition characteristics.

The data used for plotting PDF contour maps were acquired at the vertical location of $\zeta = 1.3$ over the disks rotating with a constant rotational speed of $\Omega^* = 12.57$ rad/s which corresponds to 2 rev/s. There were 1000 data points obtained per disk revolution during a 30 s sampling time which provides 60 rotations in total. The data were then ensemble averaged as it was performed previously to obtain velocity field illustrated in Section 6.4. The ensemble averaged data can then be converted into the corresponding velocity magnitudes because the hot–film probe was calibrated for every data collection. This has been the crucial improvement to the existing rotating–disk facility which has been in use for many years (Colley, 1997; Colley et al., 1999, 2006; Harris, 2013). Harris (2013), for instance, produced the PDF contours with an uncalibrated hot–film probe and visualized valuable features of the flow. However, those contour plots produced with an uncalibrated probe were not appropriate to be compared directly with the ones in Imayama et al. (2012).

The calibrated hot–film probe, in the current study, allows us to convert the raw voltage data into the velocity magnitudes which are the azimuthal components of the boundary layer flow at the radial locations vary from $r^* = 0.057$ m to $r^* = 0.192$ m corresponding to the range of Reynolds numbers from $Re = 201$ to $Re = 679$. This range of Reynolds number is very similar to the one used

in Imayama et al. (2012) and makes it appropriate for a direct comparison. The radial location, in their study, varies from $r^* = 0.116$ m to $r^* = 0.226$ m which corresponds to the range of the Reynolds number varies from $Re = 360$ to $Re = 700$. Note here that the constant rotational speed in their study is $\Omega^* = 1400$ rpm and the radius of the disk is 0.237 m.

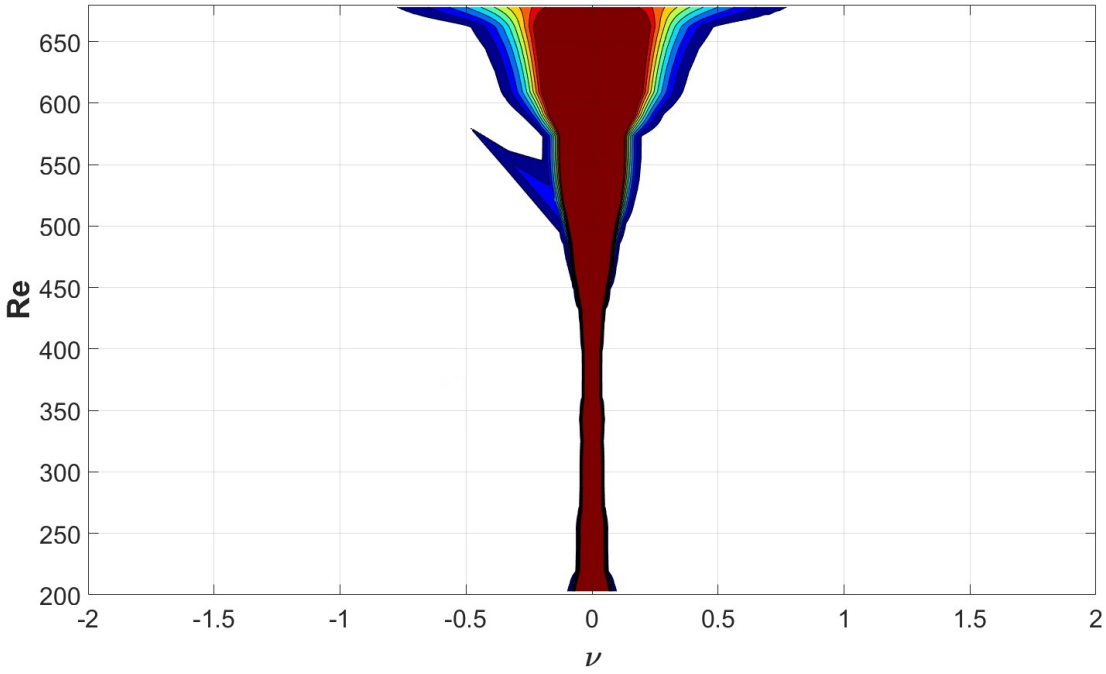

Figure 6.39: The PDF of the instantaneous azimuthal fluctuation velocity v at $\zeta = 1.3$ normalized by the corresponding wall speed. For the smooth disk rotating at $\Omega^* = 12.57$ rad/s. Filled contours indicate 10%, 20%, 30%, 40%, 50%, 60%, 70%, 80%, 90% of the local PDF value.

Figure 6.39 shows the contour plot produced for the smooth disk rotating with a constant rotational speed of $\Omega^* = 12.57$ rad/s which correspond to 2 rev/s. The raw voltage data for the azimuthal fluctuation velocity were acquired at $\zeta = 1.3$. The ensemble averaged velocity magnitudes obtained from these voltage readings, as mentioned above, were then normalized by the corresponding wall speed which is expressed as $\Omega^* r^*$. This allows us to capture the skewed structures seen in Figure 2.10 taken from Imayama et al. (2012), whereas these formations are not observed in Harris (2013), see for instance Figure 6.35 in that study.

The probabilities indicated by the filled colours are provided in the caption of Figure 6.39. For instance, the probability of the instantaneous azimuthal

fluctuation velocity in the dark red coloured area is 90% and it reduces down to 10% when the tone of the colour moves towards blue. It can be seen from the figure that the PDF is narrow and constant up to the Reynolds number of approximately $Re \cong 430$ which suggests a laminar flow regime in this domain. Starting from the Reynolds number of $Re \cong 430$, the width of the PDF starts to increase slightly until the Reynolds number of approximately $Re \cong 575$. This increase in the width of the PDF and a strongly skewed structure appeared between $Re = 500$ and $Re = 575$ indicate the transition region from laminar to turbulent flow. Beyond $Re = 575$, the skewed structure disappears and the deviation of v reaches its maximum value which demonstrates the fully turbulent flow regime. The magnitudes on the plot can be directly compared with the ones in Imayama et al. (2012) since these are non–dimensional values. Accordingly, the deviation of v in our plot seems to be bigger than the relevant figure in Imayama et al. (2012) even in the laminar flow regime. Furthermore, the maximum deviation exceeds the range of $-0.5 < v < 0.5$ in our results, whereas it is in the order of approximately $-0.25 < v < 0.25$ in Imayama et al. (2012). Therefore, it can be clearly concluded that the noise levels for our water–based rotating–disk flow is much higher than the air–based rotating–disk flow. Additionally, the deviation seems to be marginally larger than the rest of the laminar flow region at around $Re = 200$ which is not expected. However, this may be explained with the disturbances propagating from the deformation of the free–surface of water in the vicinity of the rotational axis which was pictured previously in Figure 6.10.

6.9.1 Flow Structures Normal to the Disk Surface

This PDF technique is also helpful to visualize the structure of the flow that is normal to the wall. Figure 6.40 illustrates the flow structures form in the vertical direction by means of the PDF method at 7 different Reynolds numbers which are $Re = 200$, $Re = 430$, $Re = 470$, $Re = 510$, $Re = 550$, $Re = 590$, and

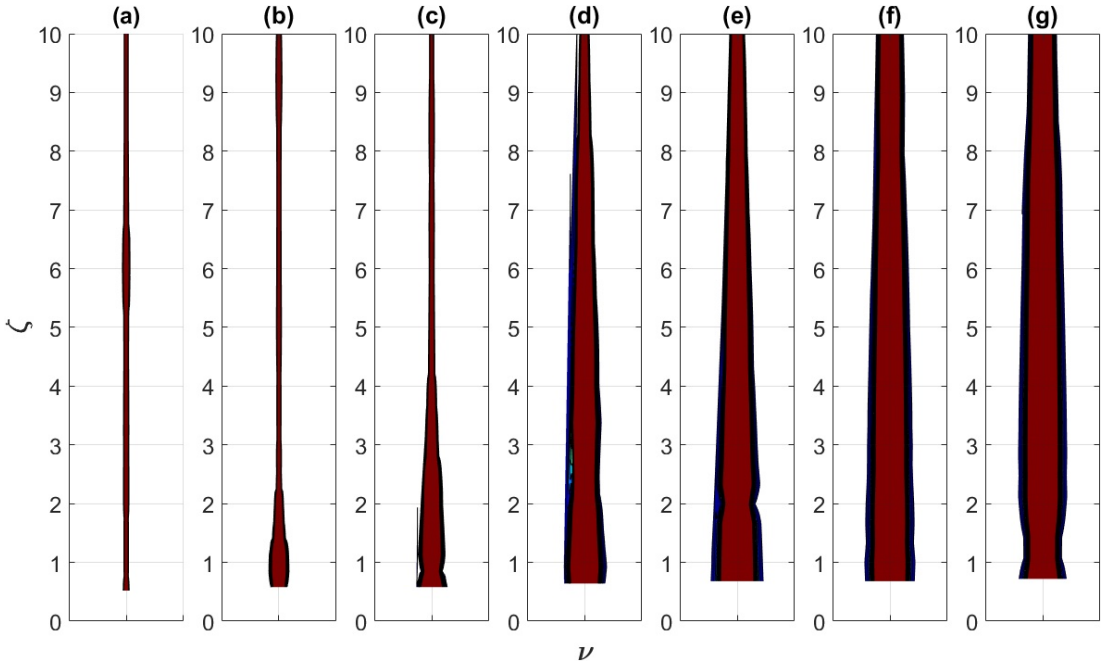

Figure 6.40: The PDF of the instantaneous azimuthal fluctuation velocity normalized by the corresponding wall speed for the smooth disk rotating at $\Omega^* = 12.57$ rad/s. (a) $Re = 200$, (b) $Re = 430$, (c) $Re = 470$, (d) $Re = 510$, (e) $Re = 550$, (f) $Re = 590$, and (g) $Re = 630$. Filled contours indicate same as Figure 6.39. The range of the abscissa is -0.5 to +0.5 for all Re.

$Re = 630$. The gradual increase in the deviation of the azimuthal velocity can clearly be seen with an increase in Reynolds number. The narrow variation seen in Figure 6.40(a) at $Re = 200$, for instance, indicates that the flow is laminar at this Reynolds number. Increasing the Reynolds number to $Re = 430$ and $Re = 470$, in Figure 6.40(b) and 6.40(c) respectively, results in the growth of the variation near the disk surface which then grows towards the $\zeta = 10$. At $Re = 510$ in Figure 6.40(d), there are notable structures appear in the vertical range of $2 < \zeta < 3$ where the similar forms occur at around $\zeta \cong 2$ at $Re = 550$, in Figure 6.40(e). These remarkable formations in the flow field can be a sign of the transition from laminar to turbulent and this statement is also supported by the highly skewed structures observed in Figure 6.39 at the similar Reynolds number range of $500 \lesssim Re \lesssim 575$. When the Reynolds number is increased to the values of $Re = 590$ and $Re = 630$, see Figure 6.40(f) and 6.40(g) respectively, the fluctuation of the azimuthal velocity appears to be constant along the vertical

axis and the maximum of the PDF seems to be centred around the mean value. This is the indication that the flow at these Reynolds numbers is fully turbulent (Alfredsson et al., 2011).

6.9.2 Roughness Effect on PDF Contour Maps

The effect of roughness on the boundary–layer flow can also be visualize with the PDF contour map method. Figure 6.41 shows, for instance, the colour contour plot of the PDF for the rough disk with $A = 0.05$ mm and $B = 0.3$ mm which lead to a roughness ratio of $a = 0.167$. This rough disk is chosen since it has the most stabilizing effect on the boundary–layer flow as it was previously revealed from the neutral stability data illustrated in Figure 6.35. Therefore, any differences in the PDF contour plots between the smooth disk and this rough disk are expected to be relatively clear compared to other rough disks. Nonetheless, Figure 6.39 and Figure 6.41 show no significant differences. Some of the apparent alterations are that the highly skewed structure, appearing between $Re \cong 500$ and $Re \cong 550$, seems to be reduced slightly with the application of roughness. Additionally, the sharp increase in the deviation of v above $Re = 650$ observed for the smooth disk disappears for this rough disk and instead the deviation grows gradually starting from approximately $Re = 575$. On the other hand, the gradual increase in the deviation of v after around $Re = 435$ for the smooth disk vanishes for the rough disk and instead the increase in the deviation becomes sharp. Apart from these small differences, these two PDF contour plots for two different cases seem to be identical and thus any benefits of the use of this method for the investigation of the surface–roughness effects on the boundary–layer flows cannot be found.

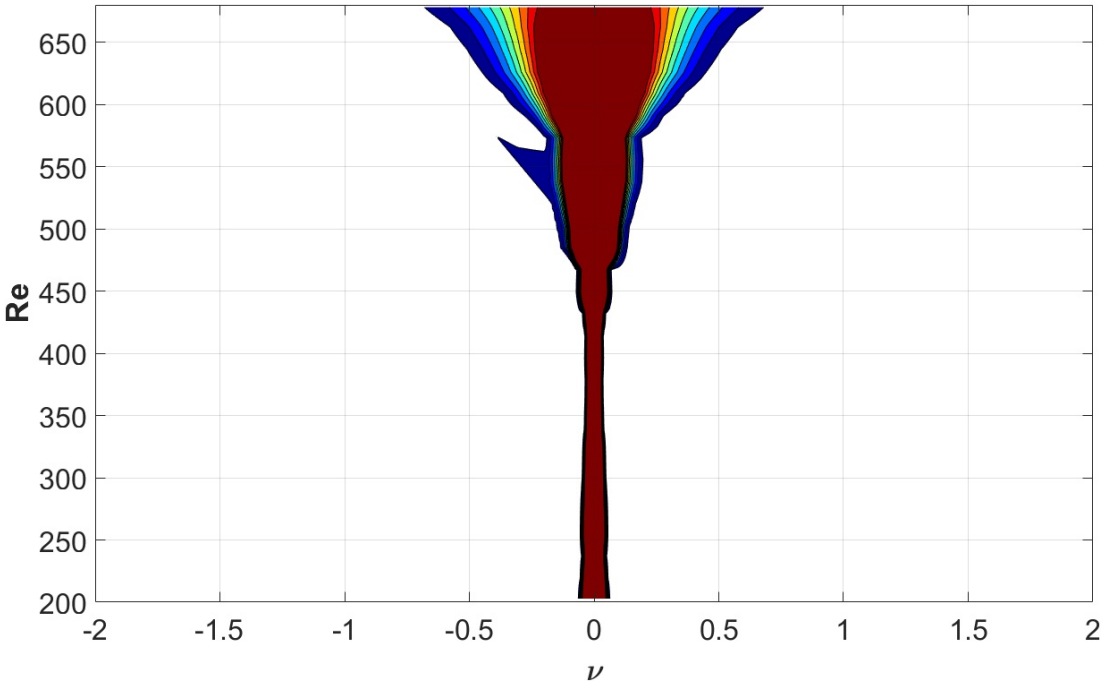

Figure 6.41: The PDF of the instantaneous azimuthal fluctuation velocity v at $\zeta = 1.3$ normalized by the corresponding wall speed. For the rough disk ($A = 0.05$ mm, $B = 0.3$ mm and $a = 0.167$) rotating at $\Omega^* = 12.57$ rad/s. Filled contours indicate same as Figure 6.39.

Chapter 7

Summary and Conclusion

The research summarized in this thesis investigated the effects of the distributed surface roughness and the finite–size of the flow configuration on the three–dimensional boundary–layer flows over rotating disks. The study comprised experimental as well as computational research.

The experimental investigation of the effects of surface roughness were carried out in a rotating–disk facility that consists of a water tank and thus the fluid domain over the rotating disk is restricted. This finite size of the facility results in a modification of the theoretically predicted rotating–disk boundary–layer flow which was obtained by the similarity solution of Kármán (1921). The first evidence of the undesired finite–size effects were previously suggested in (Colley et al., 1999, 2006; Harris, 2013), however, in the current study, the nature and the magnitude of these effects were investigated in detail for the first time.

This alteration in the boundary–layer flow is significant due to the fact that many theoretical studies, such as Cooper et al. (2015) and Garrett et al. (2016), investigating the effects of surface roughness, are based on the basic boundary–layer flow profiles which are obtained on the basis of the similarity solution of Kármán (1921). It is, therefore, important to numerically reveal, in addition to the experimental investigation, whether the roughness–induced and geometry–induced effects on the rotating–disk boundary–layer flow are distinguishable from one an-

other in order that the experimental results can be compared to the theoretical studies investigating the effects of surface roughness.

Therefore, in the computational part of the current study, the boundary–layer flow on the rotor inside the enclosed cavity of a rotor–stator system was investigated. This rotor–stator flow configuration is analogous to the rotating–disk facility used for the current experimental measurements and, therefore, enables a comparison between the effects arising from the roughness and the finite size of the flow geometry.

This examination was carried out by means of the TSST model within the ANSYS Fluent software package. The numerical results were validated against previous experimental data (Colley et al., 1999, 2006; Sambo, 1983) and computational data (Vaughan, 1986) and evaluated further for consistency in the context of the recent theoretical considerations summarized in Cooper et al. (2015), Garrett et al. (2016) and Alveroglu et al. (2016). A high level of qualitative and quantitative agreement between the current simulations and the existing previous work was found.

Particularly, a good level of agreement between the roughness–induced effects obtained by means of the TSST simulations and the corresponding theoretical results of Cooper et al. (2015) and Garrett et al. (2016) was achieved. This leads to a very significant general conclusion due to the fact that the roughness modelling capability of the TSST approach is based on empirical correlations obtained from many different experimental data in literature, whereas the other two studies model roughness in terms of some very simple theoretical assumption. The fact that all approaches yield results which are, overall, mutually consistent gives confidence in the validity of the qualitative behaviours observed. However, due to the details associated with the methods adopted to model roughness in Cooper et al. (2015) and Garrett et al. (2016), a quantitative agreement between their results and those of the current study is not possible.

It was found, in particular, that the TSST approach reconfirms that rough-

ness is expected to stabilize the Type–I instability mode which is very important in a general context. The Type–I mode is the dominant mode resulting in the laminar–turbulent transition of boundary layers with a cross–flow component, as encountered in similar form, for instance, over highly swept wings of aircraft. Stabilization of the Type–I mode equates to postponed transition and, therewith, to reduced skin–friction drag. Hence, the results of the TSST computations are strongly reassuring in that surface roughness can be used in the context of the development on new passive drag–reduction techniques as suggested by the results of Cooper et al. (2015) and Garrett et al. (2016).

Moreover, the consistency in the comparisons also extended across the different BEK flow scenarios investigated. It was discussed that the rotor–stator flow can be considered as an intermediate state between the von Kármán flow and the Ekman flow. For the case of rotor–stator flow over a smooth disk, a very good quantitative agreement between the neutral stability curve obtained by our TSST simulations and the corresponding curve for the von Kármán flow of Alveroglu et al. (2016) was found. The results only differed in a narrow Reynolds number range where the results for rotor–stator flow revealed the disappearance of the Type–II instability mode for zero frequency. Nevertheless, the disappearance of this mode is also observed by Alveroglu et al. (2016) for the Ekman flow in the same Reynolds number regime. This led to the conclusion that the absence of the Type–II mode for the TSST simulations for zero frequency may arise as a consequence of the non–vanishing fluid rotation in the core of the flow field between the two boundary layers on the rotor and the stator.

Finally, as regards the original motivation and goal of the current numerical study, the results have revealed that the effects induced by changes in the geometric boundary conditions in a rotor–stator facility can be of similar nature and magnitude as the effects induced by roughness. While only one particular system was investigated here the result suggests, nevertheless, that there probably exist other flow configurations – related to the present one or not – where

roughness–induced and geometry–induced effects may compete with each other in a similar manner and where this may have to be taken into consideration in the context of the particular scientific problems studied or the design aspects addressed.

Although the current computational study revealed that the effects of surface roughness on the transition of the rotating–disk boundary–layer flow need to be studied carefully when the flow domain has a finite size, the water–based experimental facility can still be used in order to provide supportive argument for these numerical results. Additionally, these experiments can, nevertheless, give valuable information about the effects of roughness on the boundary–layer transition process since the types of surface roughness employed in this study have not yet been investigated comprehensively in the current type of experimental flow configuration. Harris (2013) investigated the similar sort of roughness parameters to some extent, however, the current results are superior to this previous investigation by means of the recent improvements to the experimental facility.

The types of disks with different surface characteristics used in this study are the smooth glass disks, the aluminium single–grooved disks, and the aluminium distributed concentric–grooved disks. All of these disks were individually placed inside the water–based rotating–disk facility and the experimental data were collected by means of the hot–film measurements.

The agreement between the mean velocity profiles experimentally obtained over the smooth disk and the theoretically predicted rotating–disk flow (Kármán, 1921) is better in comparison with the previous study by Harris (2013) where the corresponding data were obtained by means of the same experimental facility. This improvement has been achieved using a new addition of hot–wire anemometry system to the facility and also a newly introduced rotating–arm calibration technique. This new technique was found to be clearly superior, for this particular water–based experimental facility, to the alternative method which consists of performing the calibration over a smooth disk against the von Kármán flow

profiles. Although this alternative method of calibration over a smooth disk can provide satisfactory results for the air–based rotating–disk facilities (Lingwood, 1996; Imayama et al., 2012) where the boundary–layer flow is not restricted, it cannot be applied correctly for the water–based facilities where the von Kármán flow profiles are modified due to the restricted flow domain and thus the calibration against these modified profiles would be incorrect.

In addition to the improvements mentioned above, a yaw–angle bias has also been addressed in the current study. This present yaw–angle correction, furthermore, enhances the current experimental results in comparison with the previous studies (Colley et al., 1999, 2006; Harris, 2013) which did not address this issue since in the context of their study this was not essential.

Moreover, the velocity profiles obtained over the concentric–grooved disks show that an increase in the roughness level results in a decrease in the radial jet flow and this effect is consistent with the current TSST simulations and the previous numerical results by Cooper et al. (2015) and Garrett et al. (2016). The experimental azimuthal flow profiles, additionally, are in good agreement with the TSST results to some extent where the magnitude of the core rotation of the fluid is decreased with an increase in the roughness. Only one set of data (for the case of $K = 500\mu$m) in TSST simulations does not follow this trend. However, the experimental data does not show the thickening of the boundary layer with a increase in the roughness level, whereas this effect was observed in the current TSST data and the two previous numerical studies.

In addition to the individual velocity profiles, the entire flow domain was visualized by means of the velocity traces taken at radial locations through the boundary layer with a very small radial increment which corresponds to a Reynolds number of $Re = 14$. This visualization provides valuable information, for instance, about the transition locations and the number of stationary vortices. However, a better display of the flow was obtained by means of the frequency fields which were produced by taking the Fast Fourier Transform of the velocity traces.

The number of stationary vortices, specifically, were illustrated clearly in the contour plots of these frequency fields. Although there are some exceptions in the data (2 data points out of 6), it seems that the increased roughness level reduces the number of stationary vortices in the rotating–disk boundary layer. These exceptions might result from the experimental error and/or the effects arising from the finite size of the facility. Apart from these exceptions, this outcome is very important since Cooper et al. (2015) numerically showed that the concentric grooves can reduce the number of vortices and this current data can be the first experimental confirmation of their argument.

Furthermore, the experimental data relating to the neutral stability curves were obtained for each disk. These data are in good quantitative agreement with the neutral stability curve produced from TSST simulations for the smooth disk. These current experimental and numerical data are also in very good agreement with the corresponding curve provided by Harris (2013) for the smooth disk by means of a computationally different approach. This high level of consistency gives further confidence in the validity of the TSST approach and the experimental measurements. However, the neutral stability data obtained experimentally over the concentric–grooved disks show no quantitative but qualitative agreement with the current TSST simulations and the numerical data of Harris (2013). Additionally, this experimentally obtained neutral stability data reveal that some of the roughness parameters has stabilising effect on the Type–I (cross–flow) instability mode. However, this is not the case for all rough disks, i.e. an increase in the roughness ratio does not always lead to stabilization of the flow.

Moreover, following Imayama et al. (2012), the growth of the disturbances in the boundary layer was measured by means of plotting the root mean square (rms) values of the azimuthal velocity fluctuations against the Reynolds number. Sudden rises in these corresponding figures indicate the instability regions and the growth rates in these regions can be calculated from these figures. The location of the instability region in the current study for the smooth disk slightly differs

from the corresponding location provided by Imayama et al. (2012). However, the growth rate calculated in the current study is virtually equal to the one given in Imayama et al. (2012). The graphs of the growth rates were, correspondingly, obtained for all rough disks and it was revealed from these graphs that the surface roughness has no effect on either the location of the instability region or the growth rate, in the current particular experimental facility. Nevertheless, this observation cannot be validated since the corresponding experimental data is not available in literature and also Imayama et al. (2012) carried out the experiments only for a smooth disk in their air–based facility.

In addition, the probability density function (PDF) was used as a means of a graphical representation of the flow characteristics, particularly the transition process, in the current study. These PDF graphs illustrate highly skewed flow structures occurring in the transition region similar to those observed in the corresponding figure of Imayama et al. (2012). The structure of the flow that is normal to the wall was also visualized by means of the PDF technique. The formations and the changes of the flow structure with a gradually increased Reynolds number that was observed in the current study are similar to those seen in the corresponding figures of Imayama et al. (2012). Additionally, the PDF technique was employed to visualize the flow over the rough disks, however, the comparison between the PDF graphs obtained for the smooth disk and the rough disks display no significant differences. Therefore, any advantages of the use of the PDF visualization technique to investigate the effects of the roughness on the transition process cannot be found in this particular water–based experimental facility.

In conclusion, regarding the main motivation and goal of the current experimental study, some sort of surface roughness, which is characterized by the depth and the width of the concentric grooves, can stabilize the Type–I (cross–flow) instability mode of the rotating–disk boundary–layer flow. However, it is hard to draw a general conclusion with the current experimental data due to

the difficulties arising generally from the finite size of the water–based rotating–disk experimental facility. Due to these difficulties, we have started designing and building a new air–based rotating–disk experimental facility during the later stages of the current project and that this facility will be completed, commissioned and tested as part of a future PhD study.

7.1 Future Work

As a result of the high level of consistency between the roughness–induced effects predicted by means of the current TSST simulations and the corresponding theoretical results of Cooper et al. (2015), it may be possible to employ the TSST approach to determine theory–based calibration charts relating to the slip coefficients of the *partial slip* approach. This consideration can only be possible by means of further TSST simulations in connection with the computations based on the *partial slip* approach and thus the slip coefficients which do not bear any direct relevance to real surface roughness. Ultimately, after these further simulations, a calibration chart showing the equivalent real geometric roughness heights of the corresponding slip coefficients may be obtained.

Moreover, the TSST simulations show that the Type–II instability mode vanishes for a single temporal frequency for the rotor–stator flow configuration currently studied. The disappearance of this mode was also observed by Alveroglu et al. (2016) when the flow configuration is changed from the von Kármán flow to Ekman flow. Due to the fact that the rotor–stator flow configuration was determined as the intermediate state between these two flow types, the existence of the rotation of the fluid above the boundary layer of the rotating disk might be the reason of the disappearance of Type–II mode in our numerical simulations for a single temporal frequency. This may, furthermore, explain why the Type–II mode has not yet been clearly observed in experiments. The in-depth further investigation of the TSST results may reveal the reason of this disappearance of

the Type–II mode.

Furthermore, although, the current experimental study provides valuable results which may be the first experimental confirmation of the stabilizing effect of this type of surface roughness (concentric grooves) on the Type–I mode, a more general conclusion cannot be drawn with the existing data due to the distortion results from the restricted geometry of the water–based facility. As a result of the current promising results, it is worth investigating the effects of these surface profiles (concentric grooves) on the boundary–layer transition by means of an air–based rotating–disk facility where the flow is not restricted and thus the experimental data would not be biased.

Bibliography

Al-Garni, A. M. Low speed calibration of hot-wire anemometers. *Flow Measurement and Instrumentation*, 18(2):95–98, 2007.

Aldaş, K. and Yapıcı, R. Investigation of effects of scale and surface roughness on efficiency of water jet pumps using cfd. *Engineering Applications of Computational Fluid Mechanics*, 8(1):14–25, 2014.

Alfredsson, P. H., Örlü, R., and Schlatter, P. The viscous sublayer revisited - exploiting the self-similarity to determine the wall position and friction velocity. *Experiments in Fluids*, 51(1):271–280, 2011.

Alter, S. A structured-grid quality measure for simulated hypersonic flows. *AIAA Journal*, 42nd AIAA Aerospace Sciences Meeting and Exhibit, 2004.

Alveroglu, B., Segalini, A., and Garrett, S. The effect of surface roughness on the convective instability of the BEK family of boundary-layer flows. *European Journal of Mechanics - B/Fluids*, 56:178 – 187, 2016.

Andrews, G. E., Bradley, D., and Hundy, G. F. Hot-wire anemometer calibration for measurements of small gas velocities. *International Journal of Heat and Mass Transfer*, 15(10):1765–1786, 1972.

ANSYS Fluent Theory Guide, Release 15.0. 275 Technology Drive, Canonsburg, PA 15317, USA, 2013.

ANSYS Fluent User's Guide, Release 15.0. 275 Technology Drive, Canonsburg, PA 15317, USA, 2013.

Aupoix, B. Wall Roughness Modelling with k-w STT Model. In *10th International ERCOFTAC Symposium on Engineering Turbulence Modelling and Measurements*, Marbella, Spain, 2014.

Aydin, M. and Leutheusser, H. J. Very low velocity calibration and application of hot-wire probes. *DISA Info*, 25:17–18, 1980.

Barth, T. J. A 3-D upwind euler solver for unstructured meshes. *AIAA Paper*, 91–1548, 1991.

Blazek, J. *Computational Fluid Dynamics: Principles and Applications, 3rd ed.* Elsevier, 2015.

Bödewadt, U. T. Die drehströmung über festem grunde. *ZAMM - Journal of Applied Mathematics and Mechanics / Zeitschrift für Angewandte Mathematik und Mechanik*, 20(5):241–253, 1940.

Bradshaw, P., Ferriss, D. H., and Atwell, N. P. Calculation of boundary-layer development using the turbulent energy equation. *Journal of Fluid Mechanics*, 28:593–616, 1967.

Bruun, H. H. *Hot-Wire Anemometry, Principles and Signal Analysis.* Oxford University Press, Oxford, UK, 1995.

Bruun, H. H. Hot-wire anemometry in liquid flows. *Measurement Science and Technology*, 7:1301–1312, 1996.

Bruun, H. H., Khan, M. A., Alkayiem, H. H., and Fardad, A. A. Velocity calibration relationships for hot-wire anemometry. *Journal of Physics E: Scientific Instruments*, 21(2):225–232, 1988.

Bruun, H. H., Farrar, B., and Watson, I. A swinging arm calibration method for low velocity hot-wire probe calibration. *Experiments in Fluids*, 7(6):400–404, 1989.

Carpenter, P. W. The right sort of roughness. *Nature*, 388:713–714, 1997.

Chen, Z. J. and Przekwas, A. J. A coupled pressure-based computational method for incompressible/compressible flows. *Journal of Computational Physics*, 229 (24):9150–65, 2010.

Christman, P. J. and Podzimek, J. Hot-wire anemometer behavior in low velocity air-flow. *Journal of Physics E: Scientific Instruments*, 14(1):46–51, 1981.

Cochran, W. G. The flow due to a rotating disc. *Mathematical Proceedings of the Cambridge Philosophical Society*, 30:365–375, 1934.

Colley, A. J. *An experimental investigation of the flow in the boundary layer above a rotating disc, with compliant characteristics, in water*. PhD thesis, University of Warwick, Coventry, UK, 1997.

Colley, A. J., Thomas, P. J., Carpenter, P. W., and Cooper, A. J. An experimental study of boundary-layer transition over a rotating, compliant disk. *Physics of Fluids*, 11(11):3340–3352, 1999.

Colley, A. J., Carpenter, P. W., Thomas, P. J., Ali, R., and Zoueshtiagh, F. Experimental verification of Type-II-eigenmode destabilization in the boundary layer over a compliant rotating disk. *Physics of Fluids*, 18(054107), 2006.

Cooper, A. J., Harris, J. H., Garrett, S. J., Özkan, M., and Thomas, P. J. The effect of anisotropic and isotropic roughness on the convective stability of the rotating disk boundary layer. *Physics of Fluids*, 27(014107), 2015.

Corke, T. C. and Knasiak, K. F. Stationary travelling cross-flow mode interactions on a rotating disk. *Journal of Fluid Mechanics*, 355:285–315, 1998.

Corke, T. C., Matlis, E. H., and Othman, H. Transition to turbulence in rotating-disk boundary layers—convective and absolute instabilities. *Journal of Engineering Mathematics*, 57(3):253–272, 2007.

Daily, J. W. and Nece, R. E. Chamber dimension effects on induced flow and frictional resistance of enclosed rotating disks. *ASME Journal of Basic Engineering*, 82(1):217–232, 1960.

Dassler, P., Kožulović, D., and Fiala, A. Modelling of roughness–induced transition using local variables. *V European Conference on Computational Fluid Mechanics, ECCOMAS CFD*, 2010.

Davies, C. and Carpenter, P. W. Global behaviour corresponding to the absolute instability of the rotating–disc boundary layer. *Journal of Fluid Mechanics*, 486:287–329, 2003.

Davies, C., Thomas, C., and Carpenter, P. W. Global stability of the rotating-disk boundary layer. *Journal of Engineering Mathematics*, 57(3):219–236, 2007.

Dryden, H. L. The review of published data on the effect of roughness on transition from laminar to turbulent flow. *Journal of the Aeronautical Sciences*, 20 (7):477–482, 1953.

Ekman, V. W. On the influence of the earth's rotation on ocean currents. *Ark. Mat. Astron. Fys.*, 2:1–53, 1905.

Faller, A. J. Instability and transition of disturbed flow over a rotating disk. *Journal of Fluid Mechanics*, 230:245–269, 1991.

Fedorov, A. V. Excitation of waves of instability of the secondary flow in the boundary layer on a swept wing. *Journal of Applied Mechanics and Technical Physics*, 29(5):643–648, 1988.

Ferrer, E. and Munduate, X. CFD predictions of transition and distributed roughness over a wind turbine airfoil. In *47th AIAA Aerospace Sciences Meeting including The New Horizons Forum and Aerospace Exposition*, Orlando, Florida, 2009.

Garrett, S. J., Cooper, A. J., Harris, J. H., Özkan, M., Segalini, A., and Thomas, P. J. On the stability of von Kármán rotating-disk boundary layers with radial anisotropic surface roughness. *Physics of Fluids*, 28(014106), 2016.

Gregory, N., Stuart, J. T., and Walker, W. S. On the stability of three-dimensional boundary layers with application to the flow due to a rotating disk. *Phil. Trans. R. Soc. Lond. A*, 248(943):155–199, 1955.

Hall, P. An asymptotic investigation of the stationary modes of instability of the boundary layer on a rotating disc. *Proceedings of the Royal Society of London A: Mathematical, Physical and Engineering Sciences*, 406(1830):93–106, 1986.

Harris, J. H. *Stability of the flow over a rough, rotating disk*. PhD thesis, University of Warwick, Coventry, UK, 2013.

Healey, J. J. Instabilities of flows due to rotating disks: preface. *Journal of Engineering Mathematics*, 57(3):199–204, 2007.

Hellsten, A. and Laine, S. Extension of the $k-\omega$–SST turbulence model for flows over rough surfaces. *AIAA Paper*, 97–3577, 1997.

Imayama, S., Alfredsson, P. H., and Lingwood, R. J. A new way to describe the transition characteristics of a rotating-disk boundary-layer flow. *Physics of Fluids*, 24(031701), 2012.

Jarre, S., Gal, P. L., and Chauve, M. P. Experimental analysis of the instability of the boundary layer over a rotating disk. *Europhysics Letters*, 14(7):649–654, 1991.

Jarre, S., Le Gal, P., and Chauve, M. P. Experimental study of rotating disk instability. i. natural flow. *Physics of Fluids*, 8(2):496–508, 1996a.

Jarre, S., Le Gal, P., and Chauve, M. P. Experimental study of rotating disk flow instability. ii. forced flow. *Physics of Fluids*, 8(11):2985–2994, 1996b.

Jasmine, H. A. and Gaijar, J. S. B. Absolute instability of the von Kármán, Bödewadt and Ekman flows between a rotating disc and a stationary lid. *Philosophical Transactions of the Royal Society A–Mathematical, Physical and Engineering Sciences*, 363(1830):1131–1144, 2005.

Kármán, T. V. Über laminare und turbulente Reibung. *ZAMM - Journal of Applied Mathematics and Mechanics*, 1(4):233–252, 1921.

Kobayashi, R., Kohama, Y., and Takamadate, C. Spiral vortices in boundary layer transition regime on a rotating disk. *Acta Mechanica*, 35(1-2):71–82, 1980.

Kohama, Y. Study on boundary layer transition of a rotating disk. *Acta Mech.*, 50:193–199, 1984.

Kohan, S. and Schwarz, W. H. Low-speed calibration formula for vortex shedding from cylinders. *Physics of Fluids*, 16(9):1528–1529, 1973.

Langtry, R. and Menter, F. Transition modeling for general CFD applications in aeronautics. *AIAA Journal*, 43rd AIAA Aerospace Sciences Meeting and Exhibit, 2005.

Langtry, R. B. and Menter, F. R. Correlation-Based Transition Modeling for Unstructured Parallelized Computational Fluid Dynamics Codes. *AIAA Journal*, 47(12):2894–2906, 2009.

Launder, B., Poncet, S., and Serre, E. Laminar, transitional, and turbulent flows in rotor-stator cavities. *Annual Review of Fluid Mechanics*, 42(1):229–248, 2010.

Launder, B. E. and Spalding, D. B. The numerical computation of turbulent flows. *Computers Method in Applied Mechanics and Engineering*, 3(2):269–289, 1974.

Lee, T. and Budwig, R. 2 improved methods for low-speed hot-wire calibration. *Measurement Science and Technology*, 2(7):643–646, 1991.

Lilly, D. K. On the instability of ekman boundary flow. *Journal of the Atmospheric Sciences*, 23(5):481–494, 1966.

Lingwood, R. J. Absolute instability of the boundary layer on a rotating disk. *Journal of Fluid Mechanics*, 299:17, 1995.

Lingwood, R. J. An experimental study of absolute instability of the rotating-disk boundary-layer flow. *Journal of Fluid Mechanics*, 314:373–405, 1996.

Lingwood, R. J. Absolute instability of the ekman layer and related rotating flows. *Journal of Fluid Mechanics*, 331:405–428, 1997.

Lingwood, R. J. and Alfredsson, P. H. Instabilities of the von Kármán Boundary Layer. *Applied Mechanics Reviews*, 67(030803), 2015.

Mack, L. The wave pattern produced by a point source on a rotating disk. *AIAA Journal*, 23rd Aerospace Sciences Meeting, 1985.

Malik, M. R. The neutral curve for stationary disturbances in rotating-disk flow. *Journal of Fluid Mechanics*, 164:275–287, 1986.

Malik, M. R., Wilkinson, S. P., and Orszag, S. A. Instability and transition in rotating disk flow. *AIAA Journal*, 19:1131–1138, 1981.

McDonald, P. W. The computation of transonic flow through two-dimensional gas turbine cascades. *ASME Paper*, 71–GT–89, 1971.

Menter, F. R. Two-equation eddy-viscosity turbulence models for engineering applications. *AIAA Journal*, 32(8):1598–1605, 1994.

Menter, F. R., Langtry, R. B., Likki, S. R., Suzen, Y. B., Huang, P. G., and Volker, S. A correlation-based transition model using local variables - Part I: Model formulation. *Journal of Turbomachinery*, 128(3):413–422, 2006.

Merkle, C. L., Kubota, T., and Ko, D. R. S. An analytical study of the effects of surface roughness on boundary–layer transition. *Flow Research Corp., Report 40*, 1974.

Miklavčič, M. and Wang, C. Y. The flow due to a rough rotating disk. *ZAMP - Journal of Applied Mathematics and Physics*, 55(2):235–246, 2004.

Owen, J. M. and Rogers, R. H. *Flow and Heat Transfer in Rotating Disc Systems - Vol.1 : Rotor-Stator Systems*. Research Studies Press, Taunton, U. K., 1989.

Özahi, E., Çarpinlioglu, M. O., and Gündoğdu, M. Y. Simple methods for low speed calibration of hot-wire anemometers. *Flow Measurement and Instrumentation*, 21(2):166–170, 2010.

Özkan, M., Thomas, P. J., Cooper, A. J., and Garrett, S. J. Comparison of the effects of surface roughness and confinement on rotor–stator cavity flow. *Engineering Applications of Computational Fluid Mechanics*, in press. doi: 10.1080/19942060.2016.1247297.

Press, W. H., Teukolsky, S. A., Vetterling, W. T., and Flannery, B. P. *Numerical Recipes in C, 2nd ed.* Cambridge University Press, 1992.

Rasmussen, C. G. The air bubble problem in water flow hot-film anemometry. *DISA Info*, (5):21–6, 1967.

Rayleigh, L. On the stability, or instability, of certain fluid motions. *Proceedings London Mathematical Society*, s1-11(1):57–72, 1879.

Reed, H. L. and Saric, W. S. Stability of three-dimensional boundary layers. *Annual Review of Fluid Mechanics*, 21(1):235–284, 1989.

Reynolds, O. On the dynamical theory of incompressible viscous fluids and the determination of the criterion. *Philosophical Transactions of the Royal Society of London A: Mathematical, Physical and Engineering Sciences*, 186:123–164, 1895.

Rogers, M. H. and Lance, G. N. The rotationally symmetric flow of a viscous fluid in the presence of an infinite rotating disk. *Journal of Fluid Mechanics*, 7:617–631, 1960.

Roshko, A. On the development of turbulent wakes from vortex shedding from cylinders. *NACA Report-1191, (formerly TN-2913)*, pages 801–825, 1954.

Saffman, P. G. A model for inhomogeneous turbulent flow. *Proceedings of the Royal Society of London A: Mathematical, Physical and Engineering Sciences*, 317(1530):417–433, 1970.

Sambo, A. S. *A theoretical and experimental study of the flow between a rotating and a stationary disc.* PhD thesis, University of Sussex, Brighton, UK, 1983.

Saric, W. S., Reed, H. L., and White, E. B. Stability and transition of three-dimensional boundary layers. *Annual Review of Fluid Mechanics*, 35(1):413–440, 2003.

Saric, W. S., Carpenter, A. L., and Reed, H. L. Passive control of transition in three-dimensional boundary layers, with emphasis on discrete roughness elements. *Philosophical Transactions of the Royal Society of London A: Mathematical, Physical and Engineering Sciences*, 369(1940):1352–1364, 2011.

Schlichting, H. and Gersten, K. *Boundary Layer Theory, 8th ed.* Springer, 2004.

Schubauer, G. B. and Klebanoff, P. S. Contribution on the mechanics of boundary layer transition. *NACA TN 3489*, 1955.

Skoog, D. A., Holler, F. J., and R., C. S. *Principles of Instrumental Analysis, 6th ed.* Thomson Brooks/Cole, 2007.

Smith, N. H. Exploratory investigation of laminar-boundary-layer oscillations on a rotating disk. *NACA Tech. Note No. 1227*, 1946.

Theodorsen, T. and Regier, A. Experiments on drag of revolving disks, cylinders and streamline rods at high speeds. *NACA-Report-793*, pages 367–384, 1944.

Tsanis, I. K. Calibration of hot-wire anemometers at very low velocities. *Dantec Inf*, 4:13–14, 1987.

Vaughan, C. *A numerical investigation into the effect of an external flow field on the sealing of a rotor-stator cavity*. PhD thesis, University of Sussex, Brighton, UK, 1986.

Wilcox, D. C. *Turbulence Modeling for CFD*. DCW Industries, Inc., La Canada, California, 1998.

Wilkinson, S. P. and Malik, M. R. Stability experiments in the flow over a rotating disk. *AIAA Journal*, 23(4):588–595, 1985.

Wu, S. and Bose, N. Calibration of a wedge-shaped vee hot-film probe in a towing tank. *Measurement Science and Technology*, 4(1):101–108, 1993.

Yoon, M. S., Hyun, J. M., and Park, J. S. Flow and heat transfer over a rotating disk with surface roughness. *International Journal of Heat and Fluid Flow*, 28 (2):262–267, 2007.

Yue, Z. and Malmstrom, T. G. A simple method for low-speed hot-wire anemometer calibration. *Measurement Science and Technology*, 9(9):1506–1510, 1998.

Zandbergen, P. J. and Dijkstra, D. Von-Kármán swirling flows. *Annual Review of Fluid Mechanics*, 19(1):465–491, 1987.

Zoueshtiagh, F., Ali, R., Colley, A. J., Thomas, P. J., and Carpenter, P. W. Laminar-turbulent boundary-layer transition over a rough rotating disk. *Physics of Fluids*, 15(8):2441–2444, 2003.

Appendix

The empirical correlations, in Equation 3.10, that controls the transition onset are described in the functions below.

$$Re_V = \frac{\rho^* y^2 S}{\mu^*}, \tag{A.1}$$

where y is the wall distance.

$$F_{onset1} = \frac{Re_V}{2.193 Re_{\theta_c}}, \tag{A.2}$$

$$F_{onset2} = min\left(max\left(F_{onset1}, F_{onset1}^4\right), 2.0\right), \tag{A.3}$$

$$R_T = \frac{\rho k}{\mu \omega}, \tag{A.4}$$

where k is the turbulent kinetic energy and ω is the specific dissipation rate.

$$F_{onset3} = max\left(1 - \left(\frac{R_T}{2.5}\right)^3, 0\right), \tag{A.5}$$

$$F_{onset} = max\left(F_{onset2} - F_{onset3}, 0\right), \tag{A.6}$$

The empirical correlations, F_{length} and Re_{θ_c}, in Equations 3.10 and A.2 are defined as below.

$$F_{length} = \begin{cases} \left[398.189.10^{-1} + \left(-119.270.10^{-4}\right)\tilde{Re}_{\theta_t} \right. & \\ \left. + \left(-132.567.10^{-6}\right)\tilde{Re}_{\theta_t}^{2}\right], & \tilde{Re}_{\theta_t} < 400 \\ \left[263.404 + \left(-123.939.10^{-2}\right)\tilde{Re}_{\theta_t}\right. & \\ \left. + \left(194.548.10^{-5}\right)\tilde{Re}_{\theta_t}^{2}\right. & 400 \leq \tilde{Re}_{\theta_t} \leq 596 \\ \left. + \left(-101.695.10^{-8}\right)\tilde{Re}_{\theta_t}^{3}\right], & \\ \left[0.5 - \left(\tilde{Re}_{\theta_t} - 596.0\right) \cdot 3.0 \cdot 10^{-4}\right], & 596 \leq \tilde{Re}_{\theta_t} < 1200 \\ [0.3188], & 1200 \leq \tilde{Re}_{\theta_t} \end{cases} \tag{A.7}$$

$$Re_{\theta_c} = \begin{cases} \left[\tilde{Re}_{\theta_t} - \left(396.035.10^{-2} + \left(-120.656.10^{-4}\right)\tilde{Re}_{\theta_t}\right.\right. & \\ \left. + \left(868.230.10^{-6}\right)\tilde{Re}_{\theta_t}^{2} + \left(-696.506.10^{-9}\right)\tilde{Re}_{\theta_t}^{3}\right. & \tilde{Re}_{\theta_t} \leq 1870 \\ \left. \left. + \left(174.105.10^{-12}\right)\tilde{Re}_{\theta_t}^{4}\right)\right], & \\ \left[\tilde{Re}_{\theta_t} - \left(593.11 + \left(\tilde{Re}_{\theta_t} - 1870.0\right) \cdot 0.482\right)\right], & \tilde{Re}_{\theta_t} > 1870 \end{cases} \tag{A.8}$$

The empirical correlation, Re_{θ_t}, in Equation 3.16 is defined as below.

$$Re_{\theta_t} = \begin{cases} \left[1173.51 - 589.428Tu + \frac{0.2196}{Tu^2}\right] F\left(\lambda_\theta\right), & Tu \leq 1.3 \\ 331.5\left[Tu - 0.5658\right]^{-0.671} F\left(\lambda_\theta\right), & Tu > 1.3 \end{cases}, \tag{A.9}$$

where the pressure gradient function $F\left(\lambda_\theta\right)$ is described as

$$F\left(\lambda_\theta\right) = \begin{cases} 1 - \left[-12.986\lambda_\theta - 123.66\lambda_\theta^2 - 405.689\lambda_\theta^3\right] e^{-\left[\frac{Tu}{1.5}\right]^{1.5}}, & \lambda_\theta \leq 0 \\ 1 + 0.275\left[1 - e^{-[35.0\lambda_\theta]}\right] e^{\left[\frac{-Tu}{0.5}\right]}, & \lambda_\theta > 0 \end{cases}. \tag{A.10}$$

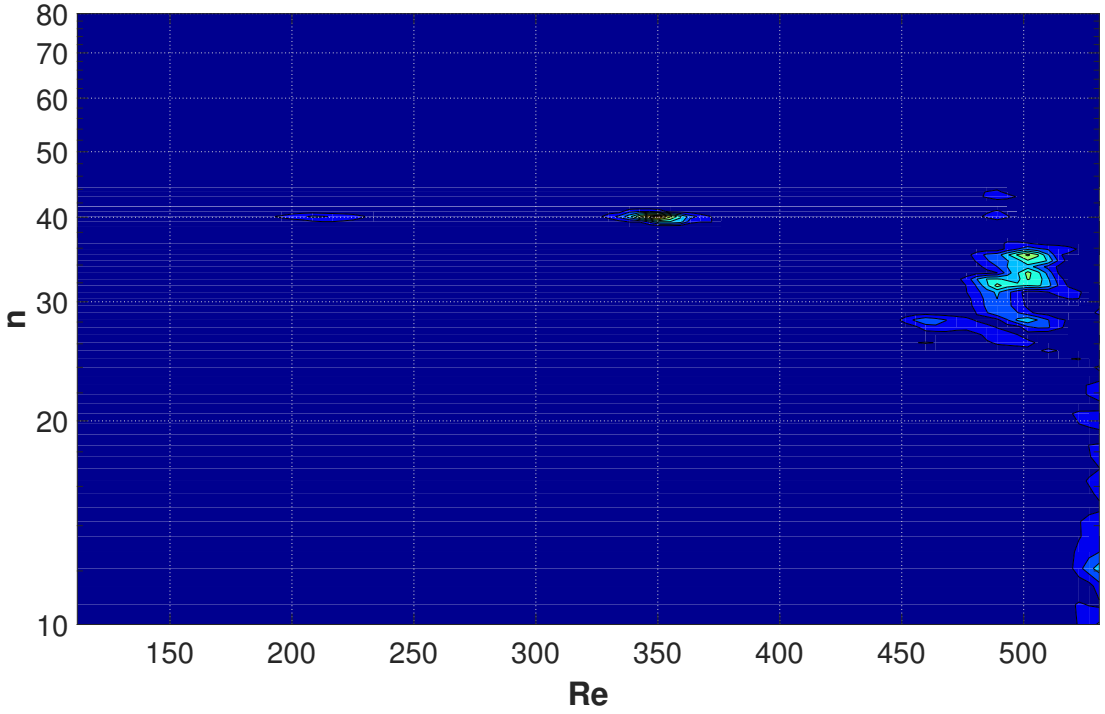

Figure 7.1: The contour plot of the Fourier energy spectrum on a logarithmic scale. The data were collected over the smooth disk at $\zeta = 1.3$ and $\Omega^* = 7.85$ rad/s.

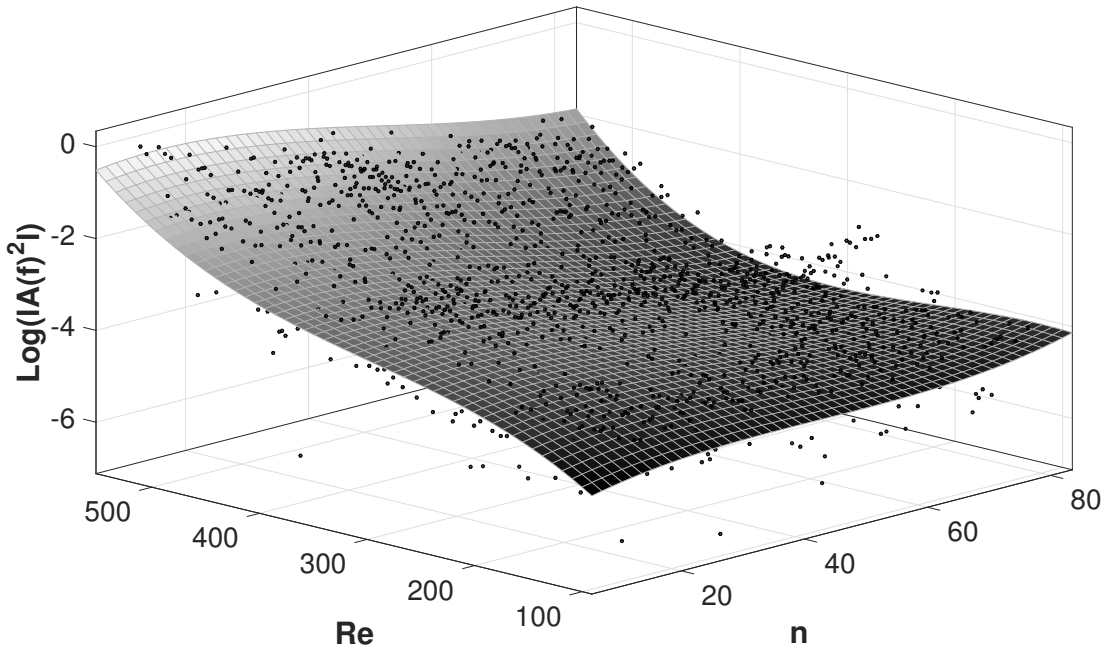

Figure 7.2: The surface function of the amplitude variation with respect to the azimuthal mode number, n, and the Reynolds number, Re. The data were collected over the smooth disk at $\zeta = 1.3$ and $\Omega^* = 7.85$ rad/s. The fitted polynomial surface is of degree 3 in both x and y. The coefficient of determination: $R^2 = 0.5828$.